The Dissertation Committee for Hirotatsu Armstrong Certifies that this is the approved version of the following dissertation:

A Generalized Method for Rapid Analysis of Active Interrogation Systems for Detection of Special Nuclear Material

Committee:

Erich A. Schneider, Supervisor

Steven R. Biegalski

Mark R. Deinert

Michael R. James

David P. Morton

A Generalized Method for Rapid Analysis of Active Interrogation Systems for Detection of Special Nuclear Material

by

Hirotatsu Armstrong, B.S.; M.S.

Dissertation

Presented to the Faculty of the Graduate School of

The University of Texas at Austin

in Partial Fulfillment

of the Requirements

for the Degree of

Doctor of Philosophy

The University of Texas at Austin

August 2013

To my parents,

Larry and Yoshiko Armstrong

Acknowledgements

I would first like to thank my advisor Erich Schneider for the guidance he has given me throughout my research, and for helping me through the problems that I thought were insurmountable. My committee deserves special recognition for investing their time in me and for being very understanding and accommodating, especially during the final weeks before my defense.

I would like to thank Michael James, Gregg McKinney, Russell Johns, and Michael Fensin of Los Alamos National Laboratory for taking the time to mentor me while I was there. And to Mark Deinert for being a reliable source of knowledge, as well as for the personal and profession advice he has given me.

I would like to thank all of my friends, and in particular Robert Flanagan, William Gurecky, and Kate Gurfein for getting me through this. Robert for helping me talk through and solve the problems that just seemed to never go away, Will for helping with the awesome illustrations used in my dissertation, and Kate for being a source of encouragement and support when things got rough.

Finally, I would like to thank my family for their love and support and for always believing that I can achieve whatever I set my mind to.

A Generalized Method for Rapid Analysis of Active Interrogation Systems for Detection of Special Nuclear Material

Hirotatsu Armstrong, Ph.D.

The University of Texas at Austin, 2013

Supervisor: Erich A. Schneider

Detection of special nuclear material (SNM) being smuggled into the US through ports of entry has been identified as a crucial capability for ensuring the safety and security of the US from radiological threats. Programs such as the NNSA's Second Line of Defense aim to deploy detection systems, both domestically and abroad, in an attempt to interdict the SNM before it reaches its destination. Active interrogation (AI) is a technique that relies on the detection of emitted particles which are produced when SNM is bombarded with a source of high energy photons or neutrons. This work presents a general framework that allows for fast radiation transport modeling of AI scenarios by generating families of response functions which depict neutron, gamma, or electron radiation exiting various regions within the problem, per unit source of radiation entering the region. The solution for a given scenario, typically the detector count rate, is computed by injecting a source term into the first region and applying the appropriate response functions, in sequence, for each subsequent region. For the AI systems modeled in this work, the source is an electron beam in a linear accelerator. Subsequent response functions create and transport bremsstrahlung photons into the SNM, and transport neutrons born in the problem to a detector. The computed solution is comparable to that

of a full Monte Carlo simulation, but is assembled in orders of magnitude less time from pre-computed response function libraries. The ability to rapidly compute detector spectra for complicated AI scenarios opens up research and analysis possibilities not previously possible, including conducting parametric studies of scenarios spanning a large portion of the threat space and generating detector spectra used for conditioning and testing of alarm algorithms.

Table of Contents

List of Tables

List of Figures

Chapter 1

INTRODUCTION

1.1 NUCLEAR MATERIALS AND NONPROLIFERATION

In 2009 at a speech given in Prague, president Obama stated that the security of the world's supply of nuclear materials was "the most immediate and extreme threat to global security," [1]. His speech outlined the development of a global Nuclear Security Summit with the goal of developing better safeguard methods and policies for securing the world's supply of nuclear materials [2]. Most non-proliferation efforts are concentrated at nuclear facilities where material controls and accounting (MC&A) [3] as well as physical protection systems (PPS) are the primary mechanisms of protection and accountability. Developing and implementing new and effective methods to properly account for and secure nuclear materials will ensure they remain out of the control of terrorist organizations and governments that may use the material for development of nuclear weapons or radiological dispersion devices.

Measures other than the standard MC&A and PPS are needed to ensure the safety of the US and its allies from nuclear threats. The possibility always exists that a country is developing a nuclear weapons program or producing weapons material covertly. Terrorist organizations may also be able to obtain nuclear materials either through direct dealings with rogue states or through obtaining the material by defeating the PPS and MC&A procedures at nuclear facilities. For these cases, systems must be in place to detect and interdict the materials as they are being transported before they reach their destination and are used for harm. The National Nuclear Security Administration (NNSA) has developed the Second Line of Defense (SLD) program to help "strengthen

the capability of foreign governments to deter, detect, and interdict illicit trafficking in nuclear and other radioactive materials across international borders and through the global maritime shipping system" [4]. The SLD program aims to equip foreign borders and ports with radiation detection equipment to both detect and identify nuclear materials that are being trafficked.

Special nuclear material (SNM) can be detected via passive or active methods which both rely on radiative properties of the nuclear material. Passive methods rely on detecting the radiation signature of nuclear material as it naturally decays; active methods involve interrogation of an object with an external source of radiation to stimulate the release of additional radiation from the SNM. This stimulated radiation is then detected to determine if SNM is present. These measures can serve as forms of primary and/or secondary screening before manual inspection of the cargo is required. The ability of these techniques to correctly discriminate radiological threats from benign material is crucial as both the direct costs associated with manually inspecting cargo and the indirect costs associated with disruption to the flow of commerce are high.

1.2 THREAT SIMULATION

Computationally simulating threat scenarios allows for optimization of detection strategies without the need for building a physical system and repeating experiments to fine-tune each system parameter. Simulation can help in the determination of the optimal interrogation energy, setup geometry, detector type, alarm algorithm as well as many other operational parameters. Simulations should be done on scenarios that span the entire threat space in order to fully characterize the capabilities of a particular system against all threats.

Most currently available radiation transport codes which can be used for simulation of threat scenarios require large computational resources to reach a properly converged solution when rich geometric detail is maintained. Because of this, direct computation of detector signals for scenarios spanning the entire threat space is infeasible. Hence, new detector systems or deployment strategies are typically designed and computationally benchmarked against only a few cases deemed to be representative of the most challenging scenarios. With this approach, systems can only be characterized for this small subset of the entire threat space. Ideally, one would like to have confidence that a system will detect a threat placed in any configuration before the costly step of building and physically testing a physical system is carried out.

The goal of this work is to develop a method which allows for rapid calculation of the time dependent detector signal for any given active interrogation (AI) scenario such that detection probabilities for scenarios spanning the entire threat space can be calculated within a time frame suitable for embedding in optimization calculations or informing alarm algorithms in real time. This is accomplished by doing the expensive radiation transport calculations once up-front and saving the data to a library. Calculations of the detection probabilities for a given scenario can then use this data rather than performing a full radiation transport simulation for the scenario.

To achieve the goal of rapid calculation of detection probabilities for any given scenario, a generic AI problem is broken up into multiple components called sub-models. These sub-models represent the major components of the AI scenario. The choice of how many sub-models to use and where the break points between the sub-models occur leads to a tradeoff of increased flexibility of the model against an increased difficulty in correctly matching boundary conditions at the sub-model interfaces. For each of the sub-models, response functions are computed which describe how radiation incident into the

sub-model is transformed as it traverses the sub-model. In general, the response functions map a particle with a given energy, direction, location, and time incident into the sub-model to a distribution of particles in energy, direction, location, and time exiting the sub-model. Since the data storage requirements are extremely large to completely capture all data over the entire phase space, approximations and interpolations over regions inside and at the boundaries of the phase space must be done to preserve the physics in lieu of storing all of the data. Choosing both the number and locations of the sub-models, as well as developing novel ways of matching boundary conditions without explicitly having all of the phase space data, is the major challenge of this research.

Once response functions for each sub-model have been generated, calculation of the detection probability is a matter of simply applying the response functions sequentially to a source term. Care must be taken to ensure the assumptions used within one sub-model are properly accounted for in the subsequent sub-model. If not, there will be a mismatch of boundary conditions between sub-models and applying the subsequent response function to the spectrum leaving a sub-model will result in systematic errors.

1.3 BENEFITS AND NOVELTY

The ability to rapidly calculate the detection probabilities for many scenarios, with various interrogation systems and configurations allows sensitivity, uncertainty, and optimization analyses that would otherwise require enormous computational resources to achieve. Simulations of many scenarios for a given interrogation and detector system would allow for better understanding of the range of threats over which the system will perform. These simulations can also be used to optimize operational parameters such as detector placement, or informatics like alarm algorithm specification. For example, the location of the detector system relative to the interrogation source can be varied to

determine the sensitivity of the measured signal to the detector location over a broad range of scenarios. The utility of these studies can extend to operational issues as well. Because different locations have unique background signature, operational parameters (detector placement, alarm algorithm) can be tuned to be most effective in the presence the measured local background.

Rapid simulation also allows for training and conditioning of various alarm algorithms. A large family of realistic test cases can be generated in which a subset is used for the conditioning, and the remainder used for assessing the efficacy of an algorithm. Test cases can also be run to determine what regions in the threat space AI reliably detects the presence of SNM with an acceptable false positive rate, and which regions it fails. This knowledge can help guide future research and development towards those areas which cannot be reliably addressed with current AI techniques. Additionally, rapid calculation of the detector signal can be used in real time where a measured signal can be compared against signals calculated in real time to estimate where within the threat space the measured signal is likely to originate from. This can be used as an additional method to flag cargo whose radiation signature matches that of cargo carrying non-benign material.

The general response function methodology has previously been developed and implemented for passive detection systems in the software XPASS [5][6]. This research aims to extend the methodology for application with AI systems. The major components of this research involve determining how many sub-models are needed, locating and defining their interfaces, developing and parameterizing each sub-model, and determining the appropriate boundary conditions at the interfaces. The boundary conditions generally represent a choice between flexibility and practicality: the more energy, position and direction information is retained at the boundaries, the higher

fidelity the reconstructions may be, but at the cost of burdensome precomputation and potentially prohibitive data storage needs. The theory for this work is presented in chapter 3, while the implementation of the theory for each sub-model as related to active interrogation is given in chapter 4. Chapter 4 also provides stand-alone simulations results and validation for each sub-model, while chapter 5 presents simulation results and case studies calculated with the full, integrated model. Finally, chapter 6 gives conclusions and recommendations for operational deployment as well as further model development.

Chapter 2

LITERATURE REVIEW

2.1 THREAT SPACE

The threat space for smuggling of nuclear materials can be defined as the set of all combinations of variables that lead to a possible threat scenario. These variables can include, but are not limited to: vehicle type, vehicle velocity, vehicle cargo, number of SNM sources, SNM isotopic composition, SNM size, SNM location within the cargo, shielding type, shielding thickness, detector type, detector position, AI source energy, local background spectrum, and alarm algorithm. It is easy to see how the combinatorics of even a coarse sampling of the threat space can lead to a very large number of distinct threat scenarios. This issue has been recognized, and a more compact, yet still representative, threat space can be populated following the guidelines of a report by Lawrence Livermore National Laboratory (LLNL) [7]. The report narrows the size of the threat space significantly by identifying several key regions of interest within the threat space. Reductions in the threat space include: a) only considering low z, mid z, and high z cargo, b) defining several isotopic compositions of interest, c) restrictions on SNM size based upon criticality considerations, and d) consideration of only several shielding materials of interest. Using this methodology, computational modeling can be limited to only regions of the threat space which are of interest.

2.2 PASSIVE DETECTION

Passive detection systems use radiation detectors to detect the presence of particles emanating from the natural decay process of the SNM. These systems typically employ PVT plastic scintillators as photon detectors [8], but NaI crystals or solid state

detectors can be used to increase the energy resolution if spectroscopic capability is desired [9][10][11]. The simplest passive systems employ plastic scintillator detectors for photon detection. These systems count the number of photon interactions in the detector and signal an alarm if the count rate exceeds a threshold that is dictated by the local background count rate [12]. This method of alarming on only the count rate relative to background is termed gross counts (GC) and is the simplest type of alarm algorithm.

Plastic scintillator detectors have very poor energy resolution, but even the crude energy information they offer can be used to determine if SNM is present. A passive algorithm of this type is termed an energy windowing (EW) [13] algorithm. The EW algorithm bins the crude spectral count rates into energy windows (large energy bins). After binning, the count rate in each of the energy windows can be compared to that of the background spectrum in the same window to determine if a threat is present. The energy window data can be compared to the background spectrum in multiple ways. Typically, a ratio of the counts (or count rate) in an energy window to some other quantity (counts in a reference window, total counts over all windows, etc.) is used. These ratios are then compared to the same ratios calculated for the background spectrum and an alarm is signaled if the ratios differ by a predetermined amount defined by the background spectrum and acceptable false positive rate.

Neutrons can also be detected with passive system by employing ^{3}He or BF_3 detectors. Neutron detection can be advantageous as the presence of neutrons above background is a strong indicator to the presence of SNM, as most nuisance sources do not emit neutrons. In the case of weapons-grade plutonium (WGPu), the spontaneous fission source strength of ^{240}Pu makes unshielded WGPu relatively easy to detect if neutron detection is available. However, background neutrons from cosmic and terrestrial

sources limit the minimum detectable activity from a neutron source and can be a source of false alarms.

Passive interrogation systems have difficulty discriminating SNM from benign sources due to the relatively weak signal of naturally decaying SNM and the effectiveness of shielding. Effects such as baseline suppression, where the vehicle passing through the detector shields the detector from background radiation, increase the minimum detectable activity of potential threats [14]. Nuisance sources present in the cargo, such as naturally occurring radioactive material (NORM) and medical radioisotopes, make discriminating between SNM and benign objects difficult with passive methods. GC algorithms have no ability to determine whether the source of the increased counts is due to a nuisance source or SNM. EW algorithms have only limited ability to discriminate nuisance sources from SNM due to the poor energy resolution of the widely-used PVT detectors.

Passive detection systems based off of PVT detectors are currently the most common systems in place due to the relatively low cost of PVT detectors compared to NaI or germanium detectors. Obtaining spectroscopic data by upgrading the detection system to NaI or germanium would allow for isotope identification by performing a peak analysis on the spectrum. Spectroscopy is essentially the limit of an EW algorithm when the energy resolution becomes fine enough to allow for peak identification. With spectroscopic analysis, the issues of background suppression and NORM within cargo can be mitigated [15][16].

2.3 ACTIVE DETECTION

2.3.1 Photon Radiography

The simplest form of active detection involves interrogating cargo with photons and generating a radiographic image of the cargo by measuring the attenuation of the beam as it passes through the cargo. SNM as well as commonly used shielding materials are typically relatively dense and have a high Z such that the photon beam is highly attenuated as it passes through the threat object. Radiographic systems can detect the presence of these high density/high Z objects, but there is little ability to discriminate SNM from many other common high density/high Z objects such as steel.

2.3.2 Active Interrogation

Due to the limitations of both radiographic and passive detection systems, AI systems are thought to be required for reliable detection of shielded SNM such as highly enriched uranium (HEU) [17]. Active interrogation is the process of stimulating the release of radiation from an object by hitting it with an external source of radiation. In SNM, these stimulated emissions occur both during and after irradiation by the source, so a radiation signature that persists after the source has turned off is an indicator of the presence of SNM. The most common application of an AI system in the homeland security context would be the use of a photon beam to stimulate the release of both photons and neutrons via photonuclear interactions with an object. Other forms of active interrogation using a neutron source [18] or muons [19] are also being investigated.

Photon interrogation systems typically use a linear accelerator to accelerate electrons onto a high Z target to generate a source of bremsstrahlung photons. These photons are collimated to form a beam which is then directed onto the object being screened. A detector system is put in place to detect any stimulated emissions from the

photon interrogation. The detector can either be co-located with the linear accelerator, or it can be located opposite or to the side of the interrogation object. The detector system can detect delayed photons, prompt neutrons, delayed neutrons, or a combination of the three; prompt photons are usually not detected as the photons from the interrogation source saturate the detector and would dominate the signal.

Detection of delayed particles is a strong indicator to the presence of SNM. The initial high intensity burst of photons from the interrogation causes the release of both photons and neutrons due to photonuclear interactions within the cargo. The continued release of photons and/or neutrons after the initial burst can be caused by the decay of activation products, fission product decays, and subcritical multiplication in the SNM. Fission products and subcritical multiplication are not present in benign material and the presence of these cause radiation to be emitted after the interrogation has ceased. Since neutrons transport at a finite speed, analysis of the detector signal must be done accounting for the time required for neutrons to reach the detector, taking into account scattering in the shielding and cargo during transport. Since photon transport happens nearly instantaneously, any counts in the detector after the interrogation has ceased can be treated as a delayed emission.

2.4 RADIATION TRANSPORT CODES

Monte Carlo codes such as MCNPX [20] and GEANT 4 [21] have been extensively benchmarked and shown to offer extremely high fidelity results as long as the proper nuclear data is available. If the geometry and physics options are correctly specified, then the radiation transport solutions obtained can be considered to be correct with high confidence, given the limitations in the user created model. Since it will never

be possible to fully replicate actual conditions of a real interrogation system, the driving force of error in modeling efforts is the fidelity and completeness of the user model.

Discrete ordinates (S_n) [22] codes such as GADRAS (1-D) [23], PARTSIN (3-D) [24], and DENOVO (3-D) [25] can be used in lieu of Monte Carlo methods. The advantage of S_n codes as compared to Monte Carlo codes is that S_n codes compute the solution (particle flux) at all locations within the problem simultaneously; for Monte Carlo codes, the solution is only calculated in regions explicitly specified by the user; each additional region comes at cost computationally. S_n codes typically run faster than Monte Carlo codes, but accurately modeling and meshing complex geometries is more difficult. For both Monte Carlo and 3D S_n codes, high computational costs are incurred if high fidelity in energy, direction, location, time, and geometric detail is desired. A major downside to S_n codes as compared to Monte Carlo codes is the discretization of energy and direction. This discretization can lead to artifacts, such as ray effects, in the solution which the user must be aware of to properly interpret the results.

2.5 THREAT REDUCTION TOOLS

Current threat reduction software allows the user to build a specific threat scenario and analyze the detector signal to determine whether SNM would be detectable in the given scenario. SWORD [26] is one such code which gives a graphical CAD-like interface to the user for setting up the problem geometry. SWORD takes this geometry and passes it to a Monte Carlo code, either GEANT 4 or MCNPX, to simulate the scenario. The detector spectra are output as ASCII text files which can then be passed to various alarm algorithms for analysis. TR-X [27] is a code developed at Los Alamos National Lab (LANL) which aims to have similar features as SWORD, but is designed specifically with MCNPX as the underlying simulation engine. TR-X uses pre-defined

templates which can be loaded and modified to build scenarios. TR-X then creates a set of input decks for the scenario and submits them as a batch to MCNPX for computation. The results are then aggregated and available for display through the TR-X GUI. Both SWORD and TR-X are essentially graphical wrappers around a Monte Carlo radiation transport code to allow for easier setup of the scenario parameters. Computation time with either SWORD or TR-X is the same as if the user were to run MCNPX or GEANT 4 independently for each scenario.

Chapter 3

THEORY

3.1 TRANSPORT EQUATION AND GREEN'S FUNCTIONS

In radiation transport, the particle flux is a scalar field specified by its location $\vec{\boldsymbol{r}}$, energy E, and direction $\boldsymbol{\Omega}$ at a given time t. Photon transport can be assumed to occur instantaneously, therefore time is not explicitly tracked unless there is a time dependent source. For neutrons and other massive particles, time must be explicitly tracked unless the system has reached a steady state. Let $\psi(\vec{\boldsymbol{r}}, E, \hat{\boldsymbol{\Omega}}, t)$ $[cm^{-2} \cdot s^{-1} \cdot MeV^{-1} \cdot str^{-1}]$ be the angular and energy dependent particle flux, so that $\psi(\vec{\boldsymbol{r}}, E, \hat{\boldsymbol{\Omega}}, t) dE d\Omega dt$ represents the flux $[cm^{-2}]$ of particles at $\vec{\boldsymbol{r}}$, having a kinetic energy between E and $E + dE$, traveling in a direction $d\Omega$ about $\hat{\boldsymbol{\Omega}}$, at a time between t and $t + dt$. Let λ represent the phase space of this flux such that $\psi(\lambda) = \psi(\vec{\boldsymbol{r}}, E, \hat{\boldsymbol{\Omega}}, t)$.

Green's functions are a mathematical tool used to describe the response of a system to an external source. They are used in electromagnetic theory to study the response of a system due to the presence of charge and in thermodynamics to study the response of a system due to an external heat source. In this work, Green's functions are used to determine the flux of particles in one region of a problem given an arbitrary distribution of particles in another region.

Let H be an operator describing the time-independent neutron transport equation in a non-multiplying medium such that

$$H = \hat{\boldsymbol{\Omega}} \cdot \vec{\nabla} + \Sigma_t(\vec{\boldsymbol{r}}, E) - \int dE' \int d\Omega' \, \Sigma_s(\vec{\boldsymbol{r}}, E \leftarrow E', \hat{\Omega}' \cdot \hat{\Omega}), \tag{3.1}$$

where $\Sigma_t(\vec{\boldsymbol{r}}, E)$ $[cm^{-1}]$ is the macroscopic total cross-section and $\Sigma_s\left(\vec{\boldsymbol{r}}, E \leftarrow E', \hat{\Omega}' \cdot \hat{\Omega}\right)$ $[cm^{-1} \cdot MeV^{-1} \cdot str^{-1}]$ is the double differential macroscopic scattering cross-section. For an external neutron source $q(\lambda')$ $[n \cdot cm^{-3} \cdot s^{-1} \cdot MeV^{-1} \cdot str^{-1}]$, the flux at any point in phase space can be obtained by solving

$$H\psi(\lambda) = q(\lambda)\,. \tag{3.2}$$

The solution to equation 3.2 can be expressed using a Green's function as

$$\psi(\lambda) = \int d\lambda' G(\lambda' : \lambda) q(\lambda'), \tag{3.3}$$

where $G(\lambda' : \lambda)$ is the Green's function for the system, and is defined by

$$HG(\lambda' : \lambda) = \delta(\lambda - \lambda'), \tag{3.4}$$

where $\delta(\lambda - \lambda')$ is the Dirac delta function.

For radiation transport, the Green's function is used to describe how a unit strength source with a given energy, location, and direction contributes to the flux at any location, over all energies, and traveling in any direction. Integrating this response over all source locations, energies, and directions yields the total flux at any point λ within the phase space. Solving equation 3.2 is difficult for a completely general problem as the source term can be non-trivial and not easily expressed in terms of simple functions. Solving the system with Green's functions involves solving a simpler transport equation (equation 3.3), over the phase space encompassed by the source.

3.2 PROBLEM DECOMPOSITION

The ability to analyze a variety of threat scenarios requires the computation of $G(\lambda' : \lambda)$ for each of the scenarios. Radiation transport codes such and MCNPX can be used to generate these Green's functions which can be stored for future use. The major

drawback with this approach is that the computational time and resources needed to obtain Green's functions that span a significant portion of the threat space is on the same order as the resources needed to directly simulate each scenario.

To overcome these computational issues, the general problem can be decomposed into several regions, each having its own Green's function. The Green's functions will describe how a source or particles entering one region of the problem contributes to the distribution of particles leaving that region. If the particles exiting one region are used as the source term for the next region, then the Green's functions can then be applied sequentially, matching conditions at the boundaries of each region, to obtain the same result had a single Green's function describing the whole problem been used. In principle, the distribution of particles in space, energy, angle, and time must be matched at the interfaces between every region. In practice, assumptions on some of these variables allow for approximate matching of the boundary conditions without explicitly needing to obtain a Green's function which is completely specified over all of phase space. This saves on both computation time required to generate the Green's functions as well as storage requirements for the data, making this method practical.

An example of this decomposition approach can be illustrated with a simple example of obtaining the flux in a detector from a source behind a semi-infinite slab of shielding. A spherically symmetric point source of strength $q\ [n \cdot cm^{-3} \cdot s^{-1} \cdot MeV^{-1} \cdot str^{-1}]$ is emitting neutrons in a vacuum with some arbitrary distribution in energy and angle. A semi-infinite slab of thickness t and total absorption and scattering cross-sections of Σ_a and Σ_s is located a distance a from the source. A detector is placed at a distance b on the other side of the shield. The system is assumed to be in steady state such that there is no time dependence of the detector signal. The average flux in the detector can be found by direct solution of the transport equation, or

by decomposing the problem and rebuilding the scenario from solutions given by Green's functions for each region. The second option, which is the underlying principle of this work, will be outlined below.

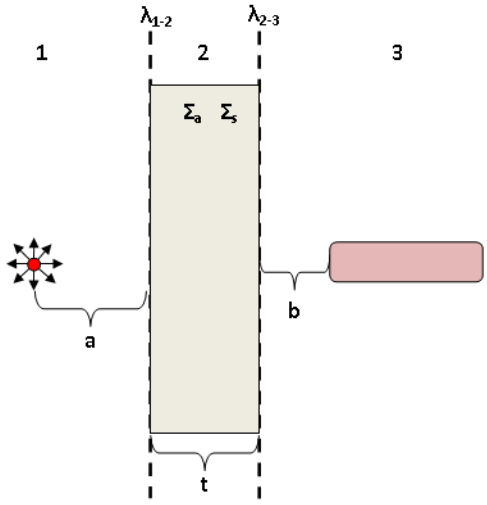

Figure 3.1: Geometry of the example problem.

The solution to this shielding problem can be obtained by breaking the problem into three distinct regions, each having its own Green's function (G_1, G_2, and G_3) which satisfy equations 3.3 and 3.4 for their respective regions. The phase space λ is subdivided into λ_1, λ_2, and λ_3 corresponding to the phase space encompassed by regions 1, 2, and 3 respectively. The parts of phase space corresponding to the interfaces of the regions are designated $\lambda_{1\text{-}2}$ and $\lambda_{2\text{-}3}$. $\lambda_{1\text{-}2}$ describes the points in phase space corresponding to particles of all energies, located on the plane at the interface of regions 1 and 2, that are headed into region 2 from region 1; $\lambda_{2\text{-}3}$ is defined similarly for the interface between regions 2 and 3.

Starting with the volumetric source q in region 1, the neutron flux at the interface of regions 1 and 2, $\psi(\lambda_{1-2})$, can be obtained by integrating $G_1(\lambda_{1\text{-}2},\lambda_1)\,q(\lambda_1)$ over all λ_1,

$$\psi(\lambda_{1-2}) = \int d\lambda_1 G_1(\lambda_1 : \lambda_{1-2}) q(\lambda_1)$$
$$\psi(\lambda_{1-2}) = \int d\vec{\boldsymbol{r}}' \int dE' \int d\Omega' G_1\left(\vec{\boldsymbol{r}}', E', \hat{\boldsymbol{\Omega}}' : \vec{\boldsymbol{r}}, E, \hat{\boldsymbol{\Omega}}\right) q\left(\vec{\boldsymbol{r}}', E', \hat{\boldsymbol{\Omega}}'\right) \quad 3.5$$

where $G_1(\lambda_1:\lambda_{1\text{-}2})$ has units of $\left[\frac{flux/(n \cdot cm^{-3} \cdot MeV^{-1} \cdot str^{-1})}{cm^{-3} \cdot MeV^{-1} \cdot str^{-1}}\right]$. $G_1(\lambda_1:\lambda_{1\text{-}2})$ describes the contribution to the energy dependent angular neutron flux at all locations $\vec{\boldsymbol{r}}$ on the plane between regions 1 and 2, from a unit strength source with energy between $E' + dE'$, within a volume dV', and headed in a direction $d\Omega'$ about $\hat{\boldsymbol{\Omega}}'$. This neutron flux can then be used as a planar source entering region 2. No assumptions need to be made on the spatial, energy, or angular distribution of neutrons at the interface of regions 1 and 2 as the information about these distributions are captured in $\psi(\lambda_{1-2})$. Integrating $G_2(\lambda_{1-2}:\lambda_{2-3})\psi(\lambda_{1-2})$over all $\lambda_{1\text{-}2}$ yields the neutron flux on the plane at the back surface of the shield,

$$\psi(\lambda_{2-3}) = \int d\lambda_{1-2} G_2(\lambda_{1-2} : \lambda_{2-3}) \psi(\lambda_{1-2}). \quad 3.6$$

Since $\psi(\lambda_{1-2})$has the same units as $\psi(\lambda_{2-3})$ $[flux]$, $G_2(\lambda_{1-2}:\lambda_{2-3})$ takes units of $[cm^{-3} \cdot MeV^{-1} \cdot str^{-1}]$ such that the integration over position, energy, and direction preserves units of $[flux]$. The Green's function G_2 has different units than G_1 as they describe the response arising from different source terms. In general, the units of the Green's function for any region will be based both on the source term and the quantity of interest (flux, current, detector count rate, etc) being calculated.

Using $\psi(\lambda_{2-3})$ as the source of neutrons in region 3, the flux at any location within region 3 is calculated from

$$\psi(\lambda_3) = \int d\lambda_{2-3} G_3(\lambda_{2-3} : \lambda_3) \psi(\lambda_{2-3}). \quad 3.7$$

$\psi(\lambda_3)$ can then be averaged over the volume of the detector to obtain the average flux in the detector.

If parameters of the problem such as material compositions are changed, new Green's functions describing the response of the perturbed system must be made. If the Green's function for each region can be obtained independently, then perturbations in one region can be handled by replacing the Green's function describing the response of the perturbed region without invalidating the Green's functions generated for any other region. But when a perturbation is made, the fluxes at all downstream interfaces between phase space regions will change, and therefore recomputed. Therefore, families of Green's functions that span all perturbations of interest to a region's geometry and composition must be created to permit the reconstruction of the particle flux exiting a region that has properties that are not constant across scenarios. In practice, this is facilitated by discretizing the phase space as will be discussed below. While these requirements imply significant precomputation is needed to use the Green's function approach, the ability to easily interchange Green's functions allows for fast analysis of many scenarios.

3.3 PHASE SPACE DISCRETIZATION

Discretization of the phase is necessary for computation and storage of the Green's function data. In general, discretization divides each component of phase space (location, energy, direction, and time) into discrete bins. Energy discretization is handled by binning particles in energy bins that are sufficiently fine to reproduce the correct physics of the problem. Spatial discretization is accomplished by computing Green's functions that describe the flux at fixed locations such as the region interfaces. Interpolation between these Green's functions gives an approximation for the Green's functions describing the flux at any location where data does not exist. Direction is handled by either a parameterization of the angular distribution to a μ^n approximation,

where μ is the cosine of the direction of travel, or storage of the data in angular bins. The latter approach is significantly more expensive computationally as well as in terms of data storage requirements and therefore is avoided unless no approximation method can produce reasonable results. Discretization in time, when necessary, is accomplished by calculating the flux integrated over discrete time bins. Integrating the flux over time rather than calculating the flux at specific points in time preserves the total number of particles crossing a surface over any specified time interval.

Equation 3.3 can be simplified to

$$\psi(\vec{\boldsymbol{r}}, E, \hat{\boldsymbol{\Omega}}) = \int dE' G(E' : \vec{\boldsymbol{r}}, E, \hat{\boldsymbol{\Omega}}) q(E'), \qquad 3.8$$

where $G(E' : \vec{\boldsymbol{r}}, E, \hat{\boldsymbol{\Omega}})$ $\left[\frac{flux \cdot MeV}{MeV}\right]$ is the Green's function, which has been integrated over all source locations and directions $\vec{\boldsymbol{r}}'$ and $\hat{\boldsymbol{\Omega}}'$, for contributions to the energy dependent flux at location $\vec{\boldsymbol{r}}$ for particles going in direction $\hat{\boldsymbol{\Omega}}$. $q(E')$ $\left[\frac{source\ particles/s}{MeV}\right]$ is the energy dependent source which has been integrated over source location and directions. Equation 3.8 is the form of equation 3.3 that remains to be discretized when MCNPX is used to generate Green's function data, as will be done in this work. This is because the MCNPX tally data obtained from an MCNPX simulation is from the sum of contribution integrated over source location and direction specified on the SDEF card. Source energy is not discretized as independent MCNPX runs will be done for each energy; after discretization in energy (described below), a MCNPX simulation will be done for each source energy group to obtain the contribution to flux from a source within each energy group. The Green's function $G(E' : \vec{\boldsymbol{r}}, E, \hat{\boldsymbol{\Omega}})$ and the source term $q(E')$ in equation 3.8 are specific to the location of the upstream source and downstream phase space interface, which are explicitly specified within an MCNPX input deck when the source term and tallies are defined.

The angular flux $\psi(\vec{r}, E, \hat{\Omega})$ in equation 3.8 is written as the product of a spatial and energy dependent flux $\phi(\vec{r}, E)$ with an energy dependent angular distribution $f(E, \hat{\Omega})$, $\psi(\vec{r}, E, \hat{\Omega}) \rightarrow \phi(\vec{r}, E) f(E, \hat{\Omega})$. The function $f(E, \hat{\Omega})$ can be parameterized into a uniform, cosine, or any other energy dependent angular distribution appropriate for the given region.

Discretization of equation 3.8 in energy turns the source distribution $q(E')$ into an N element column vector $\vec{\boldsymbol{q}} \in \mathbb{R}^{\boldsymbol{N}}$ describing the source energy distribution with embedded angular and spatial distributions over $\vec{r}'$ and $\hat{\Omega}'$ that have been specified in the source definition within MCNPX. The Green's function $G(E' : \vec{r}, E, \hat{\Omega})$ is transformed into a $M \times N$ matrix (response function) $\boldsymbol{R} \in \mathbb{R}^{\boldsymbol{M \times N}}$, where the matrix element ${}^{e,e'}\boldsymbol{R}$ describes the probability that a particle which enters the region in energy group e' leaves the region in energy group e.

Since the source term $\vec{\boldsymbol{q}}$ and the response function matrices $\boldsymbol{R}$ describe the continuous energy distribution integrated over multiple energy bins, the flux $\phi(\vec{r}, E)$ must also represented this way. If $\vec{\boldsymbol{q}}$ is an N dimensional column vector and $\boldsymbol{R}$ is an $M \times N$ matrix, then $\phi(\vec{r}, E) \left[\frac{particles}{cm^2 \cdot MeV}\right] \rightarrow \boldsymbol{\phi}(\vec{r}) \left[\frac{particles}{cm^2}\right]$ where ${}^{e}\phi(\vec{r})$ is the e^{th} element of the M dimensional column vector $\boldsymbol{\phi}(\vec{r})$, and describes the scalar flux integrated over the boundary of energy group e,

$$ {}^{e}\phi(\vec{r}) = \int_{E_{e-1}}^{E_e} \phi(\vec{r}, E) dE. \qquad 3.9 $$

$\boldsymbol{\phi}(\vec{r})$ is discretized in space by calculating a energy discretized flux at various locations $\vec{r}$, ${}_{r}\boldsymbol{\phi}$. In one dimension where $r = |\vec{r}|$, calculation of $\boldsymbol{\phi}(r)$ for any intermediate r where r_j and r_{j+1} are the two nearest neighbors for which data is available, is done through interpolation. To approximate $\boldsymbol{\phi}(r)$, where $r_j < r < r_{j+1}$, a weighted average of ${}_{r_j}\boldsymbol{\phi}$ and ${}_{r_{j+1}}\boldsymbol{\phi}$ is taken from

$$\boldsymbol{\phi}(r) \approx \frac{(r_{j+1}-r)}{(r_{j+1}-r_j)}\ {}_{r_j}\boldsymbol{\phi} + \frac{(r-r_j)}{(r_{j+1}-r_j)}\ {}_{r_{j+1}}\boldsymbol{\phi}\,. \tag{3.10}$$

The interpolation used in equation 3.10 can be easily extended to higher dimensions.

Each of the ${}_{r}\boldsymbol{\phi}$ corresponding to the different locations requires the computation of a separate response function such that the response functions $\boldsymbol{R}$ are calculated at many spatial points, $\boldsymbol{R} \rightarrow {}_{r}\boldsymbol{R}$. Therefore, the response functions ${}_{r}\boldsymbol{R}$ describe the contribution from particles entering a region to a location $\vec{\boldsymbol{r}}$. The flux of particles at $\vec{\boldsymbol{r}}$ due to a source $\vec{\boldsymbol{q}}$ can be calculated from

$${}_{r}\boldsymbol{\phi} = {}_{r}\boldsymbol{R}\vec{\boldsymbol{q}}, \tag{3.11}$$

where the flux in energy bin e is,

$${}_{r}^{e}\phi = \sum_{n=1}^{N} {}_{r}^{e,n}R \cdot {}^{n}q, \tag{3.12}$$

and

$$\boldsymbol{\psi}\left(\vec{\boldsymbol{r}},\hat{\boldsymbol{\Omega}}\right) \approx {}_{r}\boldsymbol{\phi}\cdot\boldsymbol{f}\left(\hat{\boldsymbol{\Omega}}\right) = {}_{r}\boldsymbol{R}\vec{\boldsymbol{q}}\cdot\boldsymbol{f}\left(\hat{\boldsymbol{\Omega}}\right), \tag{3.13}$$

where

$${}^{e}\psi\left(\vec{\boldsymbol{r}},\hat{\boldsymbol{\Omega}}\right) = \int_{E_{e-1}}^{E_e} \psi\left(\vec{\boldsymbol{r}},E,\hat{\boldsymbol{\Omega}}\right)dE, \tag{3.14}$$

and $\boldsymbol{f}\left(\hat{\boldsymbol{\Omega}}\right)$ is a vector function representing $f(E,\hat{\boldsymbol{\Omega}})$ which has been discretized in energy in the same manner described above. If the entire problem is broken into I regions, the flux can be obtained by successive application of the appropriate response functions to the source,

$${}_{r}\boldsymbol{\phi} = {}_{r}\boldsymbol{\mathfrak{R}}_{I}\boldsymbol{R}_{I-1}\cdots\boldsymbol{R}_{i+1}\boldsymbol{R}_{i}\boldsymbol{R}_{i-1}\cdots\boldsymbol{R}_{2}\boldsymbol{\mathcal{R}}_{1}\vec{\boldsymbol{q}}. \tag{3.15}$$

The response functions $\boldsymbol{\mathcal{R}}$, $\boldsymbol{R}$, and $\boldsymbol{\mathfrak{R}}$ in equation 3.15 are written in different fonts to explicitly denote the different units of each response function as they operate on, and transform to, quantities with different units.

If the example presented in section 3.2 is discretized in this manner, the flux in the detector can be calculated from

$$_{b}\boldsymbol{\phi} = {}_{b}\boldsymbol{\mathfrak{R}}_{3}\boldsymbol{R}_{2}\boldsymbol{\mathcal{R}}_{1}\vec{\boldsymbol{q}}, \tag{3.16}$$

where $\boldsymbol{\mathcal{R}}_{1}$, $\boldsymbol{R}_{2}$, and ${}_{b}\boldsymbol{\mathfrak{R}}_{3}$ are the response functions corresponding to G_1, G_2, and G_3. If the detector shape, orientation, location, or materials composition were to be changed, $\boldsymbol{\mathcal{R}}_{1}$ and $\boldsymbol{R}_{2}$ would remain valid. The only change to equation 3.16 would be the need to change the response function ${}_{b}\boldsymbol{\mathfrak{R}}_{3}$ for one describing the new state of the detector. If the shielding material or thickness is changed, $\boldsymbol{\mathcal{R}}_{1}$ would remain valid, and ${}_{b}\boldsymbol{\mathfrak{R}}_{3}$ would as well assuming the new shielding configuration does not significantly change the angular distribution of the neutrons exiting the shield from what was assumed in the calculation of ${}_{b}\boldsymbol{\mathfrak{R}}_{3}$. In this case, all that would need to be done is to obtain a new $\boldsymbol{R}_{2}$ which describes the new shielding configuration.

Chapter 4

IMPLEMENTATION

This chapter presents the implementation details for the theory presented in chapter 3, applied to an AI system. Implementation details for each sub-model will be discussed individually, and benchmark results presented for sub-models which rely strongly on simplifying approximations that have been developed specifically for that sub-model. The work outlined in this chapter has been incorporated into the XPASS software [5] to extend its capabilities to cover AI systems. Appendix C gives the MCNPX (version 2.70) template decks used to generate the response function library for each sub-model.

4.1 Active Interrogation Problem Decomposition

The general AI problem can be dealt with by decomposing it into eight major sub-models: 1. the AI source, 2. vehicle/cargo (incident photons), 3. shielding (incident photons), 4. the SNM, 5. shielding (escaping neutrons), 6. vehicle/cargo (escaping neutrons), 7. the detector system, and 8. background radiation (terrestrial and cosmic). Several of the regions within the problem have two unique sub-model instances. The first instance is for particles coming in to interrogate the threat object, while the second instance is for transporting particles which are emitted from the SNM to the detector. Since these instances correspond to different points within the AI scenario, they are treated separately. For example, the first instance of the vehicle/cargo sub-model transports photons through the cargo and onto the threat object; the second instance transports neutrons, which were born in the threat object and have penetrated the shielding, through the cargo and to the detector. Similarly, the first instance of the shielding sub-model transports photons through the shielding and onto the SNM; and the

second instance transports neutrons, born in the SNM, outwards through the shielding and into the cargo while also reflecting neutrons back onto the SNM for reinterrogation.

The number and locations of the sub-models are chosen to represent natural breaking points in the generalized AI problem. This work focuses primarily on sub-models 1-4. Pre-existing response functions within XPASS [5], developed for passive interrogation systems, are used for sub-models 5-8 to transport neutrons from the SNM to the detector. The exception to this is in the second instance of the shielding sub-model (sub-model 5). In that sub-model, an updated algorithm for reflecting neutrons between the SNM and various layers of shielding material has been implemented, while still using the previously developed response functions. This change is outlined in section 4.7.1.

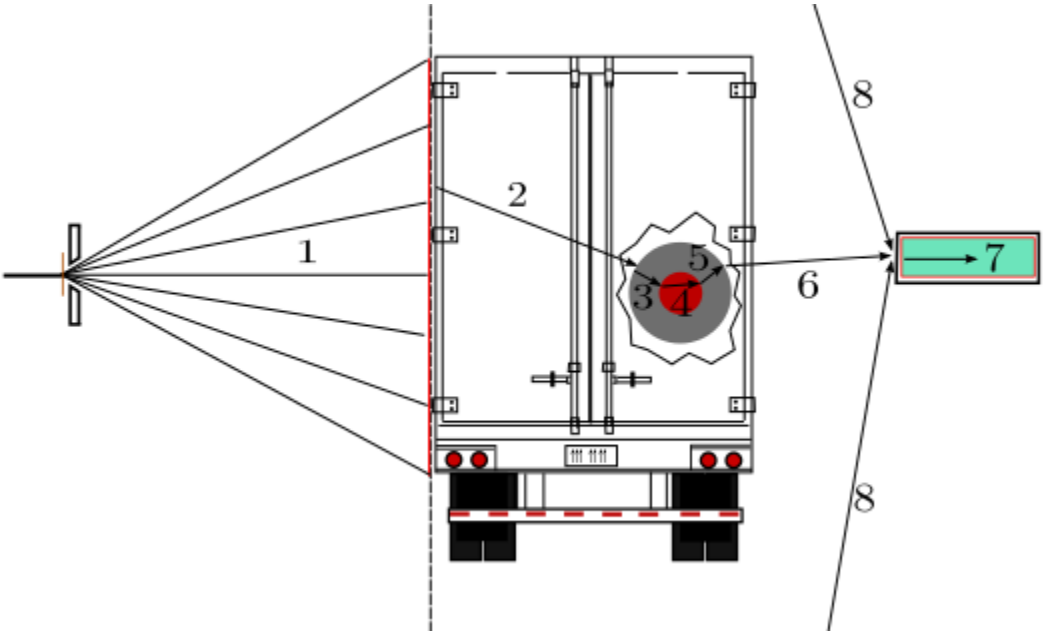

Figure 4.1: Active interrogation scenario decomposition into sub-models.

4.2 ACTIVE INTERROGATION SOURCE

4.2.1 AI Source Sub-model Definition

The AI source sub-model begins with a user defined electron source term $\vec{\boldsymbol{q}}$ [$\frac{electrons}{s}$]binned into energy groups. The source term $\vec{\boldsymbol{q}}$ can be written as $S \cdot \tilde{\boldsymbol{q}}$, where S is the source strength in units $\left[\frac{electrons}{s}\right]$, and $\tilde{\boldsymbol{q}}$ $[dimensionless]$ is a vector specifying the energy distribution of electrons across all energy groups, normalized to a single source electron. Since the entire problem is proportional to the electron source strength, the combined output of subsequent sub-models remain normalized to a unit source intensity when $\tilde{\boldsymbol{q}}$ is used. Multiplication of the normalized final result by the total electron source strength S yields the solution properly normalized to the absolute source strength.

A *source* response function $\boldsymbol{R}_{\gamma\leftarrow e}^{src}(T_{mat}, t, r_e, \vartheta)$[$\frac{photons/cm^2}{electron}$] is applied to $\tilde{\boldsymbol{q}}$ to transform the incident electron distribution into a distribution of the current density of bremsstrahlung photons on a plane at a distance (perpendicular to the face of the target) d_0 from the center of the bremsstrahlung target. The response function $\boldsymbol{R}_{\gamma\leftarrow e}^{src}$ is obtained by starting a source of electrons uniformly distributed within each energy bin of $\tilde{\boldsymbol{q}}$, with a Gaussian spatial distribution of radius r_e, and directed normally onto the center of a bremsstrahlung target of thickness t and material T_{mat}. The electron source has a unit intensity within each of the energy groups it is distributed over. The gamma current density, per source electron within each energy group, is tallied on concentric rings located on the plane at a reference distance d_0 from the target. This tally data is then divided by the area of each ring to generate response functions for a bremsstrahlung photon intensity at various divergence angles, ϑ, corresponding to the average radius of each ring.

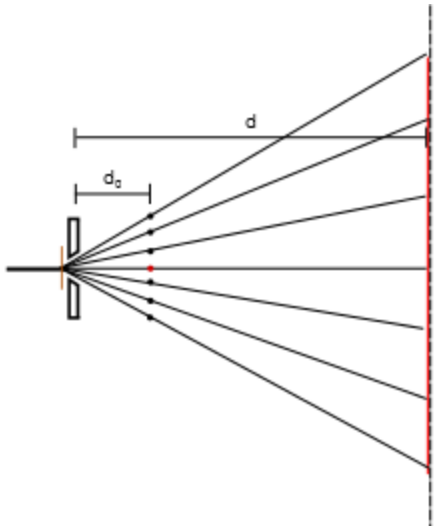

Figure 4.2: Diagram of the AI source sub-model**.**

The Source sub-model uses a simple model of a linear accelerator which includes only the electron beam and bremsstrahlung target. Directional information corresponding to the divergence of the photon beam is obtained by assuming the beam is directed radially outward from a point at the center of the target. This does not assume the beam is a point source emitting uniformly in all directions, as the intensity gradient of the photon beam as a function of divergence angle is explicitly captured in the response function. Collimators are not included so that the photon intensity at all forward directed angles can be tallied. Collimation of the photons is added by analytically collimating the beam during runtime. This analytic collimation is accomplished by allowing the user to specify a beam height and width, and truncating all photons which fall outside of the divergence angles defined by those beam parameters. While this method assumes a perfect collimator that produces no scatter, it allows for variable collimation without the need for a family of response functions that spans all potential collimation possibilities.

The response functions are generated at points, corresponding to different divergence angles from the beam axis, on a plane located at a reference distance d_0 from

the face of the bremsstrahlung target. The distance chosen for d_0 is arbitrary when collimators, which introduce scatter, are not included (as in this model). The photon current density at each divergence angle is calculated as opposed to the total current as it simplifies interpolation to divergence angles where data has not been stored. The total photon current over a small region is obtained by multiplying the photon current density at the center of the region by its area.

Calculation of Photon Intensity at any Point on a Plane

A 2D coordinate system is defined for all points in the geometry given in figure 4.3 (the third spatial dimension can be obtained via rotational symmetry) such that a point at the lower left vertex of the triangle is given by $(0,0)$, and a point at the top right vertex of the triangle is given by (d, r). If the interrogation object is a distance d from the center of the target, and the photon current density on beam axis at a reference point $(d_0, 0)$ is given by ${}^{0}_{d_0}\boldsymbol{j}'$, then the photon current density on the beam axis at any point $(d, 0)$ can be calculated (in a vacuum) from geometric attenuation by

$$\boldsymbol{j}'(d) = {}^{0}_{d_0}\boldsymbol{j}' \cdot \left(\frac{d_0}{d}\right)^2. \tag{4.1}$$

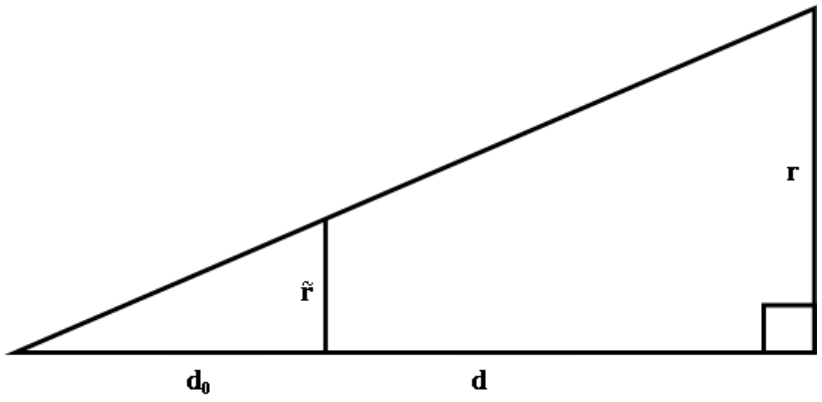

Figure 4.3: Geometry for defining a coordinate system for photon transport to the vehicle.

At a distance d from the target, the divergence of a realistic bremsstrahlung beam leads to a decreasing intensity on the plane as a function of the perpendicular distance r from beam axis. Rather than store this intensity data parameterized with respect to both r and d, a relative intensity map, $I(\frac{\tilde{r}}{d_0})$, is created on the plane located at the reference distance d_0 from the target and used to calculate the intensity at any point (d, r).

Using a simple geometric attenuation argument, it can be shown that the relative photon intensity between points (d, r) and $(d, 0)$ is the same as the relative intensity between points $(d_0, \tilde{r})$ and $(d_0, 0)$ in a vacuum; therefore, $I\left(\frac{r}{d}\right) = I\left(\frac{\tilde{r}}{d_0}\right)$. Knowing the relative intensities at $(d_0, \tilde{r})$ for various $\tilde{r}$, gives all the information needed to calculate the absolute intensities at various (d, r). Using the intensity map, the appropriate intensity factor can be applied to the current density $\boldsymbol{j}'(d)$ to obtain the absolute current density at any point (d, r). Specifying $\boldsymbol{j}'(d, 0)$ as the photon current density on beam axis at the point $(d, 0)$, so that

$$\boldsymbol{j}'(d, 0) \equiv \boldsymbol{j}'(d), \tag{4.2}$$

the current density at the point (d, r) can be calculated by

$$\boldsymbol{j}'^{(d,r)} = \boldsymbol{j}'^{(d,0)} I\left(\frac{r}{d}\right). \tag{4.3}$$

The method of analytically transporting photons on beam axis from $(d_0, 0)$ to $(d, 0)$ together with an intensity map generated at d_0 allows for calculation of the photon current density at any point (d, r). Interpolation between intensities at the various $\tilde{r}_i$where data has be stored within the intensity map produces an estimate of the relative intensity for all values of $\tilde{r}$ in the continuum.

Calculation of Energy Distribution at any Point on a Plane

In practice, equation 4.3 results in the correct intensity of the photons at (d, r), but the energy distribution is incorrect. Photons traveling in the forward direction have a higher mean energy than those which are more divergent. Without taking this into account, the high energy portion of the photon distribution, which is responsible for photonuclear interactions, will be overestimated at all divergence angles other than the forward direction. To account for the changing energy distribution with divergence angle, normalized energy distributions for each data point $(d_0, \tilde{r}_i)$ are generated and applied to the relative intensity map$I\left(\frac{\tilde{r}_i}{d_0}\right)$.

The source sub-model outlined here was broken into intensity and energy distribution components for ease of explaining the methodology. In practice, the relative intensity map and the energy distributions for each divergence angle are combined and can be obtained in a single MCNPX run. Calculation of the current density at any point (d, r) is accomplished by

$$\boldsymbol{j}'(d,r) = {}_{d_0}^{\tilde{r}}\boldsymbol{j}' \cdot \left(\frac{d_0}{d}\right)^2, \qquad 4.4$$

where ${}_{d_0}^{\tilde{r}}\boldsymbol{j}'$ is the absolute energy dependent current density at the point $(d_0, \tilde{r})$ which corresponds to the point of interest (d, r) through similar triangles. ${}_{d_0}^{\tilde{r}}\boldsymbol{j}'$ is obtained by applying the source response function $\boldsymbol{R}_{\gamma \leftarrow e}^{src}$ to the electron distribution $\tilde{\boldsymbol{q}}$, where $\boldsymbol{R}_{\gamma \leftarrow e}^{src}$ has the energy dependent intensity distributions embedded within.

Attenuation Through Air

The energy dependent photon current density $\boldsymbol{j}'(d, r)$ is calculated for a photon beam transporting through a vacuum. To add in the affects of air, $\boldsymbol{j}'(d, r)$ is analytically attenuated by using an effective removal cross section Σ_{eff} which takes into account absorption and scattering of photons out of the beam, and also takes into account photons

scattering into the beam at (d, r). Applying this attenuation factor, equation 4.4 then becomes

$$\boldsymbol{j}'(d,r) = {}_{d_0}^{\tilde{r}}\boldsymbol{j}' \cdot \left(\frac{d_0}{d}\right)^2 e^{-\Sigma_{eff} \cdot l}, \qquad 4.5$$

where $l^2 = r^2 + d^2$.

Response Function Generation

Generation of the source response data is simplified to due to the azimuthal symmetry of the beam. Due to this symmetry, the current density at any radial distance r from the beam axis is the same for all points rotated about the beam axis. The intensity map (containing both the absolute intensity and energy distribution) is created by placing a F1 current tally on a surface located at d_0 which is oriented perpendicular to the beam axis. The FS "tally segmenting" card is used to segment this tally into concentric rings which are useful for determining the photon intensity as a function of divergence angle. To obtain the current density, each of the segments is divided by the area of its respective ring. Since the data is tallied over a finite thickness ring, there is no single $\tilde{r}$ that corresponds to each of the tally segments. Therefore, each segment is assigned to the average radius of the ring over which the data corresponds to.

4.2.2 AI Source Sub-model Validation

Experimental Benchmarks

The source sub-model was benchmarked for typical use cases against experimental data found in the literature. The purpose of these benchmarks are to validate both the energy distribution and the absolute intensity of the photon beam generated within the source sub-model. The two experimental benchmarks were modeled based on work from Faddegon [28] and Starfelt [29]. These papers were chosen as the

experimental setup in each falls mostly within the scope of the source sub-model. To obtain the proper response functions, each of these experiments were simulated in MCNPX using parameters (tally locations, target thickness, normalizations, etc.) taken from work by Gierga [30].

In the work by Faddegon, the photon spectrum was measured on beam axis from monoenergetic 15 MeV electrons incident on a 8.501 mm thick Pb target (11.34 g/cm^3). In the experiment, the electron beam passes through both a thin Ti window and a Si beam monitor which are not present in the source sub-model. Because of this, it is expected that the results obtained through the sub-model will be qualitatively similar, but higher in intensity when compared to the experimental results.

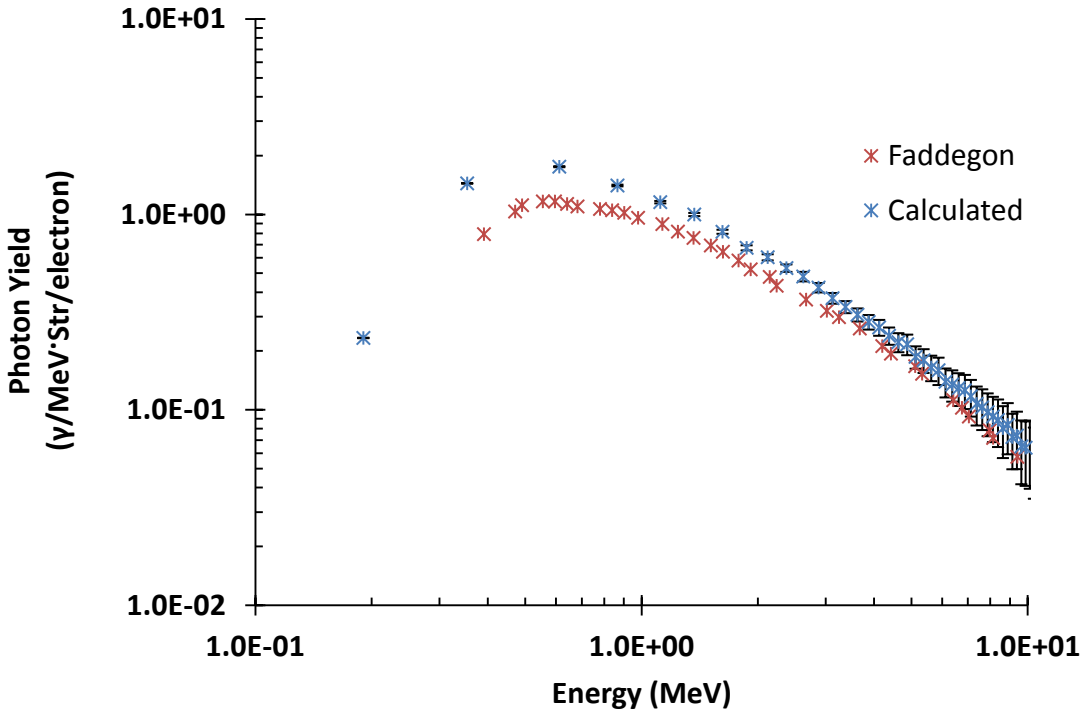

Figure 4.4: Absolute photon intensity on beam axis from 15 MeV electrons incident on a 8.501 mm thick Pb target, normalized to a single electron.

Figure 4.4 compares measured and calculated results for Faddegon's experiment. The lack of experimental details such as the Ti window and the Si beam monitor lead to a higher calculated result as compared to experiment, as expected. The integral source strength on beam axis was found to be $3.83 \pm 4.5\%$ $\left[\frac{\gamma}{Str \cdot electron}\right]$ for the calculated result, and 1.28 $\left[\frac{\gamma}{Str \cdot electron}\right]$ for the experimental result. This equates to about a factor of 3 difference between the calculated and experimental data.

A second benchmark against data from Starfelt was done to compare the energy spectrum of photons created by 9.66 MeV electrons incident on a 3.01 mm thick W target (19.24 g/cm^3). The paper does not give enough information to obtain a proper normalization factor, therefore the results obtain through the source sub-model were normalized to match the experimental data at a given point [30]. The integrated intensity was calculated to be $3.70 \times 10^5 \pm 0.4\%$ $\left[\frac{\gamma}{electron}\right]$ for the calculated case, and 3.62×10^5 $\left[\frac{\gamma}{electron}\right]$ from the experimental data. This equates to a 2.13% difference between the calculated and experimental data.

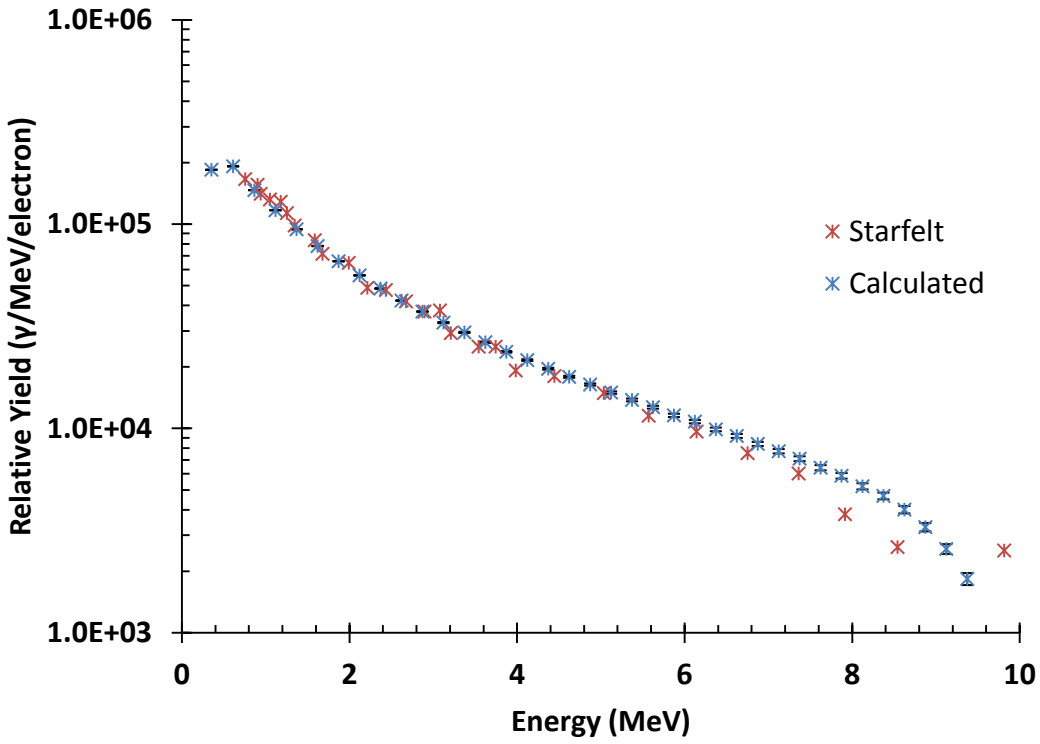

Figure 4.5: Comparison between experimental and computed photon energy spectrum from 9.66 MeV electron incident onto a 3 mm thick W target.

Computational Benchmarks

Validation of the intensity and energy distribution at points off axis was done by comparing the sub-model results to direct simulations in MCNPX. Response data was generated at $d_0 = 100$ cm for monoenergetic electrons of 20MeV. The high energy was chosen as bremsstrahlung photon production is increasingly forward directed at higher energies and should lead to the largest relative errors at large divergence angles. Concentric rings about the beam axis were used to segment the tally into 1 degree increments. A thick tungsten target (2.5 mm) was used as there will be maximum electron straggling. This was chosen to challenge the assumption of photons born at a point at the center of the target.

Using the response data generated as described above, the energy integrated photon current density at various points on a plane at $d = 200$ cm was calculated and compared to direct simulation in MCNPX; the error for all points was less than 2%.

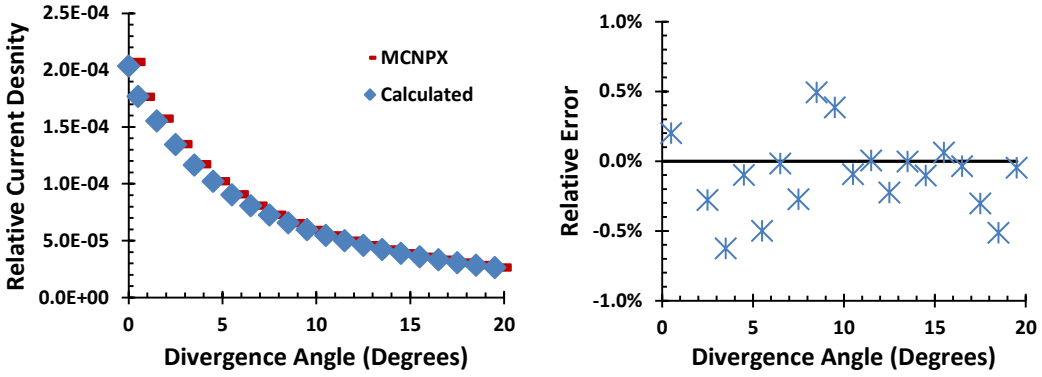

Figure 4.6: Photon current density at 200 cm from 20 MeV electrons incident onto a 2.5 mm thick W target.

The results presented above were calculated at divergence angles which correspond to where the response function data was generated, only at a larger value of *d*. To test the ability to compute the correct energy distribution at any divergence angle, a point off-axis that does not correspond to the location of the response function data was chosen. The point was chosen to be at a perpendicular distance $d = 175$ cm, and a radial distance r which corresponds to a divergence angle of 11 degrees off axis ($r = 34.017$ cm); 11 degree's was chosen as it lies exactly between two response functions located at 10.5 and 11.5 degrees and therefore will have the largest error from interpolation between response functions. A surface with a 1 cm^2 area was placed at this location for tallying in a direct simulation with MCNPX.

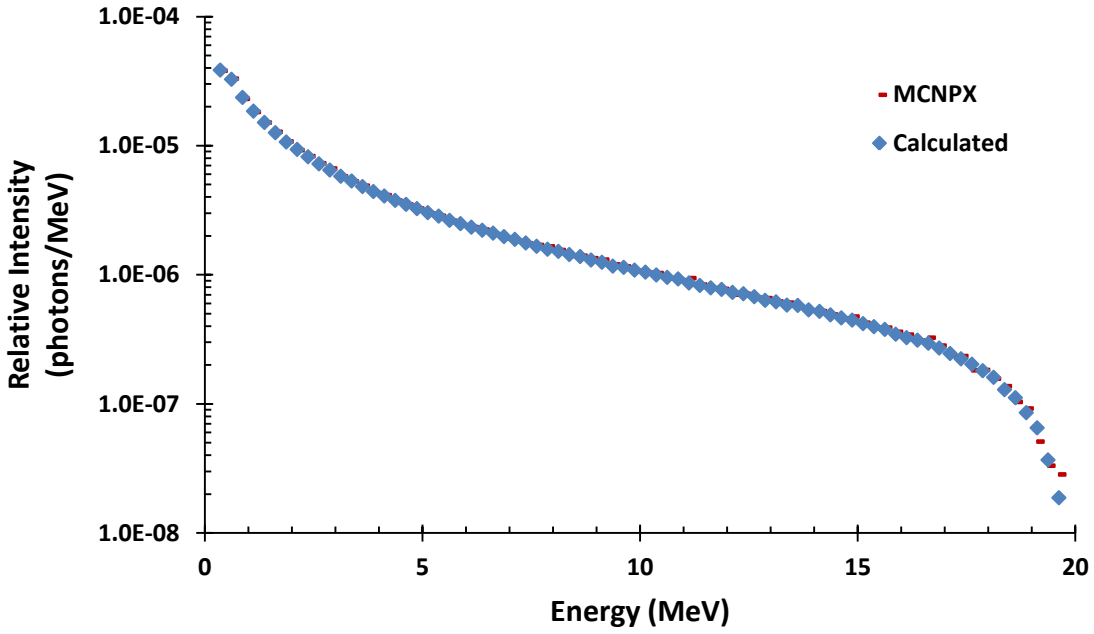

Figure 4.7: Energy distribution at 11 degrees off axis at $d = 175$ cmobtained from direct simulation with MCNPX and calculation with response functions.

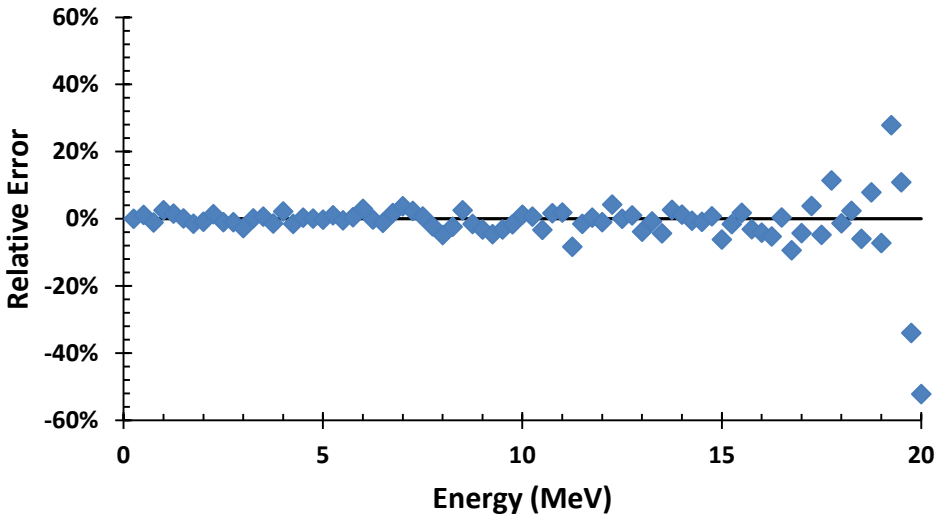

Figure 4.8: Relative error between results obtain via the source sub-model and direct calculation in MCNPX.

Comparison between the full simulation with MCNPX against calculation within the source sub-model shows that the differences in the spectra are small. Figure 4.8 shows the relative difference between these curves as a function of energy. The maximum error over all energy bins below 15 MeV is 4.23%, while the RMS error is 2.42%; energy bins above 15 MeV were not converged in the direct simulation and therefore were not considered. The RMS error of 2.42% for the difference between the source sub-model results and direct simulation results is comparable to the RMS error of 2.67% for all energy bins below 15MeV due to the statistical convergence of the MCNPX simulation. Comparison of the results is limited by the statistical convergence of the direct simulation. The oscillation of the error about zero in figure 4.8 is indicative of little systematic error.

Bounding Error Estimation

To obtain a bounding estimate for a realistic case, source sub-model parameters base upon a system [31][32] developed for active interrogation were used. Because the response functions are generated by averaging photon counts over a region that has an intensity gradient, calculation of point on beam axis should lead to the largest error. This is because the intensity gradient is largest in the forward direction so that the response functions should produce intensities that are lower than the true intensity. At points off axis, the gradient is not as severe and the response functions should produce intensities close to the true intensity (as was shown in the computational benchmarks section). To maximize the intensity gradient, 20 MeV electrons were used as opposed to the 10 MeV electrons from the literature. Additionally, a thick (1.5 mm) tungsten target was used to maximize electron straggling.

Figure 4.9 shows the results from simulating and calculating the bounding case. The energy integrated photon intensity was calculated to be $1.94 \times 10^{-4} \pm 0.161\% \left[\frac{\gamma}{electron}\right]$ from the source sub-model, and $2.05 \times 10^{-4} \pm 0.961\% \left[\frac{\gamma}{electron}\right]$ from direct simulation; these values represent an integrated error of -5.32% between the calculated and simulated intensities. The RMS error over all energy bins in the spectrum was found to be 6.91%, with the maximum error within any energy bin being 19.48%. The oscillation of the error about -5% in figure 4.10 indicates that the computed results are systematically about 5% lower than the direct simulation. This is likely due to the averaging over a large intensity gradient when generating the response function data as discussed previously. This can be reduced by implementing a higher density of response functions generated as a function of $\tilde{r}$.

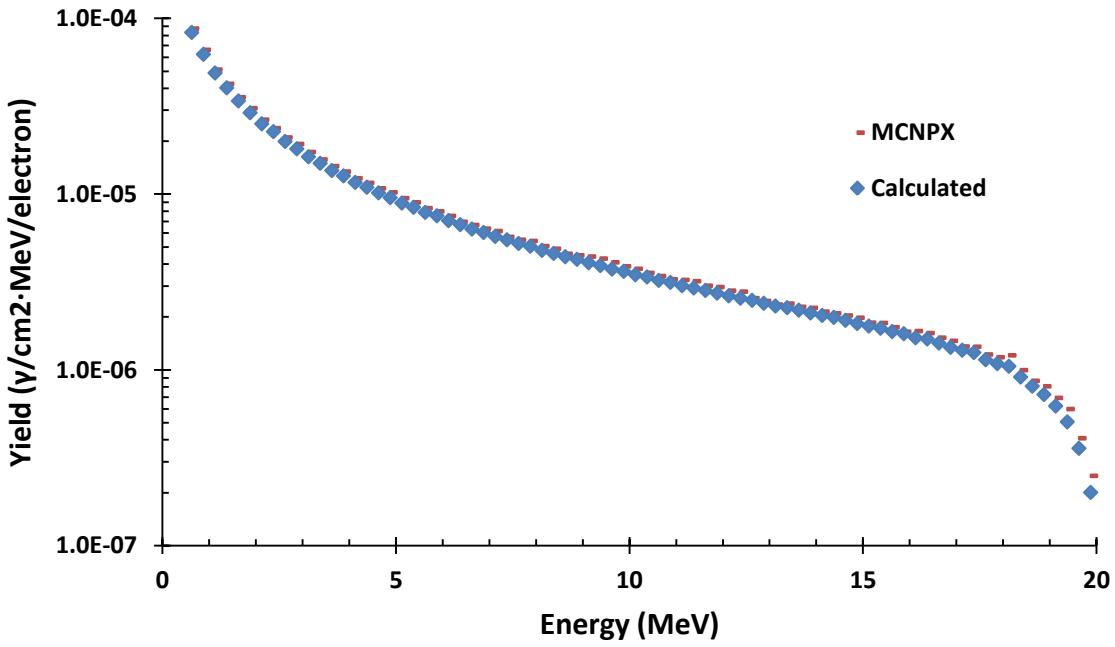

Figure 4.9: Computed photon spectrum at $d = 200$ cmfor the bounding case.

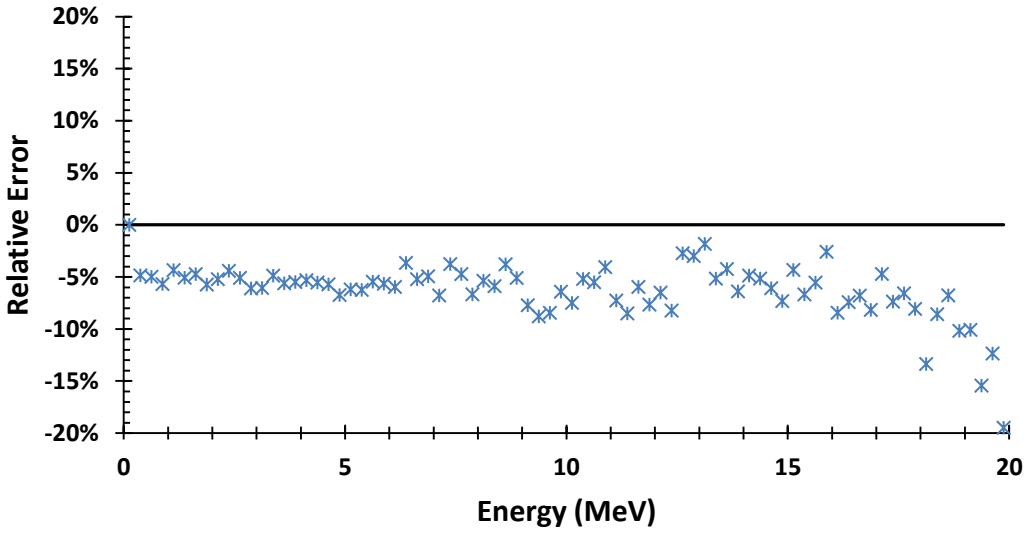

Figure 4.10: Relative difference between computed and simulated results for the bounding case.

4.3 AI CARGO SUB-MODEL

Before interrogation of the threat object, photons incident on the vehicle from the source must first transport through the bulk cargo to reach the surface of the threat object. The photon transport through the cargo is broken into uncollided and collided photons reaching the threat object. The transport is broken into these two components to better approximate the spatial and energy distribution of photons reaching the threat object. Uncollided photons are assumed to be distributed uniformly over the region of the threat object that directly intersects the beam, and collided photons are distributed uniformly over the entire surface of the threat object facing the beam. The assumptions on the spatial distribution of the photons are used to avoid introducing additional dimensions to the phase space encompassed by the cargo response function.

Two *cargo* response functions, $\boldsymbol{R}_{uncoll}^{cargo}(x', y', z', r, mat)$ $[\frac{uncollided\ photons}{photon}]$and $\boldsymbol{R}_{coll}^{cargo}(x', y', z', r, mat)$ $[\frac{collided\ photons}{photon}]$, are used to describe the two components of

photon transport through the cargo. These response functions give the total uncollided/collided photon current incident on the surface of a threat object of radius r, embedded within bulk cargo type mat at a point (x',y',z') relative to the center of a "beamlet" (a subsection of the full beam, see section 4.3.1), per photon within the beamlet. Since the photon transport is broken into collided and uncollided components, photons in subsequent sub-models are tracked via these two components as well. The results for collided and uncollided photons are computed separately and not combined until after the SNM sub-model where photo-neutrons are created. Photons that are uncollided may become collided during transport, however collided photons may never become uncollided.

In addition to photons, neutrons created within the cargo from photonuclear interactions can find their way to the threat object. A third *cargo* response function $\boldsymbol{R}_{p-n}^{cargo}(x',y',z',r,mat)$ $[\frac{neutrons}{photon}]$ describes the total neutron current incident on the threat object from neutrons created in the cargo, per photon within a beamlet. Again the location (x', y', z') is taken to be the center of the threat object relative to the center of the beamlet, r is the radius of the threat object, and mat is the bulk cargo material. The neutrons created in the cargo are assumed to be well scattered and therefore incident on the threat object uniformly from all directions. The neutron current is saved for use in the second instance of the shielding sub-model (sub-model 5) which transport neutrons from the SNM through the shielding. The neutrons born in the cargo neutrons are used as an initial condition at the boundary between the shield and cargo, and transported through the shielding and into the SNM using the updated iterative scheme outlined in section 4.7.1.

4.3.1 Cargo Sub-Model Definition

Photon Response Functions

The total photon current $\boldsymbol{j}^{\boldsymbol{cargo}}$ $[photons]$ entering the cargo is obtained by first calculating the photon current density $\boldsymbol{j}'^{\boldsymbol{cargo}}(x,y)$ $[photons/cm^2]$ anywhere along the cargo (obtained from the source sub-model). A large interrogation beam can be approximated by tiling smaller "beamlets" in a mosaic fashion. The total current in the large beam is then the superposition of the current from each beamlet. The total current for a given beamlet denoted by the indices m,n can be approximated by multiplying the current density at the center of the beamlet, $\boldsymbol{j}'^{\boldsymbol{cargo}}(x_n,y_m)$,by the area of the beamlet ${}^{m,n}A$. For beamlet $m,n,$ the total photon current incident over the beamlet is calculated by equation 4.6, where x_n and y_m are the coordinates associated with indices m and n, and ${}^{m,n}A$ is the area of the beamlet.

$$ {}^{m,n}\boldsymbol{j}^{\boldsymbol{cargo}} = \boldsymbol{j}'^{\boldsymbol{cargo}}(x_n,y_m)\,{}^{m,n}A\,. \qquad 4.6 $$

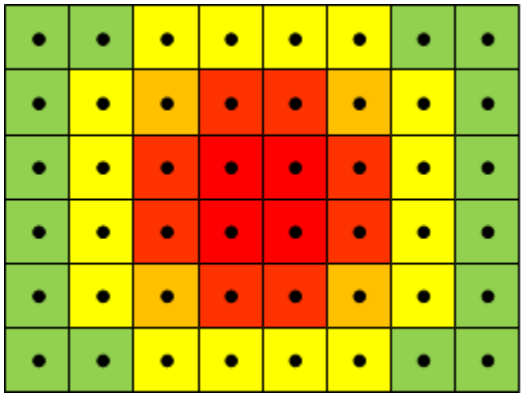

Figure 4.11: A macroscopic beam can be reconstructed by the superposition of a mosaic of smaller beamlets, each potentially having a different intensity.

With the separation of the collided and uncollided components of the total photon current on the threat object, the uncollided current incident on the threat object from beamlet m,n is

$$ {}^{m,n}\boldsymbol{j}_{uncoll}^{TO} = {}^{m,n}\boldsymbol{R}_{uncoll}^{\boldsymbol{cargo}\ m,n}\boldsymbol{j}^{\boldsymbol{cargo}}, \tag{4.7} $$

and the total uncollided current incident on the threat object from all beamlets is given by

$$ \boldsymbol{j}_{uncoll}^{TO} = \sum_{n=1}^{N}\sum_{m=1}^{M} {}^{m,n}\boldsymbol{R}_{uncoll}^{cargo\ m,n}\boldsymbol{j}^{\boldsymbol{cargo}}. \tag{4.8} $$

Similarly for the collided contribution,

$$ {}^{m,n}\boldsymbol{j}_{coll}^{TO} = {}^{m,n}\boldsymbol{R}_{coll}^{cargo\ m,n}\boldsymbol{j}^{\boldsymbol{cargo}}, \tag{4.9} $$

and

$$ \boldsymbol{j}_{coll}^{TO} = \sum_{n=1}^{N}\sum_{m=1}^{M} {}^{m,n}\boldsymbol{R}_{coll}^{cargo\ m,n}\boldsymbol{j}^{\boldsymbol{cargo}}. \tag{4.10} $$

Neutron Response Functions

High energy photons can produce neutrons as they transport through the bulk cargo material. These neutrons scatter within the cargo and may eventually make it to the threat object. The neutron current incident on the threat object, per incident photon within a beamlet, is calculated using the neutron response function $\boldsymbol{R}_{p-n}^{cargo}$ in a similar fashion as the photon calculations given above. Therefore, the neutron current incident on the threat object from beamlet m,n is calculated from

$$ {}^{m,n}\boldsymbol{j}_{n}^{TO} = {}^{m,n}\boldsymbol{R}_{p-n}^{\boldsymbol{cargo}\ m,n}\boldsymbol{j}^{\boldsymbol{cargo}}, \tag{4.11} $$

and the total neutron current from the superposition of all beamlets is given by

$$\boldsymbol{j}_n^{TO} = \sum_{n=1}^{N} \sum_{m=1}^{M} {}^{m,n}\boldsymbol{R}_{p-n}^{cargo\,m,n}\boldsymbol{j}^{\boldsymbol{cargo}} \,. \tag{4.12}$$

Response Function Generation

The response functions are generated by creating a semi-infinite cargo 260 cm thick (corresponding to the width of a trailer) within MCNPX. The use of a semi-infinite cargo neglects any edge effects that occur near the boundaries of the trailer. A photon source is distributed uniformly over a $2.5\ \text{cm} \times 2.5\ \text{cm}$ square region on the side of the cargo; this area defines the size of a beamlet. Spherical regions of various radii are placed throughout the cargo and F1 current tallies are placed on the surfaces to count the number of particles incident on each sphere. The F1 tallies use the tally tagging feature to segregate the uncollided photons from all other photons incident on the sphere. An additional F1 neutron current tally is placed on the sphere to count neutrons reaching the surface. Each of these tallies is divided into energy bins of the corresponding particle group structure to obtain the energy spectrum of the particles incident on the threat object.

The volume within each sphere is set to zero importance so that no particle which enters the sphere may leave. Because of the zero importance region, each sphere location and radius must be tallied on separate runs as the zero importance regions will kill particle which pass through one sphere that would have penetrated to a different sphere had the first not been present with zero importance.

4.4 SHIELDING SUB-MODEL

Once the photon currents $\boldsymbol{j}_{coll}^{TO}$ and $\boldsymbol{j}_{uncoll}^{TO}$ and the neutron current $\boldsymbol{j}_n^{TO}$ incident on the threat object are calculated, these particles must be transported through any shielding that may be present surrounding the SNM. The transport of photons through the

shielding remains separated into uncollided and collided photon components. The transport of neutrons through the shielding is done by setting $\boldsymbol{j}_n^{TO}$ as a boundary condition in the iterative scheme described in section 4.7.1. The shielding is modeled as layers of nested shells of possibly varying shield material.

Two *shield* response functions are used to describe the two components of photon penetration through each layer of shielding. These response functions are $\boldsymbol{R}_{Uncollided}^{Shield}(\boldsymbol{I}, r_{inner}, r_{outer}, \xi)$ $[\frac{uncollided\ photons}{photon}]$ and $\boldsymbol{R}_{Collided}^{Shield}(\boldsymbol{I}, r_{inner}, r_{outer}, \xi)$ $[\frac{collided\ photons}{photon}]$, where $\boldsymbol{I}$ is the isotopic vector of the shielding material, r_{inner} is the inner radius of the shield layer shell, r_{outer} is the outer radius of the shell ($r_{outer} - r_{inner}$ is equal to the total shielding layer thickness T), and ξ is a parameter that is useful for describing the portion of the shield under direct irradiation from the beam; ξ will be formally defined later in this section. Because the response function $\boldsymbol{R}_{Uncollided}^{Shield}$ describes the probability of a photon traversing the shielding without interacting, $\boldsymbol{R}_{Uncollided}^{Shield}$ is a square diagonal matrix when the source and destination photon energy group structures are the same.

Two additional *shield* response functions, $\boldsymbol{R}_{(\gamma,n)inner}^{Shield}(\boldsymbol{I}, r_{inner}, r_{outer}, \xi)$ $[\frac{neutrons}{photon}]$ and $\boldsymbol{R}_{(\gamma,n)outer}^{Shield}(\boldsymbol{I}, r_{inner}, r_{outer}, \xi)$ $[\frac{neutrons}{photon}]$, are needed to describe the neutrons that exit the inner and outer surfaces of the shielding due to photo-neutron production within. These photo-neutrons transport through the shielding and can interrogate the SNM, leading to increased induced neutron emission.

4.4.1 Shielding Sub-Model Definition

Photon Transmission Through Shield

The response function $\boldsymbol{R}_{Uncollided}^{Shield}$ applied to $\boldsymbol{j}_{uncoll}^{TO}$ gives the total *uncollided* photon current penetrating through a layer of shielding, $\boldsymbol{j}_{Uncollided}^{Shield}$. The response

function $\boldsymbol{R}_{Collided}^{Shield}$ applied to the total photon current incident on the shield layer, $\boldsymbol{j}^{TO} = \boldsymbol{j}_{uncoll}^{TO} + \boldsymbol{j}_{coll}^{TO}$, gives the total *collided* photon current penetrating the shielding, $\boldsymbol{j}_{Collided}^{Shield}$.

$$\boldsymbol{j}_{Uncollided}^{Shield} = \boldsymbol{R}_{Uncollided}^{Shield}\boldsymbol{j}_{uncoll}^{TO}\,, \tag{4.13}$$

$$\boldsymbol{j}_{Collided}^{Shield} = \boldsymbol{R}_{Collided}^{Shield}(\boldsymbol{j}_{uncoll}^{TO} + \boldsymbol{j}_{coll}^{TO})\,. \tag{4.14}$$

Equations 4.13 and 4.14 show how uncollided and collided photons are treated. Of the photons that penetrate through the shield, only those incident on the outer surface of the shield as uncollided photons can remain uncollided after penetration, while collided photons that penetrate through the shield can originate from either collided or uncollided photons incident on the shield.

When multiple layers of shielding are present, response functions ${}_{s}\boldsymbol{R}_{Uncollided}^{Shield}$ and ${}_{s}\boldsymbol{R}_{Collided}^{Shield}$, for each layer are used. If there are S layers of shielding present, there are $S + 1$ surfaces where the photon current must be computed. The inward directed photon currents at each shield surface are then ${}_{s}\boldsymbol{j}_{Uncollided}^{Shield}$ and ${}_{s}\boldsymbol{j}_{Collided}^{Shield}$, where ${}_{0}\boldsymbol{j}_{Uncollided}^{Shield}$ and ${}_{0}\boldsymbol{j}_{Collided}^{Shield}$ are located at the shield-SNM interface, and ${}_{S}\boldsymbol{j}_{Uncollided}^{Shield}$ and ${}_{S}\boldsymbol{j}_{Collided}^{Shield}$ are located at the cargo-shield interface. No photon backscatter coupling between multiple layers of shielding or between the shielding and SNM is considered due to the low probability for photons in the energy range of interest to undergo multiple backscatters. The boundary conditions for ${}_{S}\boldsymbol{j}_{Uncollided}^{Shield}$ and ${}_{S}\boldsymbol{j}_{Collided}^{Shield}$ are set to

$${}_{S}\boldsymbol{j}_{Uncollided}^{Shield} = \boldsymbol{j}_{uncoll}^{TO}\,, \tag{4.15}$$

$${}_{S}\boldsymbol{j}_{Collided}^{Shield} = \boldsymbol{j}_{coll}^{TO}\,. \tag{4.16}$$

Using the above definitions, the total uncollided photon current penetrating through all layers of shield is then calculated through

$$ {}_0\boldsymbol{j}^{Shield}_{Uncollided} = {}_0\boldsymbol{R}^{Shield}_{Uncollided}\ {}_1\boldsymbol{j}^{Shield}_{Uncollided}, \tag{4.17} $$

where ${}_1\boldsymbol{j}^{Shield}_{Uncollided}$ is calculated recursively through

$$ {}_s\boldsymbol{j}^{Shield}_{Uncollided} = {}_s\boldsymbol{R}^{Shield}_{Uncollided}\,{}_{s+1}\boldsymbol{j}^{Shield}_{Uncollided}. \tag{4.18} $$

For collided photons, the equivalent equations are

$$ {}_0\boldsymbol{j}^{Shield}_{Collided} = {}_0\boldsymbol{R}^{Shield}_{Collided}\ {}_1\boldsymbol{j}^{Shield}, \tag{4.19} $$

and

$$ {}_s\boldsymbol{j}^{Shield}_{Collided} = {}_s\boldsymbol{R}^{Shield}_{Collided}\,{}_{s+1}\boldsymbol{j}^{Shield}, \tag{4.20} $$

where

$$ {}_s\boldsymbol{j}^{Shield} = {}_s\boldsymbol{j}^{Shield}_{Uncollided} + {}_s\boldsymbol{j}^{Shield}_{Collided}. \tag{4.21} $$

After having penetrated through the shielding, uncollided photons continue traveling in their original path where they are sent directly to the SNM sub-model. The collided photons are sent to the SNM sub-model where they are uniformly redistributed as a monodirectional plane source that irradiates the full surface of the SNM facing the beam. Redistributing the collided photons across the surface of the SNM in this fashion is an approximation used to replicate the spreading of the photon beam after scattering in the shielding. This is done to simplify the phase space by avoiding explicitly retaining spatially dependent data in the response functions $\boldsymbol{R}^{Shield}_{Uncollided}$ and $\boldsymbol{R}^{Shield}_{Collided}$. Figure 4.12 gives a graphical depiction of how this is modeled within the SNM sub-model.

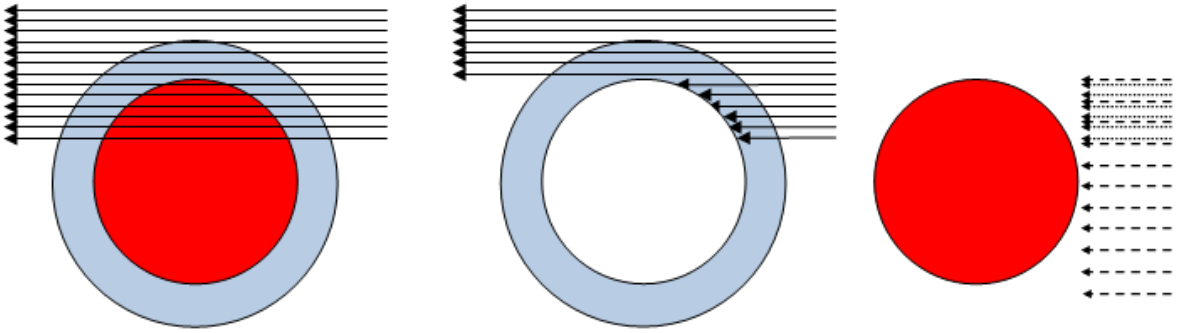

Figure 4.12: *Left*: Depiction of the physical scenario replicated within the shielding and SNM sub-models. *Middle*: The shielding sub-model calculates the total number of photons, broken into uncollided and collided components, penetrating the shielding into a central void. *Right*: The results from the shielding sub-model are passed to the SNM sub-model where the photons are modeled as a combination of uncollided photons traveling along the original path, and collided photons distributed across the front face of the SNM.

Photon Response Function Generation

The photons incident on the shield from the cargo are assumed to be a mono-directional planar source of finite extent equal to the cross-sectional area of the interrogation beam. Since the beam may only partially intersect the threat object, an angle ξ is used to define the portion of the threat object under direct irradiation. Figure 4.13 defines the angle $\xi \in [\frac{-\pi}{2}, \frac{\pi}{2}]$ which is used for calculating the position of the beam edge over the shield (or SNM when used in the SNM sub-model), relative to the center of the threat object. Since ξ is dependent upon the outer radius of the sphere, each layer of a nested shield configuration corresponds to a different value of ξ (see figure 4.13). The relationship between the angle ξ, the perpendicular distance of the beam edge to the center of the threat object $h \in [-r, r]$, and the outer radius r is given by

$$h = r\sin(\xi)\,. \qquad 4.22$$

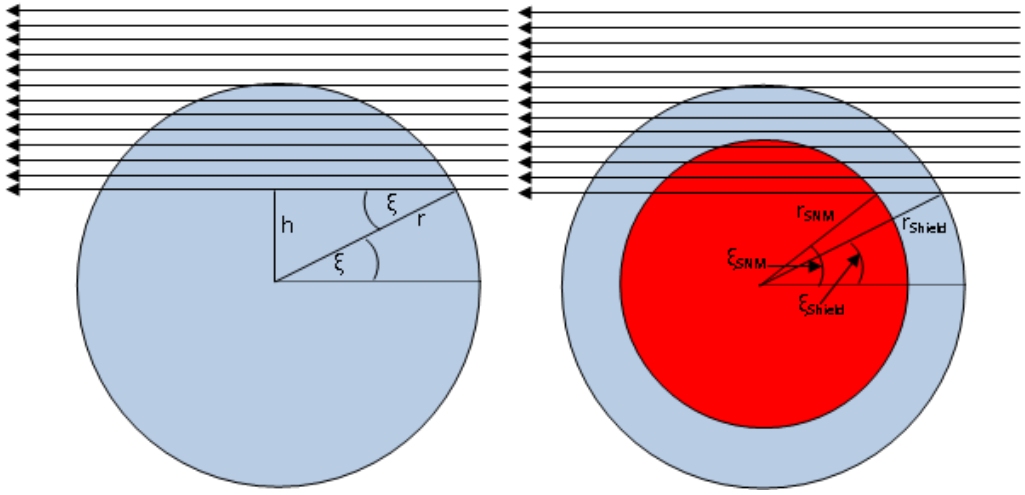

Figure 4.13: *Left*: definition of the angle ξ used within the shielding and SNM sub-models. *Right*: For SNM (red) surrounded by a layer of shielding (blue), the value of ξ differs for the SNM and each layer of shielding due to the differing outer radii.

The response functions $\boldsymbol{R}^{Shield}_{Uncollided}$ and $\boldsymbol{R}^{Shield}_{Collided}$ are generated by starting a planar source of photons, of unit strength and uniformly distributed within each photon energy group, incident on the shield. An F1 photon current tally is placed on the inner surface of the shield along with a region of zero importance to terminate photons that penetrate through the shield. The zero importance region is used to ensure that photons that make it through the shield do not score multiple times to the tally. Tally tagging is used to separate out the uncollided source photons from all other photons that contribute to the tally. The uncollided photons that reach the tally make up $\boldsymbol{R}^{Shield}_{Uncollided}$, while the remainder are considered collided photons (which will include any secondary photon production within the shielding as well) and make up the response function $\boldsymbol{R}^{Shield}_{Collided}$.

Generation of the response functions over all permutations is done by first fixing the inner radius, r_{inner}, of the shield at the smallest value of interest and setting the outer radius, r_{outer}, to r_{inner} plus the minimal thickness T_{min} of the shield being considered. A response function is created for this case and r_{outer} is increased while keeping r_{inner} fixed.

This process is repeated until r_{outer} - r_{inner} is equal to the maximum shielding thickness, T_{max} , being considered. After this is completed, r_{inner} is increased and response functions for all r_{outer} from $r_{inner} + T_{min}$ to $r_{inner} + T_{max}$ are created.

Once each of these response functions has been generated for all combinations of inner and outer shielding radii, the process is repeated for various ξ from $\frac{-\pi}{2}$ to $\frac{\pi}{2}$. Response functions for each ξ, are generated by shifting the interrogation beam relative to the center of the shield. This entire process is repeated for each shielding material type being considered. Renormalization of the generated tally results must be done to ensure that the response functions are normalized to a single photon that intersects the shield, as some source photons in the MCNPX source may not be intersect the shielding, depending on how the source term and geometry are specified.

Photo-Neutron Production within Shielding

Photo-neutron production within the shielding can become a non-trivial factor for active interrogation when high Z shielding is used. The photo-neutrons produced in the immediate vicinity of the SNM from photon interactions within the shield have a high likelihood of reaching the SNM. When this occurs, the total neutron production in the SNM from neutrons born within the shielding becomes a significant fraction of all neutrons produced.

Photo-neutron production and transport within the shielding is handled in a similar fashion as the collided component of photon transport through the shielding. The response function $\boldsymbol{R}^{Shield}_{(\gamma,n)inner}$ applied to $\boldsymbol{j}^{TO}$ results in the current of neutrons exiting the inner surface of the shield, ${}^{\boldsymbol{n}}\boldsymbol{j}^{Shield}_{inner}$, from photo-neutrons produced within the shield; the response function $\boldsymbol{R}^{Shield}_{(\gamma,n)outer}$ applied to $\boldsymbol{j}^{TO}$ results in the current of neutrons exiting the outer surface of the shield, ${}^{\boldsymbol{n}}\boldsymbol{j}^{Shield}_{outer}$, from photo-neutrons produced within the shield.

Response functions for neutron leakage through both the inner and outer surfaces are needed as neutrons exiting the outer surface can be reflected inwards from an outer layer of shielding, if present. When multiple layers of shielding are present

$$ {}^{n}_{s}\boldsymbol{j}^{Shield}_{inner} = {}_{s}\boldsymbol{R}^{Shield}_{(\gamma,n)inner\,s+1}\boldsymbol{j}^{Shield}, \tag{4.23} $$

$$ {}^{n}_{s+1}\boldsymbol{j}^{Shield}_{outer} = {}_{s}\boldsymbol{R}^{Shield}_{(\gamma,n)outer\,s+1}\boldsymbol{j}^{Shield}. \tag{4.24} $$

The neutrons produced within each layer of shielding are not transported to the SNM within this sub-model. The neutrons at the surface of each shielding layer are stored for use as boundary conditions in the reflection iteration scheme described in section 4.7.1.

Neutron Response Function Generation

The response functions $\boldsymbol{R}^{Shield}_{(\gamma,n)inner}$ and $\boldsymbol{R}^{Shield}_{(\gamma,n)inner}$ are created using the same method as $\boldsymbol{R}^{Shield}_{Collided}$ and $\boldsymbol{R}^{Shield}_{Uncollided}$. The only difference is the F1 current tally is now a neutron tally, and tally tagging is not used.

4.4.2 Shielding Sub-Model Validation

During creation of the shielding sub-models' response functions, the total number and the energy distribution of the photons penetrating through the shield, as well as photo-neutrons produced within the shield are conserved. The position and angular distributions of the photons outputted from the shielding sub-model are an approximation of the true distributions. By making assumptions on the spatial and angular distributions, the average distance a photon travels through the SNM before exiting is affected, leading to a change in the total photonuclear interaction probability (see section 4.5.1 for a discussion on the average chord length).

Due to the approximations discussed above, validation of the shielding sub-model involved calculating the photo-neutron production within the SNM based upon the

assumptions, and comparing this to the photo-neutron production obtained from a direct simulation. To accomplish this, the photo-neutron production within the SNM was calculated for direct irradiation of a shielded threat object with high energy photons within MCNPX. A second MCNPX simulation was done where the SNM (unshielded) was irradiated with the collided and uncollided photon distributions obtained from the shielding sub-model. The photo-neutron productions from these simulations were compared for validation of the shielding sub-model.

Neutron Production in 1cm Radius HEU

A scenario chosen to be representative of a typical scenario was a 1 cm radius sphere of HEU surrounded by 5 mm of Pb shielding that was irradiated with high energy photons. The photon energy was uniformly distributed between 19.5 MeV and 20 MeV, as this corresponds to the highest energy bin within the group structure used. The primary photo-neutron production within the HEU was obtained in a direct MCNPX simulation and compared against the value obtained using the photon distributions from the shielding sub-model. The total energy-integrated primary photo-neutron production was found to be $1.54 \times 10^{-3} \frac{primary\ photo-neutrons}{photon}$ from direct simulation, and calculated to be $1.51 \times 10^{-3} \frac{primary\ photo-neutrons}{photon}$ from the shielding sub-model; this equates to an integral error of -1.96%. The average error across all converged energy bins was -2.69%, with an RMS error of 15.41%.

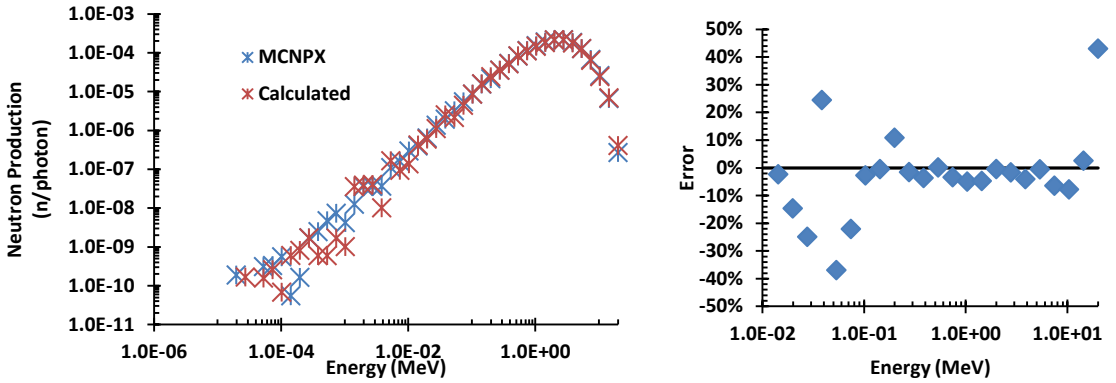

Figure 4.14: Primary photo-neutron production within 1 cm of HEU shielded with 5 mm of Pb from high energy photon interrogation.

The calculated results being systematically low by 4.9% make sense in context of the assumptions on the photon distributions. The contribution from the uncollided photons should be nearly correct as the distributions in energy, direction, and position are close to the physical reality. Therefore, the majority of the systematic error associated with the shielding sub-model should be a result of bias in how the collided photons are treated. In this validation scenario, a majority of the photons which reach the SNM were uncollided. Therefore, most of the contribution to the photo-neutron production was from the uncollided photons whose treatment is much closer to reality, and only a small fraction of the production was from the collided photons.

The response function calculation is systematically low because of the redistribution of the collided photons. In the direct simulation, photons traveling through the shield along the center see a shorter path length through the shield before reaching the SNM as compared to those photons entering either above or below the center. This causes a photon intensity gradient at the inside surface of the shield, with the center being most intense. In addition to having a higher intensity, the photons at the center also see a longer average path length through the SNM, and therefore have a higher likelihood of

interacting and producing a photo-neutron as compared to those near the edges. Redistribution of the collided photons to create a uniform intensity profile causes the collided photons to have a lower average path length through the SNM, and the probability of causing photo-neutron emission is reduced.

Bounding Error Estimation

To obtain a bounding estimate for the error introduced by the shielding sub-model, the neutron production from interrogation of a large heavily shielded threat object was calculated and compared to direct simulation. The large size was chosen to maximize the error caused by the uniform redistribution of the collided photons. A thick layer of shielding around the SNM was chosen to minimize the uncollided portion of photons penetrating the shield, and therefore maximize the relative fraction of collided photons penetrating through. An 8 cm radius sphere of HEU shielded with 50 cm of Pb was chosen as the threat object for the bounding case. HEU was chosen over WGPu because it can achieve a larger radius before criticality is reached.

The neutron production from high energy photons uniformly distributed between 14.387 MeV and 20 MeV was calculated and compared to direct simulation as described in the previous validation. The total primary photo-neutron production was found to be $3.57 \times 10^{-17} \frac{primary\ photo-neutrons}{photon}$ from direct simulation, and calculated to be $3.07 \times 10^{-17} \frac{primary\ photo-neutrons}{photon}$ from the shielding sub-model; this equates to an error of -14.1%. The average error across all converged energy bins was *-19.7%*, with an RMS error of 25.7%.

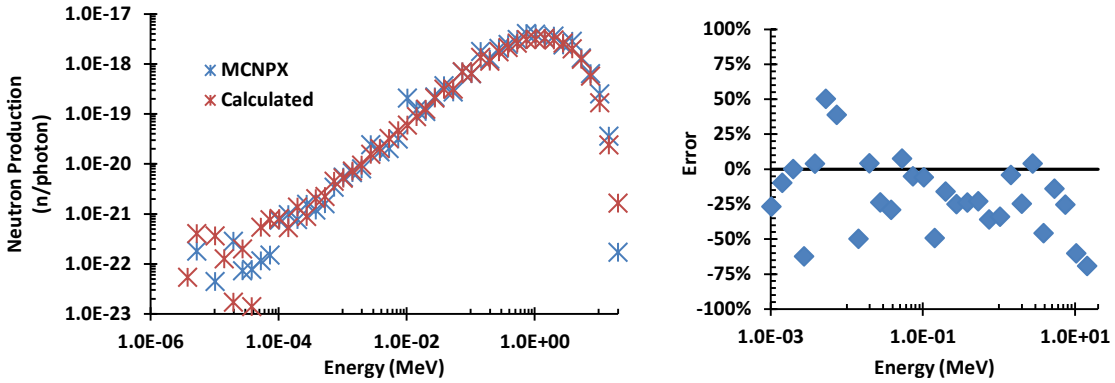

Figure 4.15: Simulated and calculated photo-neutron production in limiting case.

4.5 SNM SUB-MODEL

The SNM sub-model takes the current of collided and uncollided photons which penetrate through the shielding and returns the total neutron current exiting the surface of the SNM. The sub-model first takes the photon spectra exiting the shielding and entering the SNM, ${}_0\boldsymbol{j}^{Shield}_{Uncollided}$ and ${}_0\boldsymbol{j}^{Shield}_{Collided}$, and transports these photons through the SNM. During this transport, primary photo-neutrons are created within the SNM primarily through photofission and (γ,n) reactions. The response function which transports photon through the SNM and creates primary photo-neutrons is $\boldsymbol{R}^{SNM}_{nProduction}(\boldsymbol{I}, ACL)$ $[\frac{primary\ photo-neutrons}{photon}]$; where $\boldsymbol{I}$ is the SNM isotopic vector and ACL is the average chord length of the irradiation distribution (defined in section 4.5.1).

Once the primary photo-neutron production within the SNM is calculated, these neutrons are transported through the SNM to the surface. During transport, neutrons are lost from absorption events, and neutrons are produced from fission and (n,xn) reactions. The response function that handles the neutron transport to the surface of the SNM is $\boldsymbol{R}^{SNM}_{Escape}(\boldsymbol{I}, r, \xi)$ $[\frac{neutrons}{primary\ photo-neutron}]$, where ξ is the angle describing the portion of the SNM under irradiation (defined in section 4.4.1), and r is the radius of the SNM.

4.5.1 SNM Sub-Model Definition

After the distribution of particles incident on the SNM is calculated from the shielding sub-model, the particles are transported into the SNM where they stimulate the release of neutrons via photofission and (γ,xn) reactions. Attenuation of the photon beam when can be significant due to the high density of SNM. This leads to a higher neutron production rate on side of the SNM directly facing the beam relative to the opposite side. Figure 4.16 shows this effect and how it becomes more pronounced as the radius of the SNM increases. A complete treatment of this effect requires tracking of the spatial dependence of the flux incident on the SNM, which would significantly expand the phase space covered by the response functions.

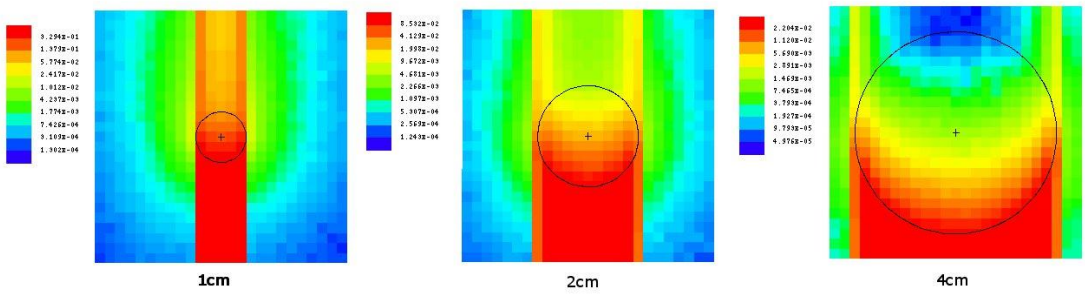

Figure 4.16: Photon intensity for a beam incident on SNM is significantly attenuated as the radius of the SNM increases. Results for SNM of radius 1, 2, and 4cm.

To avoid explicitly tracking the spatial distribution of particles incident on the surface of the SNM, a method of matching the average chord length (ACL) of photon transport through the SNM has been developed. The aim of matching the ACL is to obtain the correct total primary photo-neutron production by matching total interaction probabilities. This is accomplished by transporting particles with pre-defined spatial and angular distributions into the SNM. Matching the ACL of the pre-defined distributions

used in the response functions to that of the true incident distribution is an attempt to conserve the average distance traversed through the SNM by a photon before exiting the SNM. Conserving this path length conserves the total interaction probability as well.

Once the total primary photo-neutron production is calculated, the neutrons are uniformly distributed throughout the SNM over the region corresponding to the portion of the sphere under direct irradiation. The neutrons are then allowed to transport and leak through the surface of the sphere, or be absorbed with the possibility of creating additional neutrons.

Average Chord Length

For a given fixed irradiation distribution, the ACL for a circle (2D) or a sphere (3D) only depends on the radius of the SNM. A reference irradiation case is chosen and the *SNM* response function $\boldsymbol{R}_{nProduction}^{SNM}$is generated which describes the total primary photo-neutron production within the SNM (isotopic vector described by $\boldsymbol{I}$) for various ACLs of the reference irradiation distribution. Since the reference irradiation distribution is fixed, the only free parameter available to obtain response functions for various ACLs is the radius of the SNM.

To make use of $\boldsymbol{R}_{nProduction}^{SNM}$, the ACL is calculated for the true irradiation distribution present in the scenario. The associated response function is determined by adjusting the radius of the SNM of the reference distribution in the response function data until the ACL matches that of the true distribution. The response function for this radius/ACL is used to obtain the total number and energy distribution of the primary photo-neutrons created in the SNM.

A*CL Calculation*

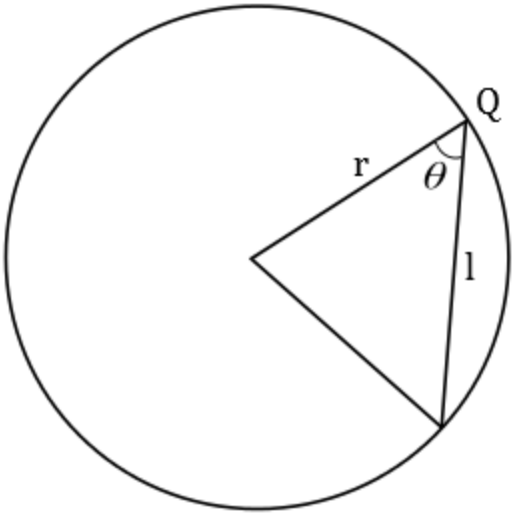

Figure 4.17: Chord length l for a particle entering the SNM at point Q heading in a direction ϕ relative to the inner surface normal.

For a 2D circular geometry, the length, *l*, of the chord going from a point Q on the surface of the circle to some other point on the surface is given by

$$l = 2r\cos(\theta). \tag{4.25}$$

If particles are incident on the SNM with a distribution *P(θ)* at *Q*, then the average length of all chords emanating from Q is

$$\bar{l} = \frac{\int_0^{\pi} 2r\cos(\theta)P(\theta)d\theta}{\int_0^{\pi} P(\theta)d\theta}. \tag{4.26}$$

Equation 4.26 can be integrated over all points on circle, weighted by the intensity of the beam at each point, to obtain the average chord length $\bar{L}$ for a distributed irradiation. For a beam centered on the circle, the angular distribution entering at any point on the surface is a delta function. Integration equation 4.26 over the face of the circle irradiated by the beam, with the appropriate cosine weighting to take into account

the reduced beam intensity away from the center of the beam, results in an average chord length of

$$\bar{L} = \frac{\pi r}{2}. \tag{4.27}$$

For a circle uniformly irradiated with a cosine weighted angular distribution, the average chord length is

$$\bar{L} = \frac{4r}{3}. \tag{4.28}$$

Equation 4.26 has been derived generally for any surface weighting distribution *P(θ)*. The results obtained by integrating equation 4.26 over the surface of a circle for a beam irradiation and a cosine distributed uniform irradiation match results published in the literature [33].

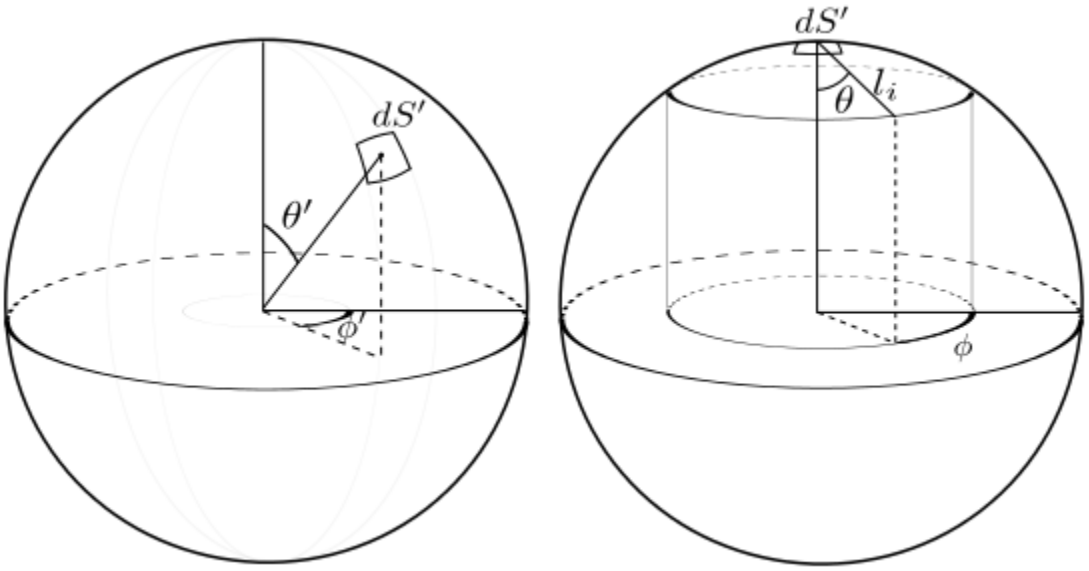

Figure 4.18: 3D spherical geometry for calculation of the average chord length through a sphere. *Left*: The surface element dS' is specified by use of a fixed primed coordinate system. *Right*: A second unprimed coordinate system is created at dS'.

In a spherical 3D geometry, the ACL is calculated in a similar fashion. First, the average length of all chords emanating from a differential surface element dS' is calculated. For this calculation, a local coordinate system at dS' is defined (see figure 4.18). The length of any chord originating from dS' is only dependent on θ, as chords with any ϕ have the same length for a given θ. Therefore, length of any chord originating from dS' is

$$l = 2r\cos(\theta), \tag{4.29}$$

and the average length of all chords, $\bar{l}$, is calculated from

$$\bar{l} = \int l \cdot P(l)dl = \frac{\int l \cdot \tilde{P}(l)dl}{\int \tilde{P}(l)dl} = \frac{\int_0^{2\pi}\int_0^{\pi} 2r\cos(\theta)\tilde{P}(\theta)d\theta d\phi}{\int_0^{2\pi}\int_0^{\pi} \tilde{P}(\theta)\, d\theta d\phi}. \tag{4.30}$$

Since l is independent of ϕ, integration over ϕ results in a factor of 2π in both the numerator and denominator, which is canceled out and reduces equation 4.30 to that of the 2D case for a circle.

To obtain the ACL, $\bar{L}$, of all chords from the entire surface of the sphere, a weighted average of $\bar{l}$ is taken by integrating $\bar{l}$ over the surface S'weighted by the relative intensity at each surface element.

$$\bar{L} = \int_{S'} \bar{l}(S') \cdot P(S')dS' = \frac{\int \bar{l}(S') \cdot \tilde{P}(S')dS'}{\int \tilde{P}(S')dS'}. \quad 4.31$$

For a uniform beam irradiating a sphere, $P(S') = \cos(\theta')$, and the ACL is calculated to be

$$\bar{L} = \frac{4r}{3}, \quad 4.32$$

which matches the result found in the literature [34]. In addition, the ACL for a sphere uniformly irradiated with a cosine distribution (used for the reference distribution) is calculated to be the same value

$$\bar{L} = \frac{4r}{3}. \quad 4.33$$

The angle ξ, defined in section 4.4.1, is convenient for calculating the position of the beam edge relative to the SNM center. The use of ξ is convenient as $\xi \in [\frac{-\pi}{2}, \frac{\pi}{2}]$ and is independent of the radius of the SNM. The portion of the SNM within the beam is parameterized as a function of ξ, and is calculated from the distance of the beam to the center of the SNM (h, see figure 4.13) and the radius of the SNM r. The relationship between h, r, and ξ is given by

$$h = rsin(\xi), \quad 4.34$$

where $h \in [-r, r]$.

The ACL for a sphere of radius r that is irradiated with a beam of photons, where the portion of the SNM under irradiation is described by ξ, is calculated from

$$ACL(\xi) = \frac{\pi r}{12} \cdot \left[\frac{9(1 - \cos(\xi)) - (1 - \cos(3\xi))}{\xi - \sin(\xi)\cos(\xi)} \right]. \quad 4.35$$

The primary photo-nuclear production within the SNM is obtained by applying the response function $\boldsymbol{R}_{nProduction}^{SNM}$ to the current of photons entering the SNM from the shielding. Since the transport is broken into collided and uncollided photons and the spatial distributions of these components are not equal, the same response function cannot be applied to the total current as the collided and uncollided components have different ACLs. The total number of primary photo-neutrons produced from uncollided photons is

$$\boldsymbol{j}_{Uncollided}^{SNM-nProduction} = {}_{ACL}\boldsymbol{R}_{nProduction}^{SNM}\, {}_{0}\boldsymbol{j}_{Uncollided}^{Shield}, \quad 4.36$$

and the total number of primary photo-neutrons produced from collided photons is

$$\boldsymbol{j}_{Collided}^{SNM-nProduction} = {}_{ACL^*}\boldsymbol{R}_{nProduction}^{SNM}\, {}_{0}\boldsymbol{j}_{Collided}^{Shield}, \quad 4.37$$

where ACL^* denotes the ACL for $\xi = \frac{\pi}{2}$, indicating the collided photons are distributed over the entire front surface of the SNM.

Response Function Generation

To generate the data for the response function $\boldsymbol{R}_{nProduction}^{SNM}$, a reference irradiation distribution must be chosen. In the SNM sub-model, the reference irradiation was chosen to be a sphere uniformly irradiated with a photon current having a cosine weighted angular distribution. Under this scenario, the ACL is calculated to be

$$\mathrm{ACL} = \frac{4r}{3}, \tag{4.38}$$

from equation 4.31. In general, the ACL of a sphere of radius r uniformly irradiated with a cos^n weighted source is

$$\mathrm{ACL} = 2r\frac{n+1}{n+2}. \tag{4.39}$$

Taking the limit as $n \to \infty$, the angular distribution becomes a delta function where all photons travel along the inward directed surface normal. In this case, equation 4.39 reduces to

$$\mathrm{ACL} = \lim_{\mathrm{n}\to\infty} 2r\frac{n+1}{n+2} = 2\mathrm{r}\,, \tag{4.40}$$

which says that the average distance a photon will travel before exiting the SNM, if it does not interact, is equal to the diameter of the SNM.

A sphere of SNM with isotopic vector $\boldsymbol{I}$ is created within MCNPX and a cosine weighted photon source is uniformly distributed over the surface. The source photons are generated at energies uniformly distributed within each group of the photon group structure. $\boldsymbol{R}^{SNM}_{nPrdctn}$ then describes the number of neutrons in a given neutron energy group produced by a photon in a given photon energy group, within a sphere of radius r and isotopic vector $\boldsymbol{I}$.

The response function $\boldsymbol{R}^{SNM}_{nProduction}$ operates on the current of photons entering the SNM from the shielding, and outputs the energy dependent number of neutrons produced within the SNM. To obtain the relevant tally data, the source of photons need to be able to interact with the SNM, but the SNM must be transparent to any photo-neutrons produced. This will let photo-neutrons born in the SNM transport to a tally on the SNM surface without interacting within the SNM. However, there currently does not

exist any direct way to accomplish this within MCNPX. The best approximation to this is to use an MX card to substitute, for the each isotope in the SNM, an isotope that is highly transparent to neutrons. In this work ^{27}Al was chosen, but any other highly transparent isotope can be used. With this substitution, the primary photo-neutrons produced can transport to the surface of the SNM without significantly altering the total number or energy distribution of the neutrons. Placing a F1 current tally on the surface of the sphere and tallying the neutrons crossing the SNM surface gives the best estimate for the true distribution of primary photo-neutrons produced within the SNM. Although not tried, the PTRAC card within MCNPX may be able to produce the exact quantity of interest, but requires additional post-processing of the results.

The above process is repeated for spheres of various radii $r \leq R_{max}$, where R_{max} is the maximum radius of the SNM under consideration (5 cm for this work), and for all SNM isotopic vectors, $\boldsymbol{I}$, of interest.

Primary Photo-Neutron Spatial Distribution

As was discussed previously, the spatial distribution of primary photo-neutron production is most intense on the face towards the photon beam, and dies off exponentially within the SNM as a function of depth (see figure 4.16). In addition, the primary photo-neutron production is most intense in regions under direct irradiation, as photons must be scattered into regions not directly irradiated to produce a photo-neutron there. An approximation to the primary photo-neutron production intensity is made by distributing the primary photo-neutrons produced over the region directly irradiated by the photon beam. This approximates the correct spatial locations over which the primary photo-neutrons are produced, but does not capture the intensity gradient through the SNM. Once uniformly distributed over this region, the primary photo-neutrons have

approximately the correct average "crows flight" distance to the SNM surface before they leak. Matching the average exiting chord length for primary photo-neutrons conserves the neutron interaction probability within the SNM and therefore secondary neutron production should be well approximated.

If the primary photo-neutrons were distributed arbitrarily throughout the SNM, then the average exit chord length would not be representative of reality, giving rise to errors in the secondary neutron production. For example, take a scenario where the photon beam irradiates only the very top portion of a SNM having a large radius. In this scenario, a majority of the primary photo-neutrons produced will leak since they are created very near the top surface of the SNM. If the SNM sub-model assumed that the primary photo-neutrons were produced uniformly throughout the SNM, the leakage probability will be erroneously low and the absorption probability too high. This leads to the incorrect number of secondary neutrons produced, as well as the incorrect number of total neutrons reaching the surface of the SNM.

The *SNM* response function $\boldsymbol{R}_{Escape}^{SNM}$transforms the primary photon-neutrons produced within the SNM into a distribution of neutrons (both primary and secondary) exiting the surface of the SNM. These neutrons are then assumed to be uniformly distributed over the surface of the SNM, to match the boundary conditions for the shielding sub-model developed previously for passive systems. That shielding sub-model will be used along with an updated iterative algorithm (see section 4.7.1) to transport neutrons exiting the SNM through the shield, as well as reflect neutrons back and reinterrogate the SNM.

Application of $\boldsymbol{R}_{Escape}^{SNM}$to the primary photo-neutron production from collided and uncollided photons must be handled separately, as the distributions of the neutron production within the SNM are not the same. Once the neutrons for each component are

transported to the surface, they are added together before being uniformly distributed on the surface. At this point, the neutrons produced from the interrogation are added with the neutron source from decay and spontaneous fissions which is calculated with the current capabilities within XPASS. The total neutron current exiting the SNM, $\boldsymbol{j}^{SNM}$, is then the sum of the passive and active contributions, and the transport through to the detector system is handled within the previously developed XPASS sub-models.

$$\boldsymbol{j}_{AI}^{SNM-Escape} = {}_{ACL}\boldsymbol{R}_{Escape}^{SNM}\boldsymbol{j}_{Uncollided}^{SNM-nProduction} + {}_{ACL^*}\boldsymbol{R}_{Escape}^{SNM}\boldsymbol{j}_{Collided}^{SNM-nProduction}, \quad 4.41$$

$$\boldsymbol{j}^{SNM} = \boldsymbol{j}_{AI}^{SNM-Escape} + \boldsymbol{j}_{Passive}^{SNM}. \quad 4.42$$

Response Function Generation

The response function $\boldsymbol{R}_{Escape}^{SNM}$ is generated by uniformly distributing a neutron source within a sphere over all $\xi' \leq \xi$, for a given ξ. An F1 current tally is placed on the surface of the SNM which tallies all neutrons, either primary or secondary, that reach the surface, per neutron uniformly distributed over all ξ'. The neutron source is of unit intensity and uniformly distributed within each of the neutron energy. $\boldsymbol{R}_{Escape}^{SNM}$then describes the contribution that a neutron in an energy group, uniformly distribute over all $\xi' \leq \xi$ within a sphere of radius *r* and isotopic vector $\boldsymbol{I}$, has to the number of neutrons in any other energy group which exits the surface of the SNM. The process is repeated for a range of $-\frac{\pi}{2} \leq \xi \leq \frac{\pi}{2}$, in spheres of various radii $r \leq R_{max}$, and for all isotopic vectors $\boldsymbol{I}$ of interest.

4.5.2 SNM Sub-Model Validation

Primary Photo-Neutron Production via ACL Method

The primary photo-neutron production calculated through the ACL method was validated by comparing the computed results to a direct simulation in MCNPX. Using

the calculated average chord lengths, the total primary photo-neutron production for 3 SNM types (^{235}U, ^{238}U, and ^{239}Pu) of radius 5 cm irradiated with a beam of photons was calculated for several ξ and photon source energies using the reference irradiation distribution (uniformly irradiated with a cosine weighted angular distribution). In addition, the photo-neutron production was calculated for SNM uniformly irradiated with a cos^{10} angular distribution to demonstrate the results for an irradiation scenario having a much larger ACL. The results show that matching ACLs lead to a total integrated error of a few percent at most across the SNM types, radii, and energies of interest.

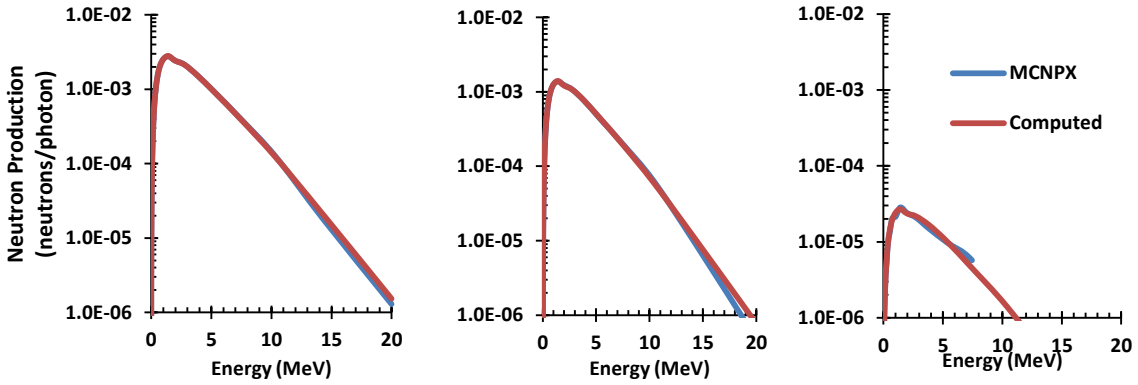

Figure 4.19: Calculated photo-neutron production from 10MeV photons in a 5cm radius sphere of ^{235}U for ξ values of $\frac{\pi}{2}$ (left), 0 (center), and -1.197 (right) radians.

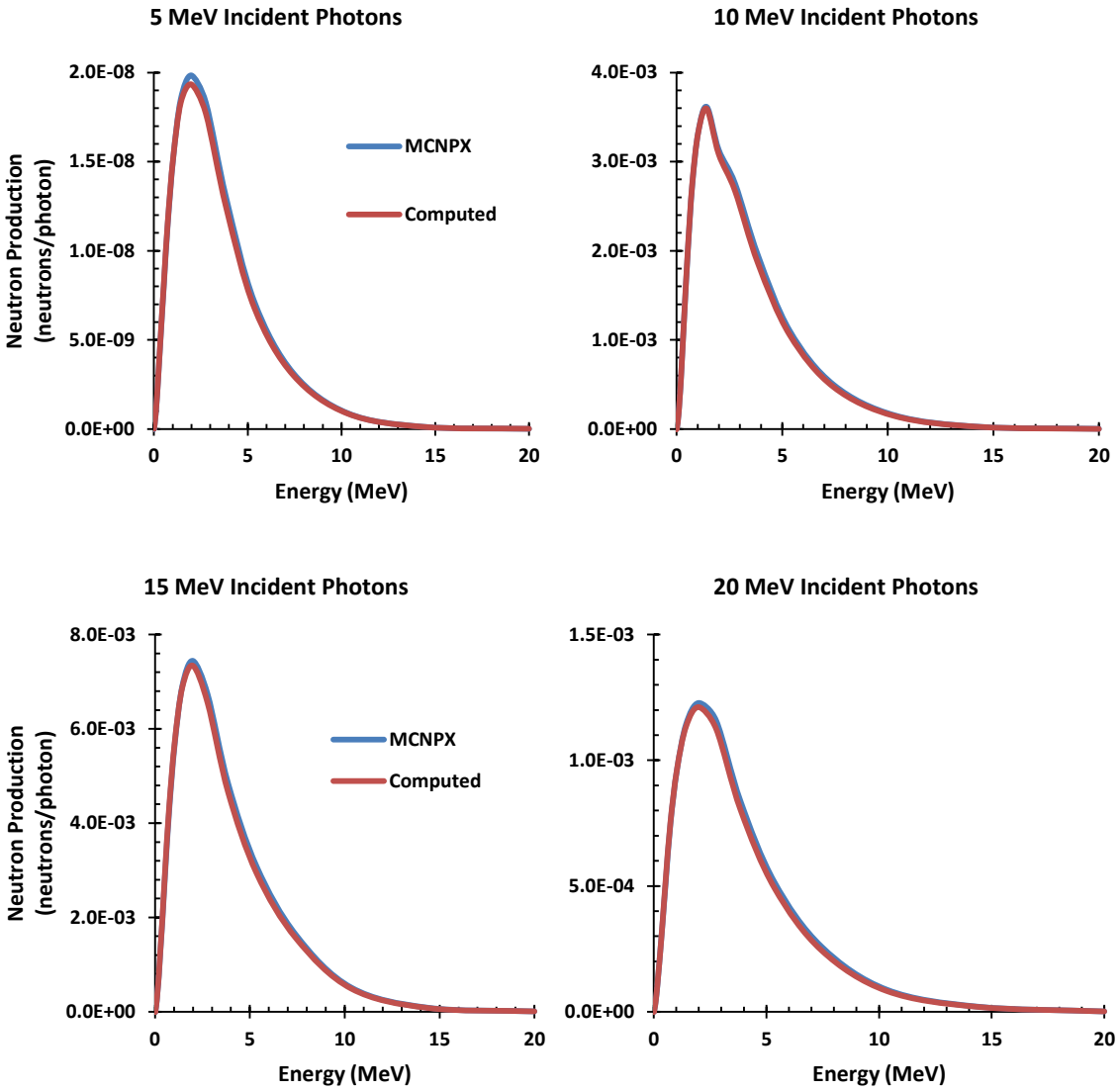

Figure 4.20: Comparison of the photo-neutron production using the ACL method to direct simulation in MCNPX for incident photons of various energies on a 5cm radius sphere of ^{235}U.

SNM Scenario Geometry				Total Neutron Production		
Isotope	Radius	Cos^n	ξ	ACL	MCNPX	Error (%)
U235	5cm	10		2.46E-02	2.48E-02	-0.81
			1.571	1.91E-01	1.91E-02	0.04
			0	9.55E-03	9.54E-03	0.10
			-1.197	1.87E-04	1.83E-04	2.14
U238	5cm	10		2.26E-02	2.29E-02	-1.33
			1.571	1.76E-02	1.76E-02	0.07
			0	8.80E-03	8.79E-03	0.11
			-1.197	1.72E-04	1.70E-04	1.16
Pu239	5cm	10		2.85E-02	2.88E-02	-1.05
			1.571	2.22E-02	2.22E-02	-0.07
			0	1.11E-02	1.11E-02	-0.12
			-1.197	2.17E-04	2.14E-04	1.38

Table 4.1: ACL Photo-Neutron Production for 10MeV Incident Photons

Total Neutron Current Exiting SNM

Highly Enriched Uranium

The first case involves calculating, with response functions, the total neutron current exiting the surface of a 1 cm sphere of HEU irradiated with 10 MeV photons, and comparing these values against direct simulation with MCNPX. The isotopic vector of the HEU is given in Table 4.2.The total photo-neutron production was first calculated as described in section 4.5.1. Figures 4.21 and 4.22 show the result of that calculation, which is then used as the current of neutrons, $\boldsymbol{j}^{SNM-nProduction}$, to which $\boldsymbol{R}_{Escape}^{SNM}$ is applied. The RMS error for the total primary photo-neutron production calculation was 0.95%, and the average error -0.45%. The errors in the primary photo-neutron production calculation are presented as a reference point for the error in the calculation of neutrons exiting the SNM.

ZAID	Weight%
92232	3.00E-08
92234	7.00E-01
92235	9.03E+01
92236	3.00E-01
92238	8.70E+00

Table 4.2: HEU Isotopic Vector

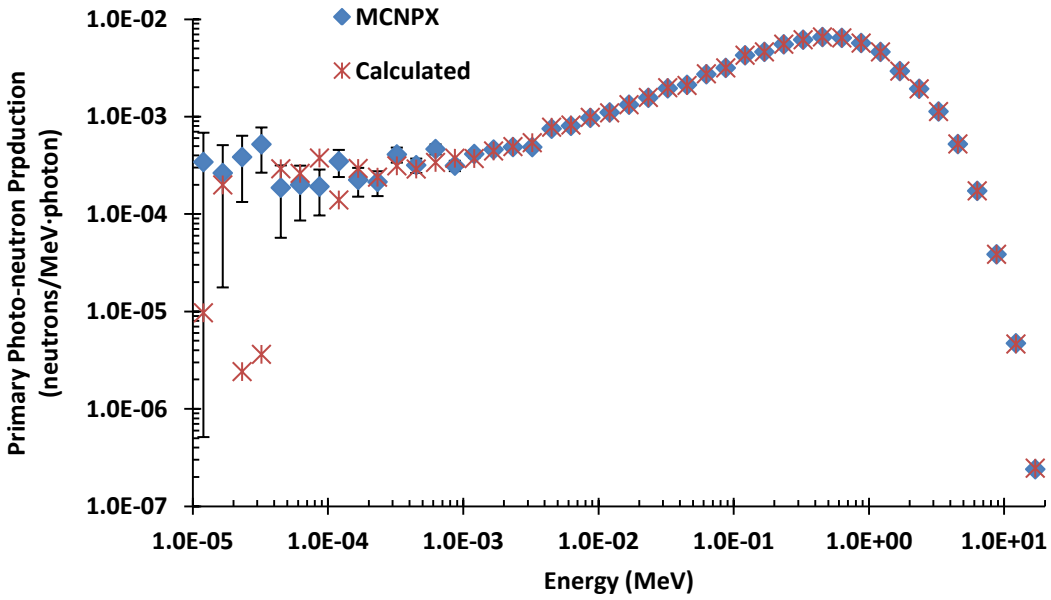

Figure 4.21: Total primary photo-neutron production for case 1.

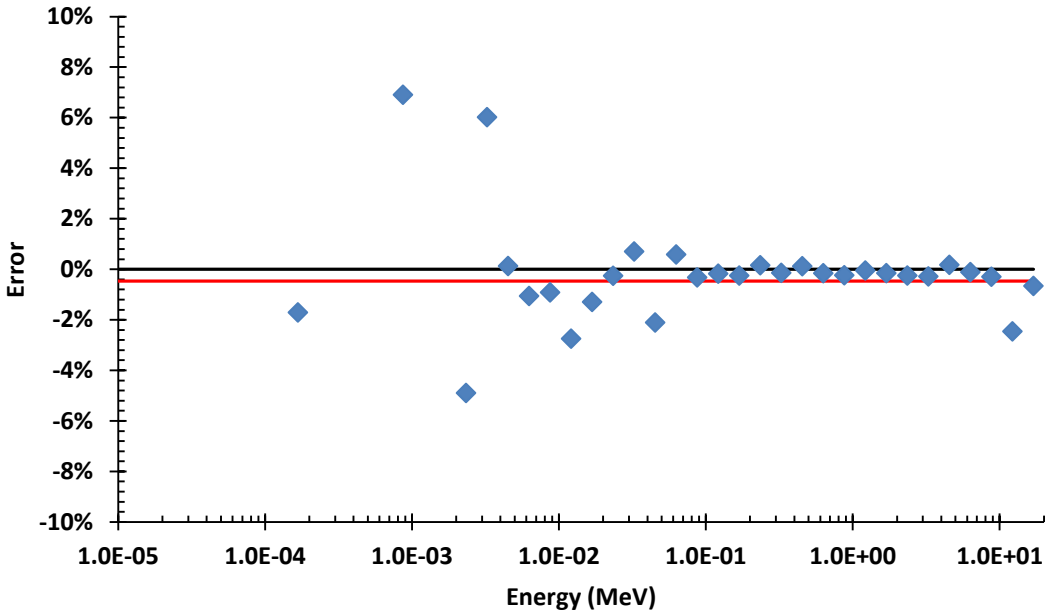

Figure 4.22: Relative errors for the primary photo-neutron production for case 1. The red line indicates the average error.

The neutron current leaking from the surface of the HEU was calculated by applying $\boldsymbol{R}_{Escape}^{SNM}$ to the calculated primary photo-neutron current given above. The energy integrated neutron current was found to be $1.42 \times 10^{-2} \frac{neutrons}{primary\ photo-neutron}$, which is a 0.22% error from the value obtained through direct simulation in MCNPX. The RMS error over all energy bins was 4.17%, with an average error of -0.19%.

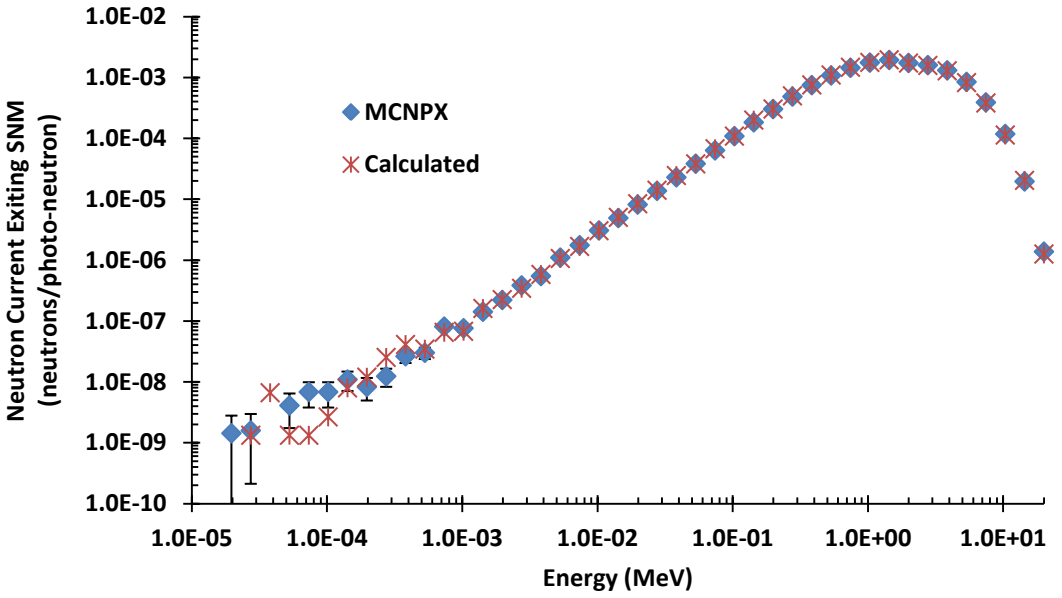

Figure 4.23: Total neutron current exiting surface of SNM in case 1.

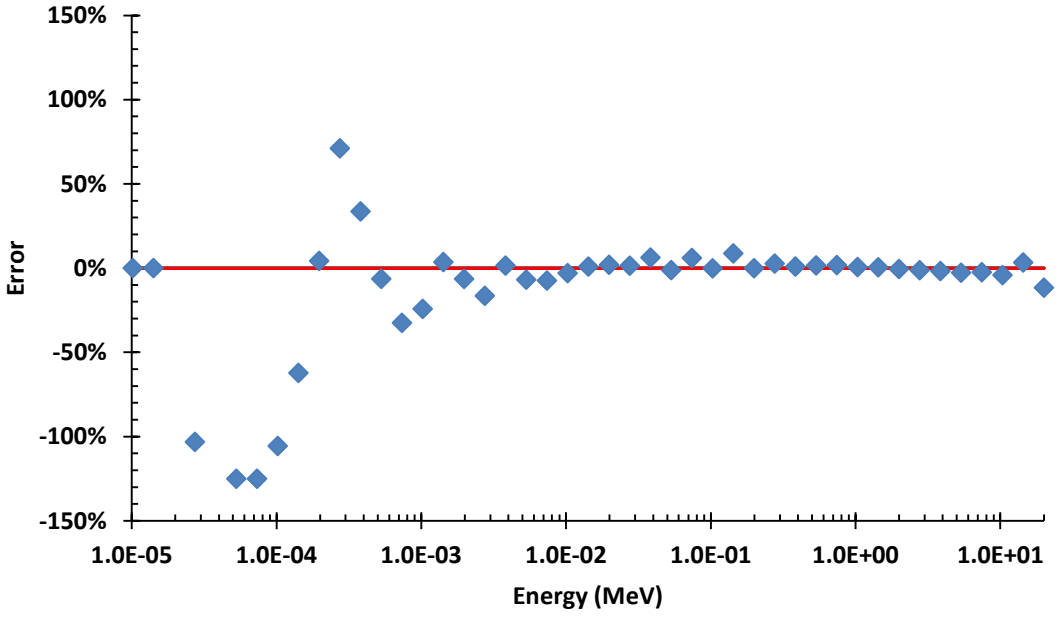

Figure 4.24: Relative errors in the neutron leakage for case 1. The red line indicates the average error over all converged energy bins.

Weapons Grade Plutonium

The second case involves calculating, with response functions, the total neutron current exiting the surface of a 1 cm sphere of WGPu irradiated with 10 MeV photons, and comparing these values against direct simulation with MCNPX. The isotopic vector of WGPu used is given in Table 4.3. Figures 4.25 and 4.26 show the primary photo-neutron production within the WGPu from 10 MeV photons. The RMS error for the total primary photo-neutron production calculation was 2.24%, and the average error-0.92%.

ZAID	Weight%
94236	5.00E-09
94238	1.50E-02
94239	9.36E+01
94240	6.00E+00
94241	3.55E-01

Table 4.3: WGPu Isotopic Vector

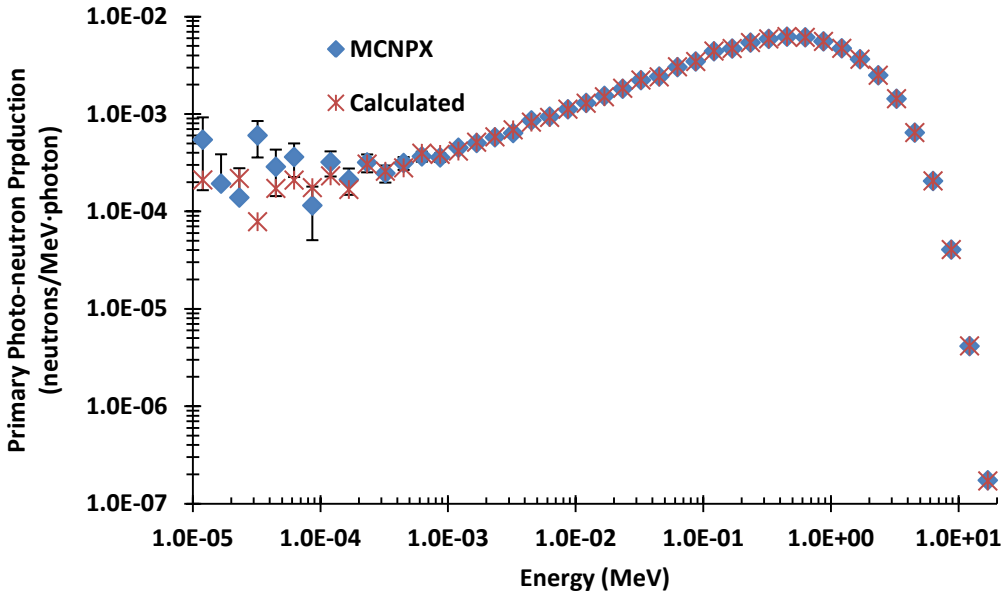

Figure 4.25: Total primary photo-neutron production for case 2.

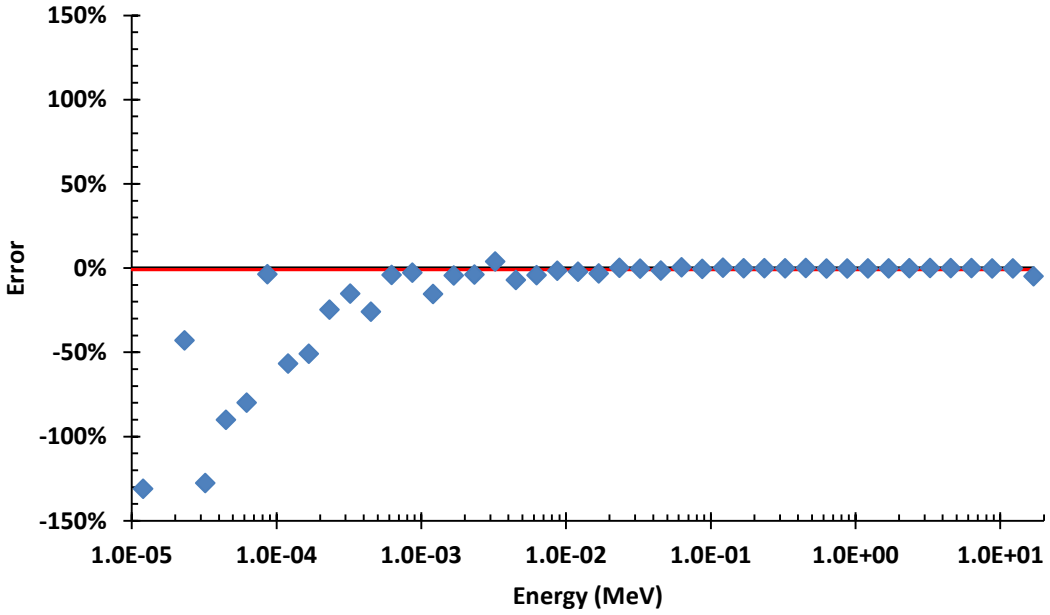

Figure 4.26: Relative errors in the primary photo-neutron production for case 2. The red line indicates the average error over all converged energy bins.

The neutron current leaking from the surface of the HEU was calculated by applying $\boldsymbol{R}_{Escape}^{SNM}$ to the calculated primary photo-neutron current given above. The energy integrated neutron current was found to be $1.64 \times 10^{-2} \frac{neutrons}{primary\ photo-neutron}$, which is a 0.31% error from the value obtained through direct simulation in MCNPX. The RMS error over all energy bins was 3.28%, with an average error of 0.26%.

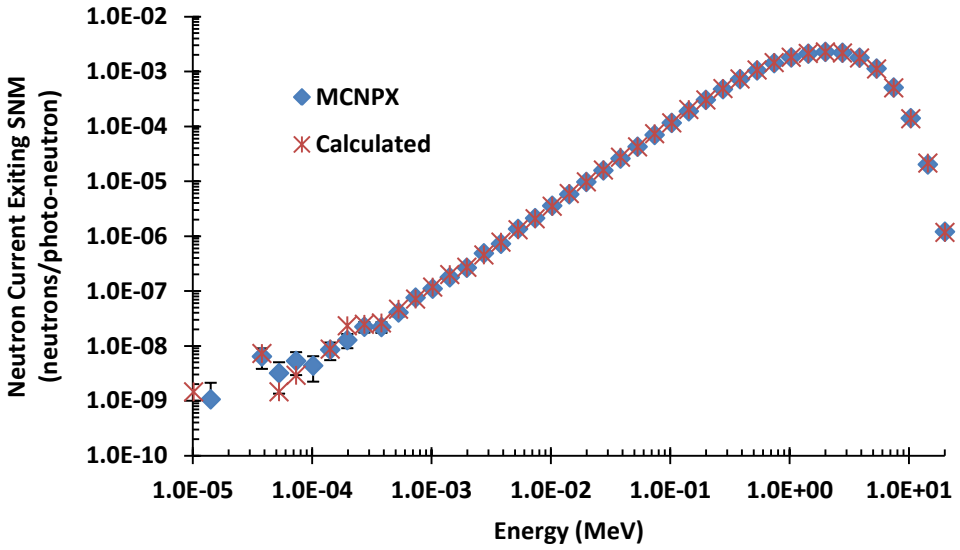

Figure 4.27: Total neutron current exiting surface of WGPu in case 2.

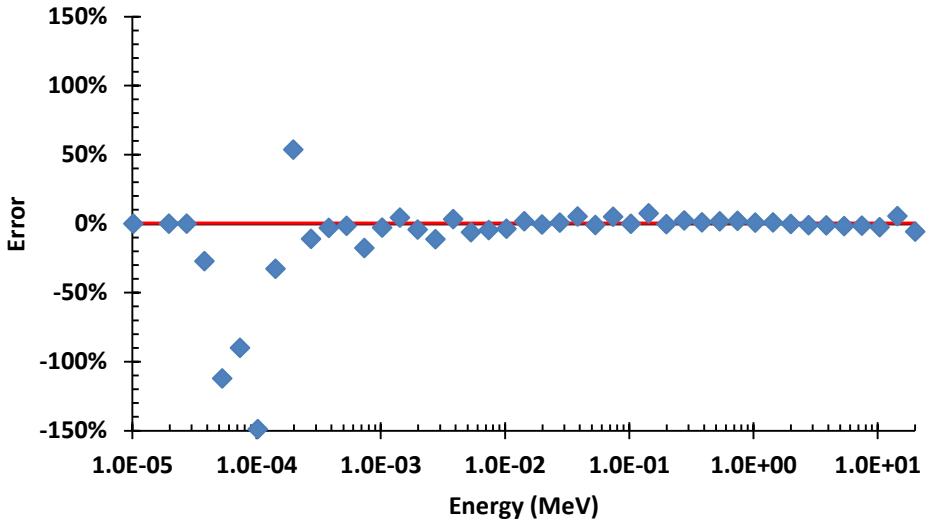

Figure 4.28: Relative errors in the neutron leakage for case 2. The red line indicates the average error.

Bounding Error Estimation

To obtain an estimate for a bounding error in the SNM sub-model, the neutron current exiting an 8 cm sphere of HEU was calculated. Since the main source of error in the SNM sub-model is the assumption of uniform birth over the irradiated portion of the SNM, a sphere of 8 cm was chosen as that assumption breaks down for SNM of large radii. HEU was chosen as a large radius (8 cm) can be attained without the geometry becoming critical. Irradiating the entire sphere $\left(\xi = \frac{\pi}{2}\right)$ exacerbates the assumption of uniform birth as the photon attenuation through the SNM is not as significant for glancing irradiations $\left(\xi \approx -\frac{\pi}{2}\right)$.

A photon source of 10 MeV was used to irradiate an 8 cm radius sphere of HEU. The total number of primary photo-neutrons produced was calculated to be $1.19 \times 10^{-1} \frac{primary\ photo-neutrons}{photon}$, which corresponds to an error of -3.41% as compared to direct simulation in MCNPX. The RMS error over each of the energy groups was calculated to be 2.16%, with an average error of -0.77%.

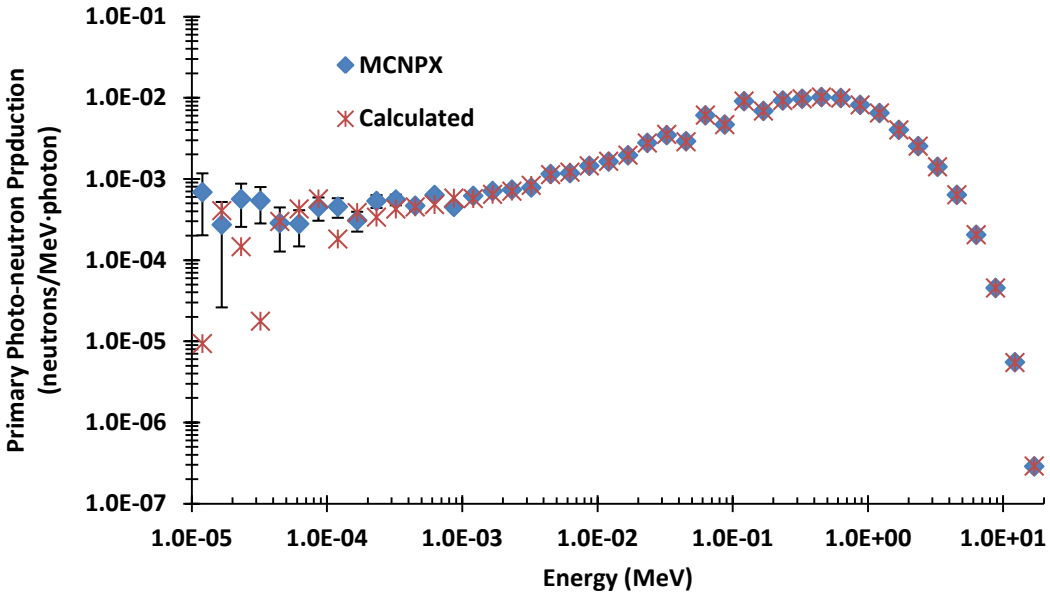

Figure 4.29: Primary photo-neutron production in the bounding case.

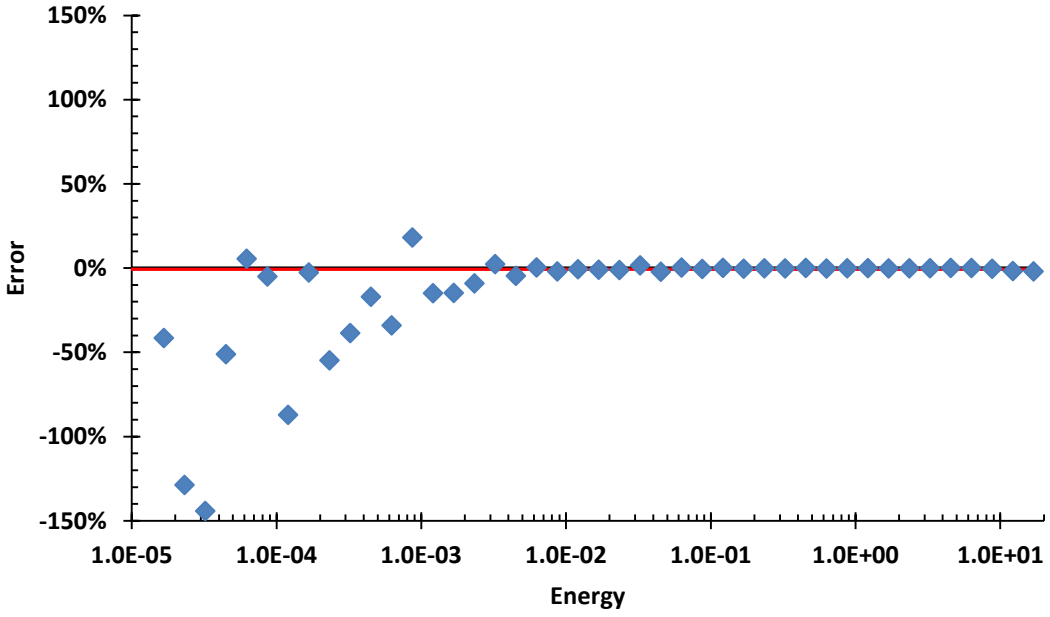

Figure 4.30: Relative errors for the bounding case. The red line indicates the average error over all converged energy bins.

Using the primary photo-neutron distributions given above, the neutron current exiting from the surface of the 8 cm radius HEU was calculated. The energy integrated current was calculated to be $8.27 \times 10^{-2} \frac{neutrons}{primary\ photo-neutron}$, which is a 47.25% error from the value obtain through direct simulation. The RMS error over all energy bins was 45.41%, with an average error of 44.9%.

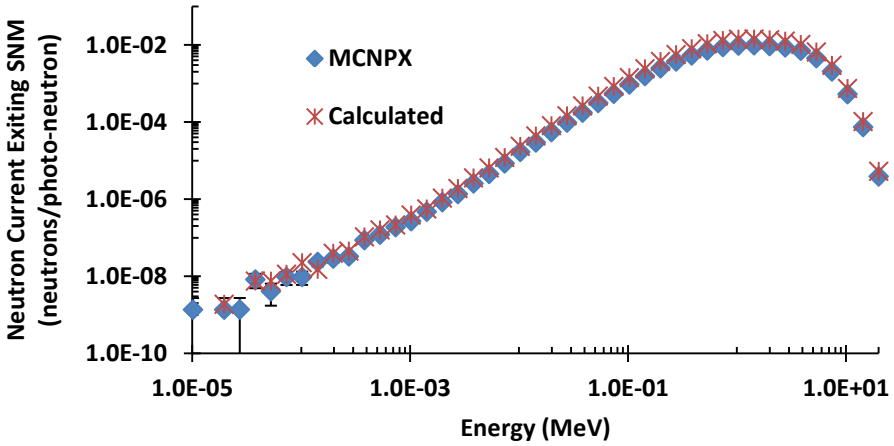

Figure 4.31: Total neutron current exiting the surface of the HEU in the bounding case.

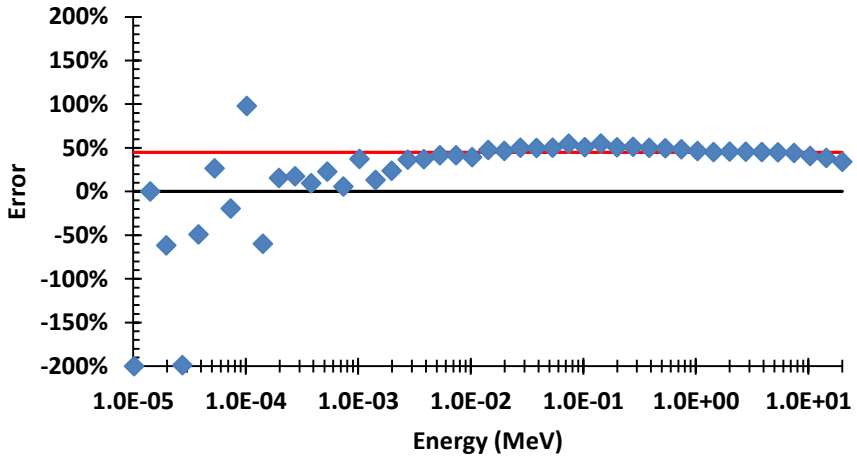

Figure 4.32: Relative errors in the neutron leakage for the bounding case. The red line indicates the average error over all converged energy bins.

4.6 INDUCED ACTIVE BACKGROUND SUB-MODEL

High energy photon interrogation of a vehicle containing bulk cargo will induce an active background signal in the detector from neutrons produced within the cargo. The response function $\boldsymbol{R}^{Bg}_{Induced}(x, mat)$ $[\frac{neutrons}{cm^3 \cdot photon}]$ describes the volumetric neutron production at a photon penetration depth x within a bulk cargo material mat per photon within the beamlet making up the beam (see section 4.3.1). Integration of $\boldsymbol{R}^{Bg}_{Induced}$ over an associated volume of the cargo will give an estimate of the total neutron production within that volume from each photon within the beamlet.

4.6.1 Induced Active Background Sub-Model Definition

To calculate the active background detector count rate from neutrons produced within the cargo, photons from the interrogation beam are first transported into the cargo. If the photon energy is above the photonuclear threshold of the cargo material, photon interaction with the cargo can lead to neutron production. The cargo is meshed into a 3D rectangular grid and a point source placed at the center of each voxel. The cargo is meshed over the volume of cargo that is irradiated at a given time, this volume is dependent upon the beam height and beam width as well as the width of the cargo (depth). Figures 4.33 and 4.34 show the meshing in 2D, for a single slice along the cargo length direction. The thickness of each voxel along the cargo length direction is equal to the width of the beam.

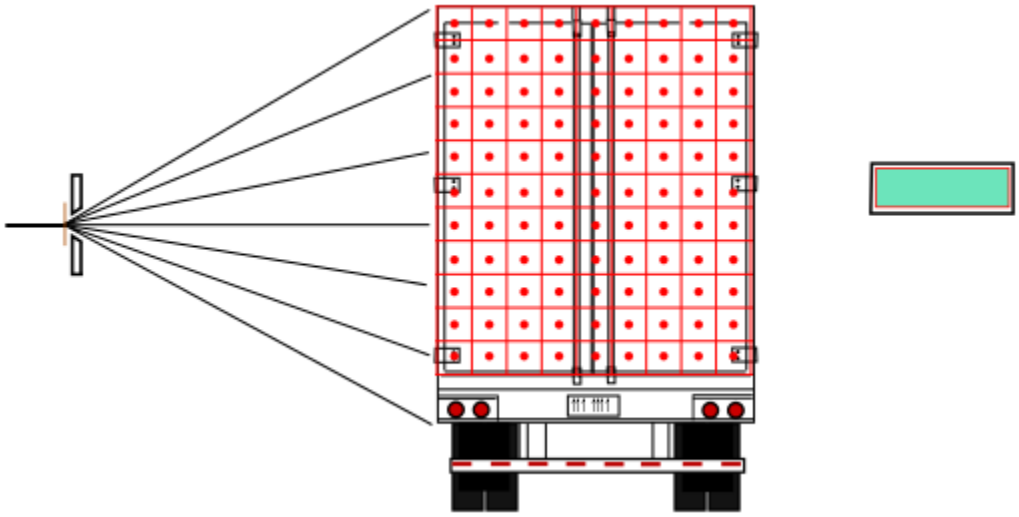

Figure 4.33: Cargo mesh in 2D for a single slice in the cargo length direction.

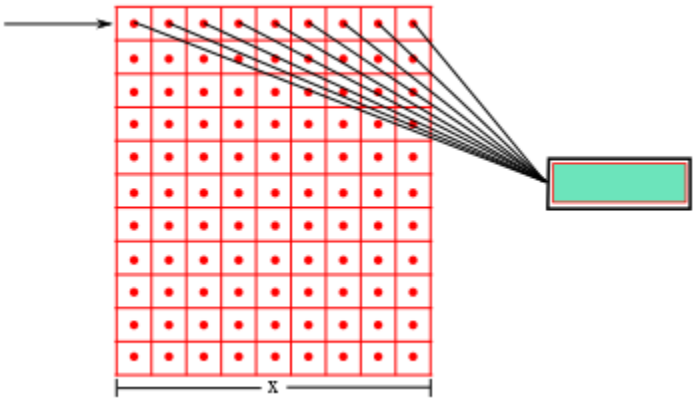

Figure 4.34: The total neutron production from each voxel is transported to the detector. Shown for a photons from a single beamlet at the top of the interrogation beam.

The response function $\boldsymbol{R}_{Induced}^{Bg}$ is used to calculate the volumetric neutron production within each voxel from photons within the beam. This volumetric neutron production is integrated over the associated voxel by multiplication by the volume of the voxel. All neutrons produced within a voxel are assumed to be generated from the point

at the center of the voxel. The response functions previously developed for XPASS are used to transport these neutrons from each point into the detector.

To obtain the total induced active background count rate, neutrons from all cargo mesh points must be transported to the detector and added together.

$$AI_{bg} = \sum_{i}^{nBH} \sum_{j}^{nBW} \sum_{k}^{nD} V_{ijk} \tag{4.43}$$

Equation 4.43 gives the formula used to calculate the induced active background count rate AI_{bg} from the summation of the background count rate from each voxel element, V_{ijk}, where nBH is the number of voxels in the beam height direction (z), nBW is the number of voxels in the beam width direction (y), and nD is the number of voxels in the cargo depth direction (x).

Response Function Generation

A geometry similar to what was developed for the cargo response functions is used to generate the response function $\boldsymbol{R}_{Induced}^{Bg}$. A beamlet, equal in dimension to the one used in the cargo sub-model, is placed on the side of the cargo and a source of photons are uniformly distributed throughout this beamlet. Spheres are placed at various depths within the cargo and aligned with the center of the beamlet, and F1 neutron current tallies are placed on the surface of each sphere. The neutron importance within the volume of cargo inside of each spherical region is set to a non-zero value (eg. 1), while the remainder of the bulk cargo has a neutron importance of zero. This is done so that only neutrons produced within each spherical volume contribute to the tally located at the surface of that sphere. The tally results for each sphere are divided by the volume of the sphere to obtain an estimate for the volumetric neutron production as a function of

depth from the vehicle surface. This process is repeated for all bulk cargo types used within the cargo sub-model.

4.7 XPASS

This section presents updates and improvements to the preexisting version of XPASS. These improvements are only applicable to the AI mode of XPASS, as there was not time to implement and ensure the changes do not have unintended side effects if implemented for the passive detection mode. For a detailed description on the use of XPASS, including the format of an input file, see reference [5].

4.7.1 Neutron Shield Sub-Model Reflection Iterations

Transporting neutrons through multiple nested layers of shielding is done iteratively to properly capture neutrons reflected back from each layer of shielding. Each shielding layer is indexed by S_i, where the outermost shielding layer is designated S_I, the innermost layer is designated as S_1, and the SNM designated S_0. The *interfaces* between each layer of shielding are indexed by i, where the interface between the SNM and first layer of shielding is $i = 0$, and the interface between the outermost layer of shielding and the cargo is designated $i = I$.

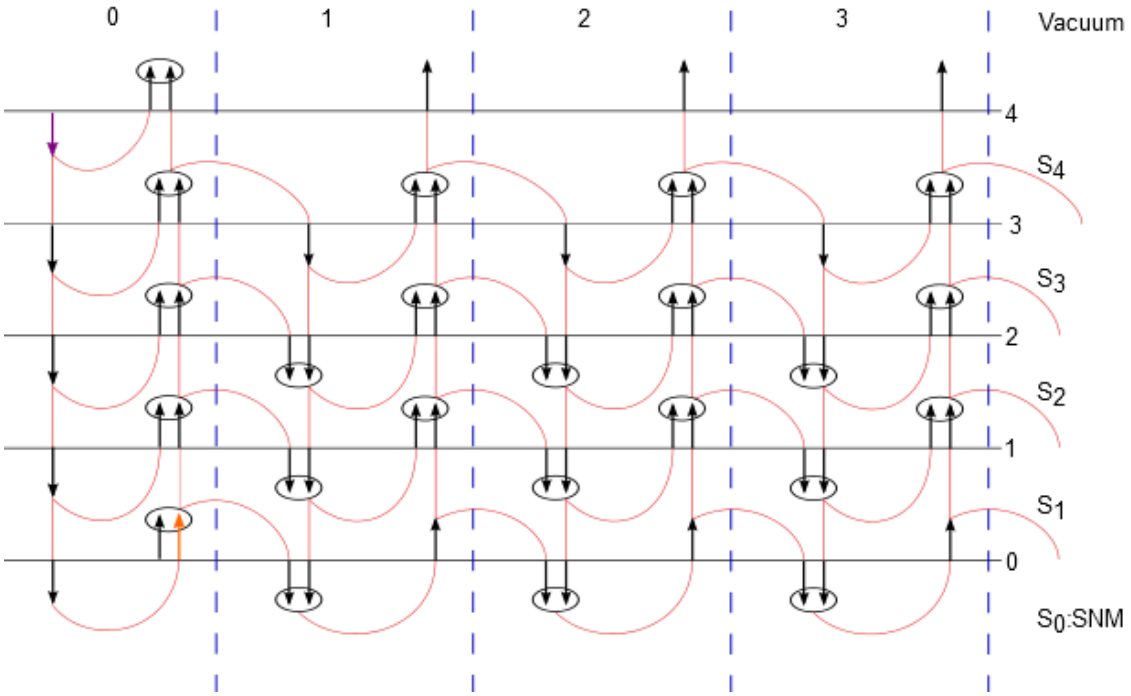

Figure 4.35: Updated neutron reflection iteration scheme.

Figure 4.35 shows a schematic of the updated reflection iteration scheme for $I = 4$. The black arrows represent the components of the inward and outward directed neutron current at each interface; the circles denote a summation of the circled components. The dashed blue lines separate the calculations done for each iteration, with the iteration number centered on the top of each section. The curved red lines show how the partial neutron currents at each interface contribute to the partial current at adjacent interfaces. The purple arrow in iteration 0 denotes neutrons entering the outmost layer shield as a boundary condition imposed on the first iteration. The orange arrow in iteration 0 denotes the passive neutron current $\boldsymbol{j}_{Passive}^{SNM}$ from spontaneous fission and decay of the SNM which is calculated using the current XPASS capabilities for passive systems.

Let the total outward directed neutron current at interface i is given by $\boldsymbol{j}_{+}^{i}$, and the total inward directed neutron current at interface i is given by $\boldsymbol{j}_{-}^{i}$. Then these partial currents $\boldsymbol{j}_{\pm}^{i}$ can be assembled through an infinite series of reflection iterations,

$$\boldsymbol{j}_{\pm}^{i} = \sum_{r=0}^{\infty} \boldsymbol{j}_{\pm}^{i,r} , \tag{4.44}$$

where $\boldsymbol{j}_{\pm}^{i,r}$ is the contribution to the total inward/outward directed neutron current at interface i from iteration r.

The elements $\boldsymbol{j}_{\pm}^{i,r}$ in equation 4.44 contain contributions from back-reflected neutrons at interface i, as well as transmitted neutrons from the immediately adjacent shielding layers. Outward directed neutrons at interface i - 1 that are transmitted through S_i as well as inward directed neutrons at interface i that are back-reflected off of S_i contribute to $\boldsymbol{j}_{+}^{i,r}$; inward directed neutrons at interface $i + 1$ that are transmitted through S_{i+1} as well as outward directed neutrons at interface i that are back-reflected off of S_{i+1} contribute to $\boldsymbol{j}_{-}^{i,r}$. The elements $\boldsymbol{j}_{\pm}^{i,r}$, are generated from the recursion relation given by

$$\boldsymbol{j}_{-}^{i,r} = {}^{-}\boldsymbol{j}_{+}^{i,r-1} + {}^{-}\boldsymbol{j}_{-}^{i+1,r} , \tag{4.45}$$

$$\boldsymbol{j}_{+}^{i,r} = {}^{+}\boldsymbol{j}_{-}^{i,r} + {}^{+}\boldsymbol{j}_{+}^{i-1,r} , \tag{4.46}$$

where for the r^{th} iteration, ${}^{+}\boldsymbol{j}_{-}^{i,r}$ denotes inward directed neutrons at interface i which were reflected outward off S_i, ${}^{+}\boldsymbol{j}_{+}^{i,r}$ denotes outward directed neutrons at interface i which were transmitted through S_{i+1}, ${}^{-}\boldsymbol{j}_{+}^{i,r}$ denotes the outward directed neutrons at interface i which were reflected inwards off S_{i+1}, and ${}^{-}\boldsymbol{j}_{-}^{i,r}$ denotes inward directed neutrons at interface i which were transmitted through S_i.

The partial currents ${}^{\pm}\boldsymbol{j}_{\pm}^{i,r}$ are obtained by applying shielding response functions to the neutron current incident onto a layer of shielding. ${}_{enter}^{exit}\boldsymbol{K}^{S_i}[unitless]$ is the response function for shielding layer S_i, where *enter* can take the value of + or - and denotes the

direction of travel (outward, inward) of the neutrons as they enter the shielding layer, relative to the center of the threat object; and *exit* can take the value of + or - and denotes the direction of travel of the neutrons as they either transmit through or reflect off the shield. Therefore, ${}^{+}_{+}\boldsymbol{K}^{S_i}$ gives the time dependent neutron energy spectrum transmitted through S_i from outward directed neutrons incident on the inner surface of S_i, ${}^{-}_{+}\boldsymbol{K}^{S_i}$ gives the time dependent neutron energy spectrum reflected back off S_i from outward directed neutrons incident on the inner surface of S_i, ${}^{-}_{-}\boldsymbol{K}^{S_i}$ gives the time dependent neutron energy spectrum transmitted through S_i from inward directed neutrons incident on the outer surface of S_i, and ${}^{+}_{-}\boldsymbol{K}^{S_i}$ gives the time dependent neutron energy spectrum reflected back off S_i from inward direct neutrons incident on the outer surface of S_i.

The four partial neutron currents needed in the recursion relations given by equations 4.45 and 4.46 can then be calculated from equations 4.46 through 4.49.

$$ {}^{+}\boldsymbol{j}^{i,r}_{-} = {}^{+}_{-}\boldsymbol{K}^{S_i}\boldsymbol{j}^{i,r}_{-} \tag{4.47} $$

$$ {}^{+}\boldsymbol{j}^{i,r}_{+} = {}^{+}_{+}\boldsymbol{K}^{S_{i+1}}\boldsymbol{j}^{i,r}_{+} \tag{4.48} $$

$$ {}^{-}\boldsymbol{J}^{i,r}_{+} = {}^{-}_{+}\boldsymbol{K}^{S_{i+1}}\boldsymbol{J}^{i,r}_{+} \tag{4.49} $$

$$ {}^{-}\boldsymbol{J}^{i,r}_{-} = {}^{-}_{-}\boldsymbol{K}^{S_i}\boldsymbol{J}^{i,r}_{-} \tag{4.50} $$

Combing equations 4.45 through 4.50, equation 4.44 can be rewritten in a form suitable for implementation with recursive iterations given by

$$ \boldsymbol{j}^{i}_{-} = \sum_{r=0}^{\infty}\boldsymbol{j}^{i,r}_{-} = \sum_{r=0}^{\infty}\left[{}^{-}_{+}\boldsymbol{K}^{S_{i+1}}\boldsymbol{j}^{i,r-1}_{+} + {}^{-}_{-}\boldsymbol{K}^{S_{i+1}}\boldsymbol{j}^{i+1,r}_{-}\right], \tag{4.51} $$

$$ \boldsymbol{j}^{i}_{+} = \sum_{r=0}^{\infty}\boldsymbol{j}^{i,r}_{+} = \sum_{r=0}^{\infty}\left[{}^{+}_{-}\boldsymbol{K}^{S_i}\boldsymbol{j}^{i,r}_{-} + {}^{+}_{+}\boldsymbol{K}^{S_i}\boldsymbol{j}^{i-1,r}_{+}\right]. \tag{4.52} $$

The initial iteration starts at interface I - 1, and the initial condition $\boldsymbol{j}^{I,0}_{-} = \boldsymbol{j}^{TO}$, where $\boldsymbol{j}^{TO} = \boldsymbol{j}^{TO}_{uncoll} + \boldsymbol{j}^{TO}_{coll}$ and is obtained from the cargo sub-model, is used to initiate

the reflection iterations. Reflections between the cargo and the threat object are current not considered. Therefore, a vacuum boundary condition is imposed at interface $i = I$. A list of all initial and boundary conditions is given in table 4.4.

Initial Condition	$\boldsymbol{j}_{-}^{I,0} = \boldsymbol{j}^{TO}$
Vacuum	$\boldsymbol{j}_{-}^{I,r} = 0\,; r \neq 0$
SNM Boundary	$\boldsymbol{j}_{+}^{0,0} = {}_{-}^{+}\boldsymbol{K}^{S_0}\boldsymbol{j}_{-}^{1,0} + \boldsymbol{j}_{Passive}^{SNM}$

Table 4.4: Reflection Iteration Initial and Boundary Conditions

The reflection iterations are repeated until a convergence criterion is met. The criteria chosen for this implementation is the total neutron current exiting the outermost shielding layer at the r^{th} iteration be much less than the total neutron current exiting outermost shielding layer from all other previous iterations; or,

$$\frac{{}^{+}\boldsymbol{J}_{+}^{I-1,r}}{\sum_{k=0}^{k=r-1} {}^{+}\boldsymbol{J}_{+}^{I-1,k}} < refeps, \qquad 4.53$$

where *refeps* is a user defined cutoff value defined in the physics block on an XPASS input file.

4.7.2 Input File Parameters Additions

Additions to the XPASS input file parameters were made to allow users access to the features developed for active interrogation. These include a new AI block, additions to the physics block, additional parameters that must be specified for AI, and slightly modified definitions of certain parameters when used for AI. The AI block as well as the new physics parameters are described in tables 4.5 - 4.8. Specification of the AI block

within the input file initiates the AI mode of XPASS; XPASS will run in passive detection mode if the AI block is excluded.

When XPASS is run in AI mode, the physics parameter *mactime* must be set to the value "on", and the parameter *interval* must be set to a value greater than zero. Active interrogation was not been implemented for a stationary vehicle, and therefore *mactime* must be set and the width of a time step must be specified with the parameter *interval*. In addition, AI was not implemented for scenarios which lack a vehicle. Therefore, the *vehicle* block must be present for vehicle type *truck* as it is the only option currently available within the XPASS data library.

In AI mode, setting the physics parameter *background* to "on" will turn on calculation of background detector count rates from natural sources (cosmic and terrestrial) only. This will not initiate an active background calculation from neutrons created within the cargo. The active background calculation as well as the option to specify a background count rate is set through the AI block. Each source of background (natural, active, user specified) is treated independently within XPASS and the total background is the sum of the three components.

The user defined time step width set through the parameter *interval* takes on a slightly different meaning when XPASS is used in AI mode. In passive mode, *interval* is simply the time step used to build the time structure for the truck traversing through the radiation portal monitor. This time structure is used to calculate the vehicle location as a function of time for transport of particles from a moving source to the detector. In AI, the value set for *interval* is still used to build the vehicle transit time structure, however the width of the time bins within that structure are not constant over all times.

To allow for measurements of the die-away signal between pulses, a very fine time structure on the order of milliseconds or less must be used. Simulation of the

vehicle transit through the interrogation system over multiple seconds in increments of roughly 1 millisecond leads to unnecessarily long computation time. A variable width time structure was used for the vehicle time structure, where a course binning over all time is set by the parameter *interval*. XPASS then calculates the time at which the SNM within the vehicle will intersect the interrogation beam, and modifies the time structure in this region. The calculation of when this intersection occurs is dependent upon the SNM size and location(s) within the cargo, vehicle velocity, source location, and the collimated width of the interrogation beam.

The time structure is modified by binning time into time bins of width $\frac{1}{freq}$, where *freq* is the pulsing frequency of the interrogation source and is specified within the AI block. This creates a single time bin for each pulse of the source. However, for each pulse there are two components, a "beam-on" time which typically lasts for several microseconds, and a "beam-off" time which fills the remainder of the time before the next pulse. This "beam-off" time is when the detector system is measuring the die-away profile of the neutron count rate. Having a single time bin for each pulse does not produce the fidelity in time required to see the die-away after the interrogation pulse has ceased. Therefore, each of the newly created time bins is then divided into *nFineTime* number of bins, where *nFineTime* is an integer value and specified within the AI block.

When specifying a neutron alarm algorithm in AI mode, the parameter *nint* should be set to a value of "1". This is because the integration over multiple time bins implemented when *nint* is set to a value greater than 1 assumes the time bins are of equal width. In AI mode, this is not the case, and the routine has not been updated to integrate over a fixed interval of time rather than a fixed number of time bins.

A final caveat for using XPASS in AI mode is the *save* block is not used. An output file for each neutron detector will always be generated.

Keyword	Req'd	Values	Description
sigmaeff	yes	≥ 0	macroscopic effective attenuation XS [cm^{-1}]

Table 4.5: XPASS Input: *physics* block addition

Keyword	Req'd	Values	Description
electrons	yes	n/a	initiates *electron* block of input
current	yes	≥ 0	electron beam current [mA]
pulsew	yes		electron pulse duration [μsec]
freq	yes		source pulse frequency [Hz]
nFineTime	yes		number of fine bins between pulses
erad	yes	> 0	electron beam radius [mm]
target	yes	[W, Pb, Al, Fe]	bremsstrahlung target material
thickness	yes	> 0	[mm]
sx	yes	[-inf,inf]	source position in x direction [cm]
sy	yes	[-inf,inf]	source position in y direction [cm]
sz	yes	> -132	source position in z direction [cm]
BW	yes	>0	collimated beam width at vehicle surface [cm]
FBH	yes	1 ≥ FBH > 0	fraction of cargo height covered by beam
bgXw	no	> 0	voxel size in x direction for induced AI background calculation [cm]
bgYw	no	> 0	voxel size in y direction for induced AI background calculation [cm]
bgZw	no	> 0	voxel size in z direction for induced AI background calculation [cm]
bg	no	n/a	initiates background block of input

Table 4.6: XPASS Input: *AI* block

Keyword	Req'd	Values	Description
[energy]	yes	> 0	unnormalized amount of electrons in energy group⁺†‡

⁺ all electrons at 8 MeV
8 1
† all electrons at 12 MeV
12 1
‡ 10% electrons at 8 MeV, 40% at 12 MeV, 50% at 18MeV
8 1
12 4
18 5

Table 4.7: XPASS Input: *electron* block

Keyword	Req'd	Values	Description
[ndet number]	yes	> 0	background count rate in given neutron detector [cps]⁺†

⁺ ndet 0: 10 cps
0 10

† ndet 0: 10 cps, ndet 1: 12 cps
0 10
1 12

Table 4.8: XPASS Input: *bg* block

4.7.3 AI Output File

When XPASS is run in AI mode, an output file will be created in the XPASS home directory. The output file is formatted to make plotting of the detector spectra, time dependent detection probabilities, and time dependent ROC curves simple. An output file is generated for each detector in the simulation. The format of the output file is described below.

The output file begins with a background section which displays the total background count rate. This total count rate is also broken down into the components user, natural, and active which correspond to the three independent components that make up the background. A blank line delimiter follows the background section.

The next line will print out the variable width time structure used in the simulation. The course regions have a time width equal to the physics parameter *interval* and the fine regions have a time width equal to $\frac{1}{freq*nFineTime}$ which are specified in the AI block. The next line will print out the time dependent detector count rate for each time bin, with background included. The data in the background section of the output file can be subtracted from this spectrum to isolate the SNM signal. A blank line delimiter follows the spectrum section.

The next section prints the detection probability (DP), for a given false alarm probability (FAP), for each time bin specified in the above spectrum section. This data is formatted as a table where the first column is reserved for displaying the FAP. Each

subsequent column gives the DP for the corresponding time bin, and each row of the table corresponds to a different FAP. Currently, the FAP is calculated in 100 logarithmically spaced values from 1E-3 to 1.0. This table is printed for each alarm algorithm specified on the neutron detector, and each table is separated by a blank line delimiter.

4.7.4 Response Function Data Library

The original method for storage of the response function data library used in the passive version of XPASS was developed without knowing the extent to which the data libraries would grow. As the response library grew, the structure of the data library quickly became unmanageable. A new response library database format was developed for the AI response function data library, with the specific goal of having an easy to manage data library that could access data extremely fast.

The previous method involved storage of the response libraries in a structure of nested directories. While this method was relatively fast for accessing data, as only several levels need to be traversed before reaching the desired data, it lead to an exponential growth in the number of directories and files used in the response library. This leads to extremely long transfer times when copying the data library to a new computer, as the IO operations on each file become the limiting factor. Transferring ~50 GB of data stored in the directory structure took about 14 hours, and had to be done overnight. In addition, there were issues where the number of files within the data library exceeded the remaining number of files the operating system (Linux) could handle. The only options were to install an additional HDD large enough to fit the data library (not possible for most laptops), or reinstall the OS and adjust the number of inodes available to the OS. These issues with the data library make XPASS not suitable for distribution,

as it is not clear if it is possible for optical medical to store the database library in this structure. In addition, the data files are stored as compressed binary files. This is disadvantageous as the data is not human readable, and there is a performance penalty as the data must be decompressed during runtime.

The response database format developed allows for storage of an entire response function within a single ASCII text file. These files are human readable, and the entire response library can be stored within a single directory in only a few files (one file for each response function). The database format follows a semi-rigid format, which makes indexing of the data possible. This indexing makes it possible to calculate the position within the file where the desired data begins. Access of the data can be done extremely fast through this indexing, even as the database file grows extremely large. Without this indexing, obtaining data in a large text file would be time consuming as each character must be read in and checked to find the appropriate data. During development, this method was tested on a database file ~15 GB in size and it took nearly 20 minutes to locate the data at the very end of the file. With the indexing scheme, the ability to calculate as opposed to search for the start of the data reduces the time to obtain the data at the end of the ~15 GB file to nearly nothing. The database format is broken into 2 sections, a header section and a response data section. The format of these sections is described below.

The header is divided into a header line, a comment block, a variables block, and a data structure block. The header line, which is the first line of the database file contains 2 integer values, *nc* and *nv*, as well as a list (*nc* values long) of variable flags given by "n" or "s". The first value, *nc*, on the header line gives the number of lines of comments present within the comment block. The second value of the header line, *nv*, gives the number of variables, besides source energy, over which the response function spans;

energy is not included as the response function data always spans source and destination energies without exception. For example, if the AI source sub-model spans electron energy, electron beam radius, target material, target thickness, and beam divergence angle, the value of *nv* would be 4 (electron energy is excluded). Finally, the header line ends with a list of flags, either "n" or "s", one for each variable (so *nv* flags) which describe how the values in the variable block should be interpreted. If a flag is set as "n", then the variable values will be treated as numeric values, and if the flag is set as "s", the variable values will be treated as strings. Treating values as a string is required for variables such as target material which do not take numerical values. However, if all data was treated as simple text, then when XPASS needs data for the value 2.65, it will not find a match if the data happens to be stored under as 2.650. Using the "n" flag tell the database parser that the particular variable is a numerical value, and to treat the text entry 2.650 as the numeric value 2.65. A newline character terminates the header line.

The next section within the database file is the comment block. The comment block must be *nc* lines long, and can take any form. The size of the comment block (in numbers of lines) can always be adjusted by modifying the value of *nc*.

The variable block follows the comment block. The variable block is *nv* lines long, with each line containing a whitespace delimited list of the data point values present within the response data for the corresponding variable. For example, if the target material variable of the AI source sub-model spans W, Pb, Al, and Fe, then the line which corresponds to the target material variable would read,

```
W Pb Al Fe
```

where the order of values match the order at which they appear within the data block (in this example, W would appear before Pb and so forth). The order in which the variables appear within the variable block indicated the order in which they are present within the

data block. For example, if the AI source sub-model only spanned target material and target thickness, then the variable block

```
W Pb Al Fe
0.5 1.0 1.5 2.0 2.5
```

indicates that the data for all target thicknesses (0.5-2.5 mm) of W will appear first, then the data for all target thickness of Pb, and so forth. The variable block

```
0.5 1.0 1.5 2.0 2.5
W Pb Al Fe
```

indicates that the data for all target materials (W, Pb, Al, Fe) for target thickness 0.5 mm will appear first, then the data for all target materials for target thickness 1.0 mm, and so forth. See the end of this section for a detailed discussion on the indexing of the data within the response data block. The flags on the header line tell how to interpret the values for each of the respective variables in the variable block. For example, the header line (with 10 lines of comments) for the variable block

```
W Pb Al Fe
0.5 1.0 1.5 2.0 2.5
```

would be

```
10 2 s n
```

and the header line for the variable block

```
0.5 1.0 1.5 2.0 2.5
W Pb Al Fe
```

would be

```
10 2 n s
```

After the variable block, the energy and time binning structures are defined in the data structure block. The data structure block beings with a single line with three integer values, *nSE*, *nDE*, and *nTme*, which tell how many bins are present within the source

energy, destination energy, and time binning structures respectively. The next two lines give the source and destination upper energy bin values; and if $nTme > 0$, a third line is present which gives the upper time bin values. After the group structures, a blank line terminates the header section and initiates the start of the response data section.

The response data section begins after the blank line delimiter separating it from the header section. The response data section stores the response function matrix values as well as the relative errors of each matrix entry. Each matrix beings with a data description line, which lists the values for each of the variables for which the particular response matrix applies. The format of the data within the response data section, as well as the method for indexing of the data is given below.

The response function data are stored as a table which represents the matrix that the data will be placed into. If each matrix element is stored in scientific notation to a precision of d, and the relative error is stored in fixed point notation to a precision e, then each matrix entry will take up $c = d + e + 10$ characters, including white space, on a single line. For example, if $p = 4$ and $e = 4$, the value $32.4 \pm 3\%$ would be stored as "3.2400E+01 0.0030 " which includes the trailing whitespace after the relative error value. Each row within the data matrix represents an energy bin within the destination group structure, and each column represents an energy bin within the source energy group structure. Therefore, a single line in the matrix will have $c*nSE + 1$ characters, including the newline character, and the entire matrix will have $M = (c*nSE + 1)*nDE$ characters. If the response function is time dependent, then matrices for each time bin appear in sequence, so the total number of characters within a time dependent response function is $M = (c*nSE + 1)nDE*nTme$. To simplify the indexing scheme, the data description line is padded with white space to $c*nSE + 1$ characters (including the newline character) to match the line width of the data. Therefore, the total number of

characters associated with a response function, including the data and the data description, is given by

$$M = (c \cdot nSE + 1)(nDE + 1)\ ;\ nTme = 0$$
$$M = (c \cdot nSE + 1)(nDE \cdot nTime + 1);\ nTme > 0 \qquad 4.54$$

An indexing scheme was developed to quickly calculate which response function within the response data section hold the desired data. Before this method is described, the order of the response data within the data section will be illustrated with an example. If the AI source sub-model spans 3 variables, target material, target thickness, and beam divergence angle, and the phase spaced encompassed by those variables is coarsely sampled, then the variable block of the database file may be given as below,

```
W Al Pb
0.5 1.0 1.5
2 5
```

where the target thickness is given in millimeters and the divergence angle is degrees. With a variable block orders as shown above, the order in which the response data will appear within the response data section is

```
(W,0.5,2),(W,0.5,5); (W,1.0,2),(W,1.0,5); (W,1.5,2),(W,1.5,5);
(Al,0.5,2),(Al,0.5,5); (Al,1.0,2),(Al,1.0,5); (Al,1.5,2),(Al,1.5,5);
(Pb,0.5,2),(Pb,0.5,5); (Pb,1.0,2),(Pb,1.0,5); (Pb,1.5,2),(Pb,1.5,5).
```

Therefore, if the data for (Pb,0.5,5) is desired, the data from the 13th response function must be used, where the first response function (W,0.5,2) is considered the 0th response function.

If the response function spans nv variables, indexed from [1,nv], and the v^{th} variable contains N_v samples of the possible variable values, indexed from [0,N_v - 1], and $\vec{v}$ is a nv element vector which has the index of the desired data for each variable (eg. $\vec{n} = (2,0,1)$ for (Pb,0.5,5)), then the desired data can be found in the R^{th} response function, where

$$R = \left(\sum_{v=1}^{nv-1} n_v \cdot \prod_{i=v+1}^{nv} N_i \right) + n_{nv} \, . \qquad 4.55$$

Using equation 4.55 with $nv = 3$, $\vec{n} = (2,0,1)$, $N_1 = 3$, $N_2 = 3$, and $N_3 = 2$, the value of R is calculated to be $R = 2 \cdot (3 \cdot 2) + 0 \cdot (2) + 1 = 13$ which matches previous value given for *R*.

To index the R^{th} response function, the location of the first character where the data beings must be calculated. Knowing the total number of characters associated with a response function *M*, the character relative to the start of the *response data section* where the desired response function data begins is given by *R*M*. To obtain the location relative to the start of the database file, the total number of characters hc in the header section, including newline characters as well as the blank line delimiter between the header and data sections, is added to *R*M*. The value of hc must be determined by counting each character within the header block when the database file is opened, as there are no restrictions on the number of characters within the various sections of the header block. Written out explicitly, the location of the character, relative to the beginning of the database file, where the desired data described by $\vec{n}$ begins, is given by

$$R = \left[\left(\sum_{v=1}^{nv-1} n_v \cdot \prod_{i=v+1}^{nv} N_i \right) + n_{nv} \right] (c \cdot nSE + 1)(nDE + 1) + hc; nTme = 0 \, ,$$

$$R = \left[\left(\sum_{v=1}^{nv-1} n_v \cdot \prod_{i=v+1}^{nv} N_i \right) + n_{nv} \right] (c \cdot nSE + 1)(nDE \cdot nTme + 1) + hc; nTme > 0 \, . \qquad 4.56$$

Chapter 5

RESULTS

This chapter presents benchmark results from the fully integrated model incorporating all AI sub-models as well as the sub-models developed previously for passive detection systems. Following the benchmarks, several applications of the use of XPASS to simulate realistic deployment conditions for AI technologies are presented. These application case studies inform detection methodologies by shedding light on the sensitivities of the detector count rate to changes in the scenarios. Appendix D contains examples of the XPASS input files used to generate the simulation data in this chapter.

5.1 BENCHMARKS

A comparison of published results to those given by XPASS simulations are given below. Given the nature of AI systems involving nuclear material, there are few publicly available experimental results. Those that are available are typically carried out in very controlled environments, and do not model a vehicle traversing through an interrogation source and detector system, but rather contain a stationary mass of SNM that is irradiated with a single pulse of photons. Due to the inability to completely replicate the published experimental setups, we do not expect to obtain simulated results that match experimental values exactly. Rather, we expect results to be within an order of magnitude, but exhibit the same behaviors and sensitivities to changes.

5.1.1 Case 1: Single pulse of 10 MeV photons on 5.3 kg of HEU, 2.8 kg of WGPu

XPASS was used to simulate an experiment conducted jointly by Idaho National Laboratory (INL) and LANL [35][36]. In the experiment, the neutron signal from irradiating a 5.3 kg sphere of bare HEU was obtained by measuring the neutron count rate

for 8 ms after a pulse of 10 MeV (maximum energy) photons irradiated the HEU. This procedure was repeated many times and the data aggregated to obtain the expected neutron count rate from a single pulse. The pulse frequency was given to be 125 Hz, and the pulse width given to be 4 μs with a electron beam current of 6 mA. The HEU was placed 100 cm from the linear accelerator and rows of 6 He-3 detectors were placed on either side of the HEU at a distance of 50 cm perpendicular to the beam axis. Each detector was 117 cm long, 2.54 cm in diameter, and pressurized to 10 atm. Each He-3 tube was surrounded with polyethylene moderator, and was wrapped with a layer of cadmium to reduce background counts.

The above experimental setup was replicated as closely as possible within XPASS. However, due to limitations within the current response library, several important factors could not be correctly matched. Currently, the detectors may only lie on a plane at a fixed distance from the wall of the cargo container; this distance corresponds to 198.1 cm from the cargo center. To replicate the 50 cm distance between the SNM and detector, the SNM is moved as close to the detector as possible within XPASS. However, as XPASS was developed for vehicle transport of SNM, the current response functions library is limited to SNM locations within the volume of a $259.08\ \text{cm} \times 259.08\ \text{cm} \times 1615.44\ \text{cm}$ trailer. Therefore, the closest SNM to detector distance that can be achieved with the limitations is 78 cm. This is achieved by placing the SNM adjacent to the cargo container wall which is closest to the detector. The interrogation source is not limited in its placement and can be moved to any location, so the 100 cm source to SNM distance can be achieved.

Significant differences are present between the detectors used within the INL work and those modeled within XPASS. The INL detectors have a layer of cadmium shielding embedded within a layer of 25% boron loaded flexible shielding. The entire

detector is encased in moderator that is used to thermalize cosmic neutrons which then become absorbed within the shielding. While the intent is to reduce the cosmic background, the shielding will also play affect the measured signal from the SNM. This shielding is lacking in the XPASS model and therefore a higher (possibly significantly) neutron count rate is expected from an XPASS simulation. In addition, the He-3 tube used in the experiment was 2.54 cm in diameter and pressurized to 10 atm, whereas the He-3 detector model within XPASS is fixed at 4.99 cm diameter and a pressure of 6 atm. The polyethylene moderator that surrounds the He-3 tube in the experiment can be modeled within XPASS. However, the thickness of this moderator is not given and therefore differences in the true versus simulated moderator thicknesses will lead to differences in the neutron count rate. In addition, the XPASS detector contains a Fe reflector not present in the experimental design. Figure 5.1 shows a comparison between the geometry of the detector design used in the experiment and those modeled within XPASS, while figure 5.2 shows a comparison between the experimental setup geometry and that modeled within XPASS. Table 5.1 lists the relevant experimental parameters values and those used in the XPASS simulation.

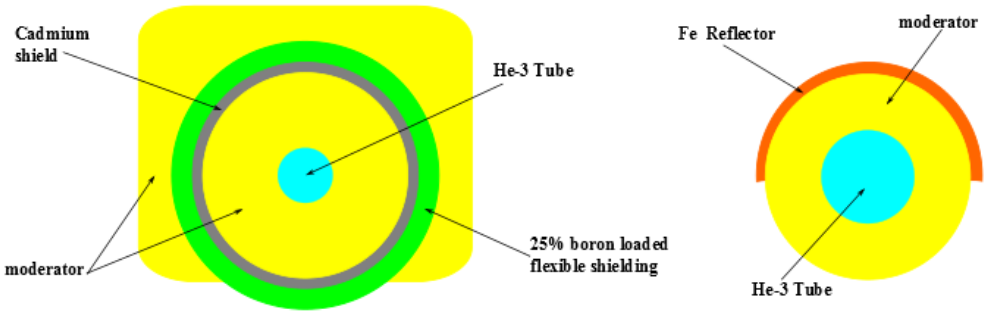

Figure 5.1: Comparison of the detector used in the INL work (left) and the detector simulated within XPASS.

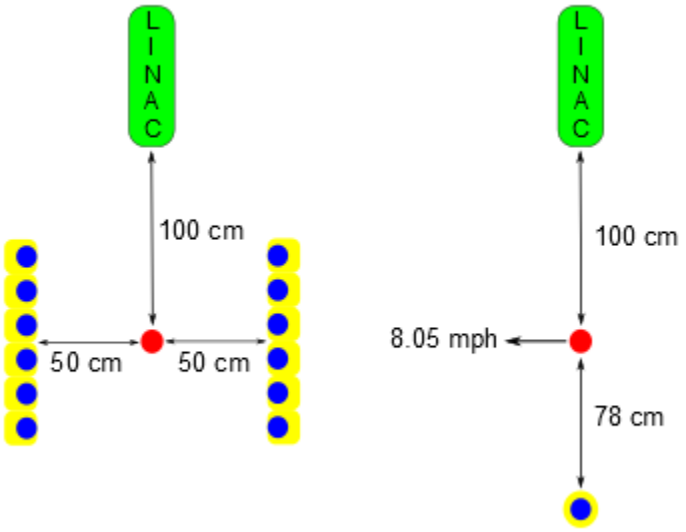

Figure 5.2: Comparison of the experimental and simulated geometries for benchmark case 1. *Left*: Actual setup. *Right*: XPASS setup.

	Experiment	XPASS
Al Source		
current	6 mA	6 mA
pulse width	4 μs	4 μs
frequency	single pulse	single pulse
distance to SNM	100 cm	100 cm
SNM		
mass	5.3 kg	5.3 kg
shielding	bare	bare
distance to detector	50 cm	78 cm
Detector		
length	117 cm	117 cm
diameter	2.54 cm	4.99 cm
pressure	10 atm	6 atm
shielding	cadmium	none
moderator	yes	yes
efficiency	unknown	100%

Table 5.1: Comparison of relevant experimental and simulated parameters for benchmark case 1.

XPASS models the AI source as a continuously pulsing electron beam hitting a bremsstrahlung target to produce photons. In order to replicate the signal from a single pulse of the linear accelerator, the pulse frequency was reduced from 125 Hz to 5 Hz. This pulse rate was chosen to be a low enough value so that only a single pulse will hit the SNM. This allows XPASS to effectively simulate the die-away from single, isolated pulse in time. To reduce computation time as well as get around the limitations XPASS has on the placement of the detector, the signal from a single detector was simulated and the results scaled by a factor of 12 to obtain an estimate for the neutron count rate from a set of 12 detectors.

In the XPASS simulation, the HEU is placed within a vehicle carrying no bulk cargo, which was traveling through the interrogation system at 8.05 mph. Figure 5.3 shows the detector count rate for the first 8 milliseconds after the interrogation pulse. XPASS was not used to calculate an active background for this benchmark. Instead, a constant background count rate of 0.167 cps was specified within the XPASS input file. This value was obtained from plots of the active background count rate in the INL work.

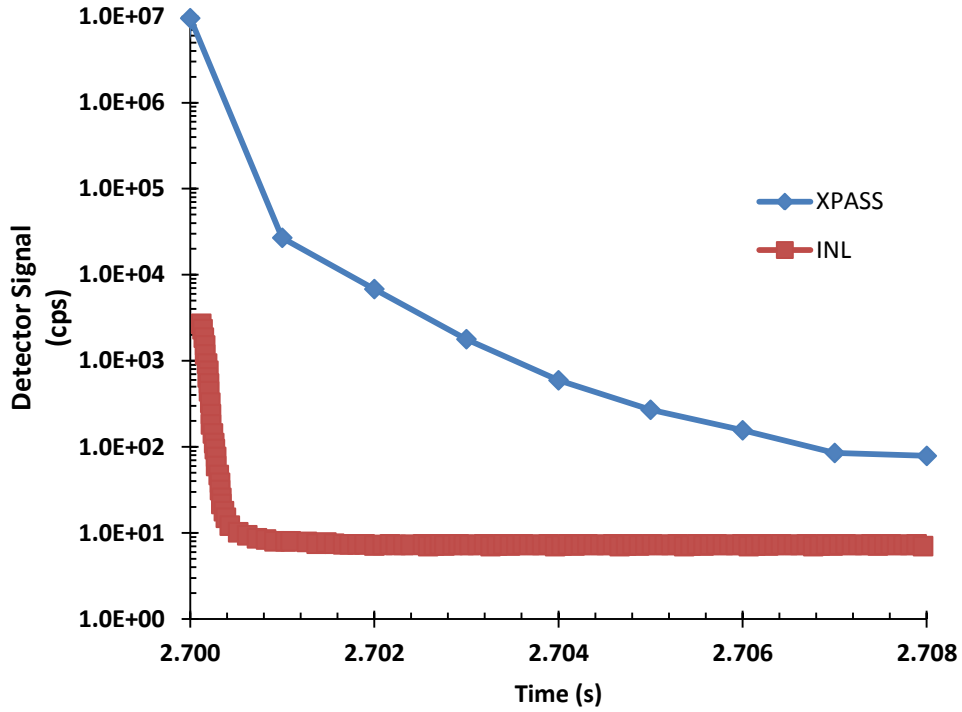

Figure 5.3: Detector signal for the first 8 ms after a pulse of 10 MeV photons on 5.3 kg of HEU.

The results obtained from the XPASS simulation show the detector count rate falling to a value of 84.7 cps at 8 ms after the pulse. This result is a factor of 12.1 times higher than the experimental value of ~7 cps. The die away rate of the detector signal immediately after the pulse also is not in agreement with the experimental data. The experimental results show a rapid fall-off in the detector count rate to ~7 cps in about 0.5 ms, while the die-away in the XPASS results continues even after the prompt neutron transient has ended. The longer die away time in the XPASS results is likely caused by neutrons thermalizing in the (possibly larger) moderator, reaching the reflector, and making their way back to the detector. In the experiment, the shielding will absorb any neutrons that migrate far from the detector, thermalize, and make their way back towards

the detector. The only thermal neutrons that reach the detector are those that thermalize within the moderator immediately surrounding He-3 tube. The presence of shielding is expected to lead to a lower detector count rate that falls off rapidly as compared to the XPASS detector geometry.

Direct comparison of the magnitude and die away times between the experimental results and the XPASS simulation are not meaningful as there are significant differences in the setup configurations and detector geometries. The lack of shielding and the presence of a reflector in the XPASS detector can explain the differences in the die away times. Those same differences as well differing He-3 tube radii, moderator thicknesses, and SNM to detector distance can explain the differences in the magnitude of the detector count rate. Since XPASS cannot be used to reproduce this experimental setup, the sensitivity to the change in a parameter is investigated to determine if XPASS produces correct behavior.

Isolation of the active contribution to the detector count rate is desired in order to benchmark the AI capability of XPASS. This will ensure that any differences seen are not due to errors caused by differences in the passive spectra. The INL work gives the detector count rate for both active and passive scenarios, where the active count rate includes the passive the contribution from the passive signal. The passive count rate was subtracted from the active count rate to obtain the neutron count rate from neutrons born from interrogation of the SNM only. The XPASS source code was modified so that the passive neutrons from decay and spontaneous fissions of the SNM were not included in the detector spectra.

As stated previously, direct comparison between the XPASS and INL results is not meaningful do to the significant differences. However, comparisons between the change in results caused by a change in parameters will determine if XPASS produces the

correct behavior. The XPASS results (modified source code) were normalized so that the detector count rate at 8 ms after the pulse hits the HEU matched that given in the INL results. This renormalization factor was found to be 1.051. Using this renormalization factor obtained from the simulation of 5.3 kg of HEU, a second case was simulated with 2.8 kg of WGPu. Figure 5.4 shows the detector count rate for the 5.3 kg HEU and the 2.8 kg WGPu cases.

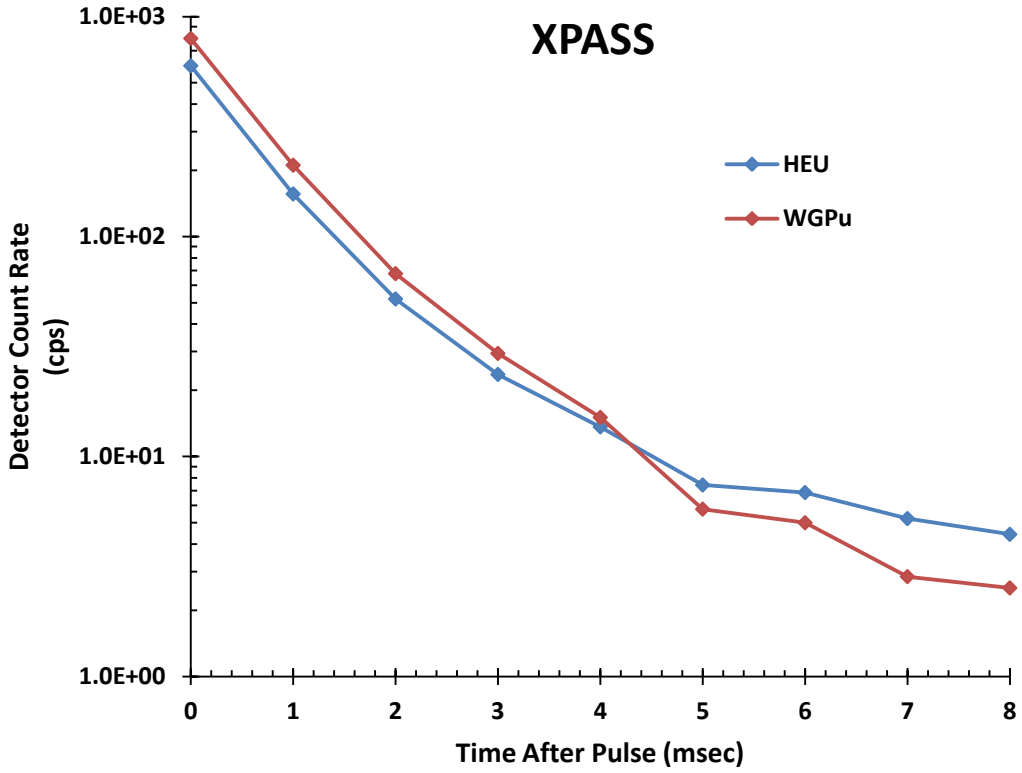

Figure 5.4: Detector signal for the first 8 ms after a pulse of 10 MeV photons on 5.3 kg of HEU and 2.8 kg of WGPu.

Figure 5.4 shows the detector count rate initially being higher for the WGPu, then switching to HEU at around 4.5 ms after the pulse. The ratio between the detector count rates is taken at 8 ms after the pulse and compared to the same ratio from the INL work.

At 8 ms after the pulse in the XPASS simulation, the HEU case has a detector count rate of 4.43 cps and the WGPu case has a detector count rate of 2.53 cps. This results in a value of 1.75 for the relative count rate between the HEU and WGPu cases. The ratio calculated from the INL work (passive signal subtracted) was found to be 2.09. Figure 5.5 gives a side by side comparison between the results simulated with XPASS, and those given in the INL work.

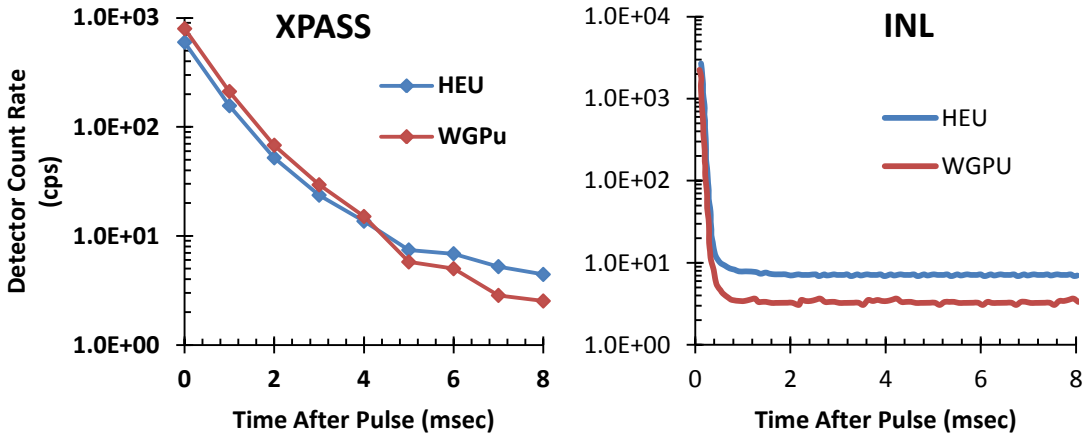

Figure 5.5: Comparison between the XPASS and INL results.

The differences in the results may be due to several factors. First, applying a single normalization factor to scale the results over all energies may not be correct. Differences in the neutron energy distributions exiting the HEU versus WGPu can lead to differing levels of thermalization within the moderator. Without shielding, the thermalized neutrons can easily reach the detector and lead to different relative count rates, and a energy dependent scaling factor may be more appropriate. In addition, inspection of the XPASS results show the solution is not quite converges as there is not a smooth decrease during the die away period. If the results past 8 ms are looked at, several time steps see an increased detector count rate relative to the previous time step.

This is due to the response functions data within $R_{nLeakage}^{SNM}$ not being well converged over all energies at every time step. Converging a tally binned in energy and time, where the major factor in the time dependence is the emission of delayed particles, is extremely challenging within MCNPX. Improving the statistical convergence of the data within $R_{nLeakage}^{SNM}$ should lead to improved results. Taking these differences into account, the general behavior of the XPASS results matches that in the INL work within reason.

5.1.2 Case 2: Single pulse of 10 MeV photons on 22 kg of HEU

XPASS was used to simulate an experiment conducted by LANL where a 22 kg sphere of bare HEU was irradiated by a single linear accelerator pulse producing 10 MeV (maximum energy) photons [31][37][38]. The detector signal was obtained from measurement of the neutron count rate for 20 ms after each pulse. This procedure was repeated many times and the data aggregated to obtain the expected neutron count rate from a single pulse. The pulse frequency of the linear accelerator was 50 Hz, and the pulse width 6 μs. The electron beam current was not given directly, but the measured dose rate at 1 m was given as 160 R/min, and a MCNPX calculated normalization factor of 150 R per 4×10^{15} electrons at 1 m was provided. Using this information, the electron beam current was found to be 38mA. The HEU was placed at 7 m from the linear accelerator and a large area detector (LAD) containing 4 He-3 tubes was placed at a distance of 1.5 m directly behind the HEU (within the beam path). Each He-3 tube within the LAD was 182.88 cm long, 5.08 cm in diameter, and pressurized to 2 atm. The space between He-3 tubes within the LAD was filled with polyethylene moderator to increase detection efficiency. Additionally, the LAD was completely surrounded in a layer of cadmium to reduce background counts.

The above experimental setup was replicated as closely as possible within XPASS. Several of the limitations present in benchmark case 1 also affect benchmark case 2, but overall the parameters of benchmark case 2 were able to be replicated much more closely within XPASS than those of benchmark case 1. Table 5.2 gives a comparison of the relevant experimental parameters and the values used for the simulation within XPASS.

	Experiment	XPASS
Al Source		
current	38 mA	38 mA
pulse width	6 μs	6 μs
frequency	single pulse	single pulse
distance to SNM	700 cm	700 cm
SNM		
mass	22 kg	22 kg
shielding	bare	bare
distance to detector	150 cm	150 cm
Detector		
length	182.88 cm	182.88 cm
diameter	5.08 cm	4.99 cm
pressure	2 atm	6 atm
shielding	cadmium	none
moderator	yes	yes
efficiency	27%	*27%

*Simulated at 100% efficiency then multiplied by 0.27

Table 5.2: Comparison of relevant experimental and simulated parameters for benchmark case 2.

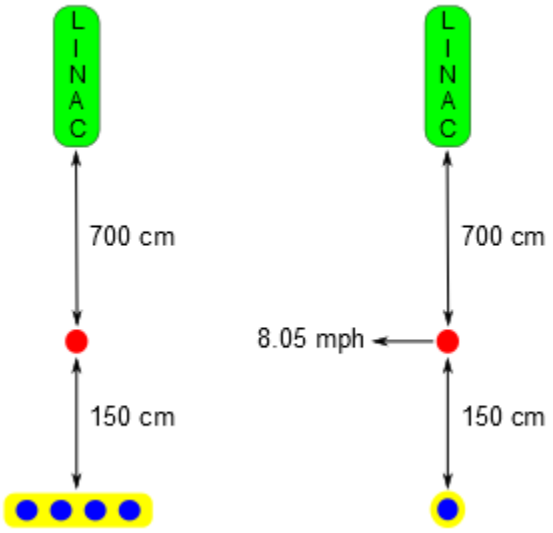

Figure 5.6: Comparison of the experimental and simulated geometries for benchmark case 2. *Left*: Actual setup. *Right*: XPASS setup.

As stated in benchmark case 1, XPASS models the AI source as a continuously pulsing beam of photons. Therefore, in order to replicate the signal from a single pulse from the linear accelerator, the pulse frequency was reduced from 50 Hz to 5 Hz. To reduce computation time, the signal from a single detector was modeled within XPASS and the results scaled by a factor of 4 to obtain an estimate for the detector count rate from the LAD.

In the XPASS simulation, the HEU was placed within a vehicle with a voided cargo container traveling through the interrogation system at 8.05 mph. A constant background of 23 cps was specified within XPASS, in accordance with the active background rate reported in [31]. Figure 5.7 shows the detector count rate for the first 20 milliseconds after the pulse. The results obtained through the XPASS simulation show the detector count rate falling to a value of 76.9 cps at 20 ms after the pulse. This result is about 23% lower than the experimental value of ~100 cps.

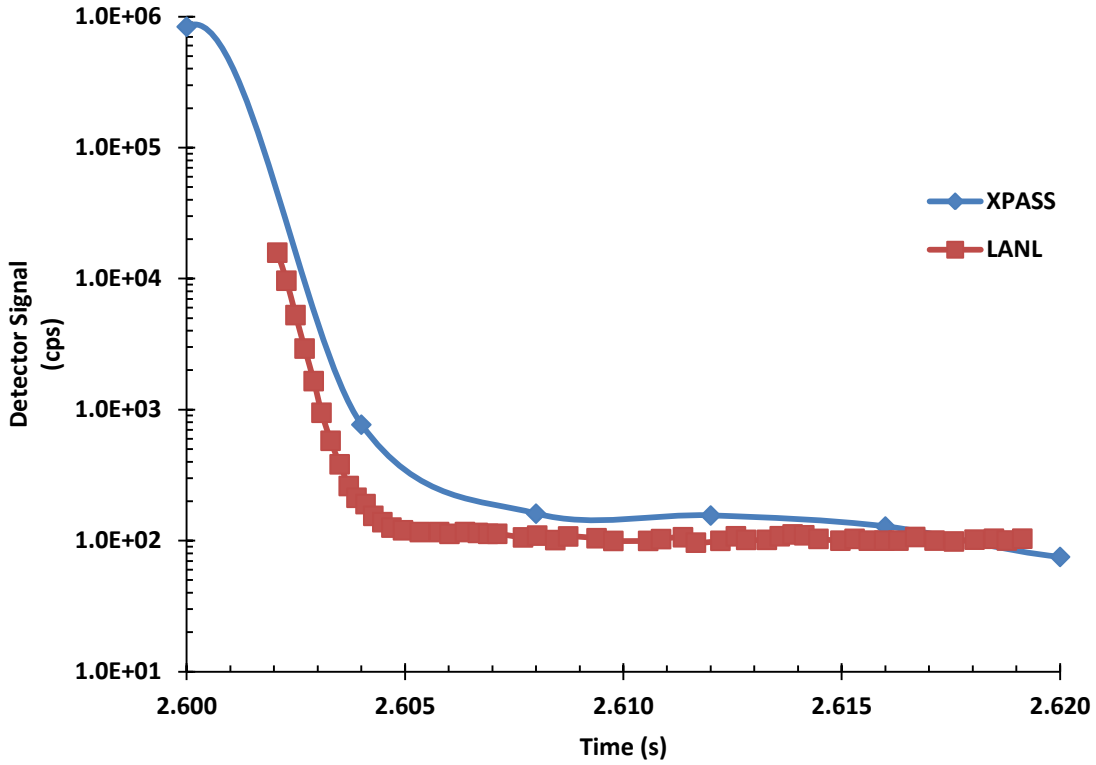

Figure 5.7: Detector signal for the first 20 ms after a pulse of 10 MeV photons on 22 kg of HEU.

5.1.3 Case 3: Count Rate Attenuation with Lead Shielding

The LANL paper in benchmark 2 also includes a case where slabs of lead (Pb) shield were placed between the linear accelerator and SNM, and the neutron count rate measured as a function of Pb thickness [31]. An analogous shielding configuration was modeled in XPASS and compared to the published results to determine if XPASS properly models the change in the detector signal in presence of shielding material. The SNM and source were the same described in benchmark case 2. Two LADs were placed 90 degrees from the beam axis on either side of the HEU; one LAD was set at a distance of 1.37 m from the SNM, and the other at 2.23 m. The neutron count rate for the first

20 ms after a single interrogation pulse was measured for shield thicknesses ranging from 2.54 cm - 15.24 cm.

The geometry in this benchmark cannot be completely replicated within XPASS as XPASS assumes the shielding material to be a spherical shell wrapped around the SNM. This differs from the benchmark case as the neutrons exiting the HEU in the experiment do not see the Pb shield, while in XPASS they must pass through in order to reach the detector. To minimize this difference in the geometry, the XPASS source code was modified so that the shield is present and visible to the interrogation photons as they penetrate the threat object, but is removed for neutrons exiting the SNM. Simulations were run with photonuclear production turned off within the shield, as well as turned on. As the distance between the shield and SNM in the experiment was not provided, these represent bounding cases for all neutrons born in the shield reaching and interrogating the SNM and no neutrons born in the shield reaching the SNM.

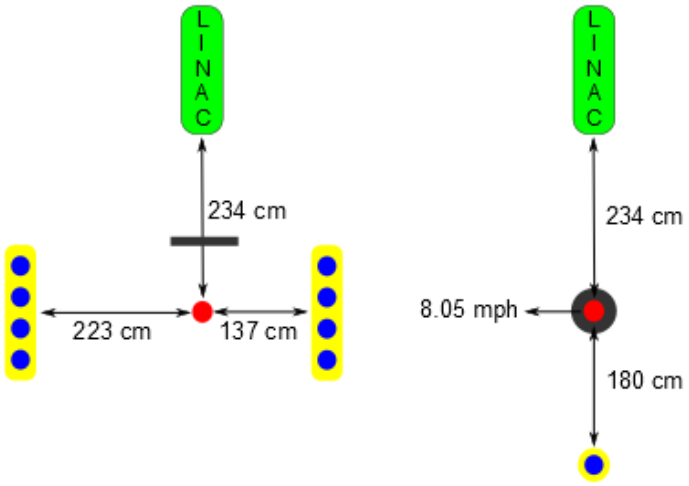

Figure 5.8: Comparison of the experimental and simulated geometries for benchmark case 3. *Left*: Actual setup with the Pb shield placed between the linac and HEU at an unknown distance. *Right*: XPASS setup with the Pb shield modeled as a spherical shell around the HEU.

	Experiment	XPASS
AI Source		
current	38 mA	38 mA
pulse width	6 µs	6 µs
frequency	single pulse	single pulse
distance to SNM	234 cm	234 cm
SNM		
mass	22 kg	22 kg
shielding	bare	bare
distance to detector	137 cm 223 cm	180 cm
Detector		
length	182.88 cm	182.88 cm
diameter	5.08 cm	4.99 cm
pressure	2 atm	6 atm
shielding	cadmium	none
moderator	yes	yes
efficiency	27%	*27%

*Simulated at 100% efficiency then multiplied by 0.27

Table 5.3: Comparison of relevant experimental and simulated parameters for benchmark case 3.

In the XPASS simulation, a single detector was placed at 1.8 m from the HEU which corresponds to the average distance of the two LADs in the experiment. The results obtained through XPASS for benchmark case 3 were multiplied by a factor of 2 to scale to number of LADs, then by a factor of 4 to scale to the number of He-3 tubes per LAD, then by a factor of 0.27 to account for the detector efficiency. Due to the differences in geometry between the simulated and experimental setups, it is not expected that the detector count rates will match. However, the geometries are sufficiently similar that count rates on the same order of magnitude may be expected. In addition to the introduction of shielding, the location of the HEU relative to the source and detector is

changed between benchmark cases 2 and 3 as well, with the case 3 geometry being more compact. This compaction of the geometry from benchmark case 2 to 3 should lead to an increase in the detector count rate for bare HEU. Table 5.3 gives a comparison of the relevant experimental parameters and the values used for the simulation within XPASS.

The increase in the neutron count rate going from benchmark case 2 to 3 is shown in figure 5.9 and is within a factor of 3 of the increase observed in the experimental result at 20 ms after the pulse; the simulated results are within a factor of 5 at earlier times. As stated previously, the absolute increase was not expected to match as the geometry in the XPASS simulation for benchmark case 3 is not a good representation of the experiment. Because the geometry of the shielding experiment could not be well replicated in XPASS, the simulation results were renormalized so that the neutron count rate for the bare HEU matches the experimental value of ~835 cps at 20 ms after irradiation. Once this absolute renormalization is done, the relative changes due to the addition of various thickness of Pb shielding on the detector count rate can be meaningfully compared to the published values.

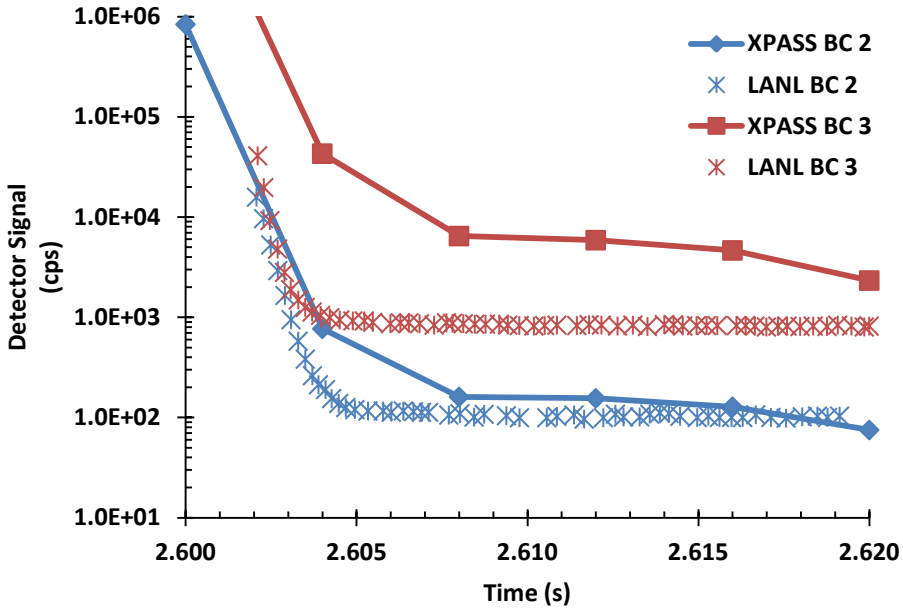

Figure 5.9: Neutron count rate increase between benchmark cases 2 and 3 for 22 kg of HEU.

The detector count rates for Pb shield thicknesses of 2.54 cm, 5.08 cm, and 10.16 cm are plotted in figures 5.10 and 5.11 for the two XPASS cases corresponding to photonuclear production within the Pb shield being off and on. As expected, the XPASS results bound the published results. Without knowing the exact geometry or being able to calculate the number of neutrons produced within the shield that made it to the SNM in the experimental results, all that can be said is that XPASS matches the sensitivity to a change in the shielding configuration. It is important to note that the shield produces (n,2n) neutrons as well as increase the effective multiplication factor of the SNM-shield system, augmenting subcritical multiplication of delayed neutrons.

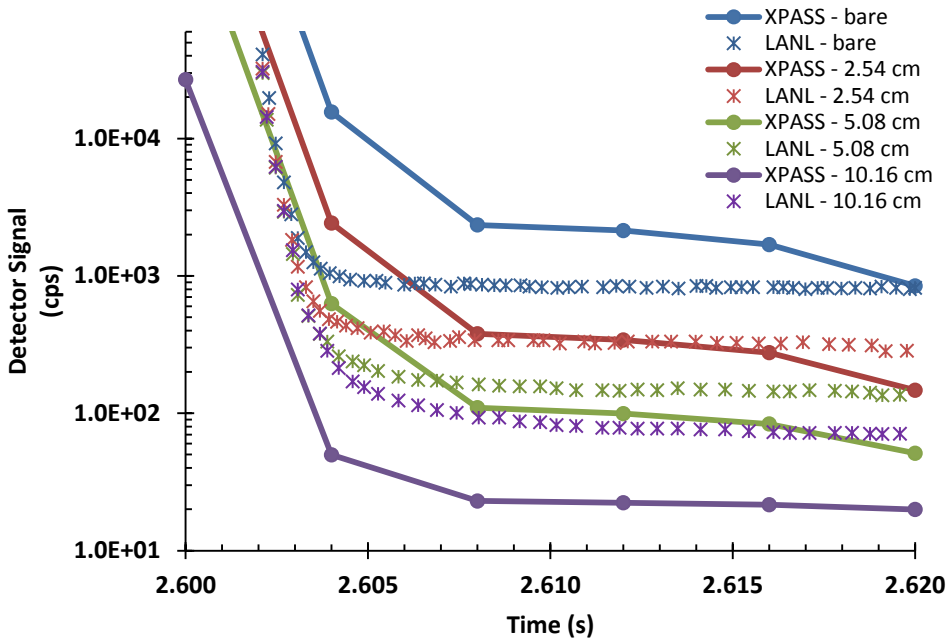

Figure 5.10: Neutron count rate for various thicknesses of Pb shield between the source and 22 kg of HEU. Photoneutron production in shield turned off.

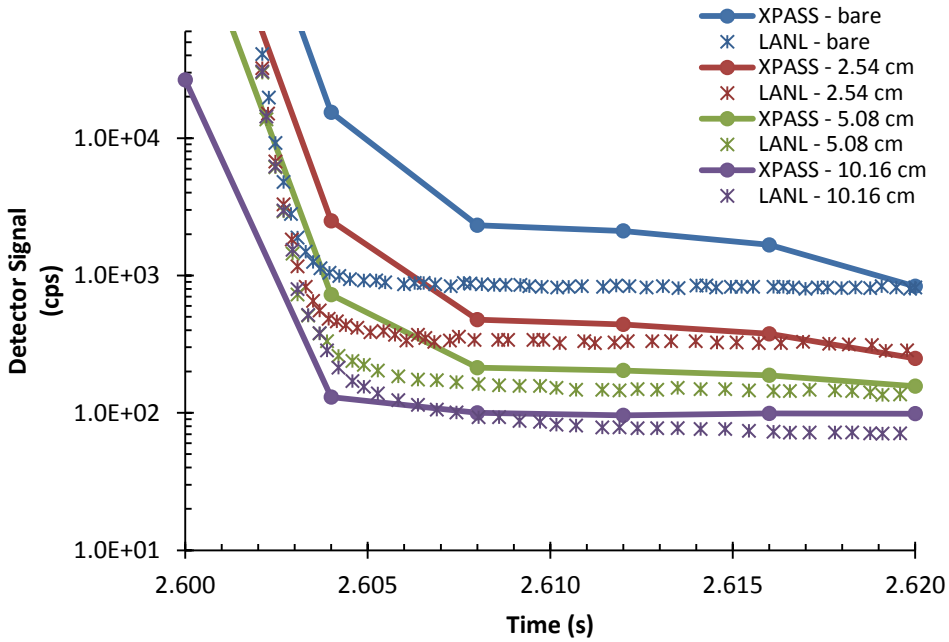

Figure 5.11: Neutron count rate for various thicknesses of Pb shield between the source and 22 kg of HEU. Photoneutron production in shield turned on.

5.2 APPLICATIONS

This section provides case studies illustrating the sensitivity of the neutron count rate to key factors defining an AI scenario. These application cases demonstrate the power of XPASS as time dependent detector spectra from a time dependent source, that is not in steady state and is moving with time, are able to be calculated.

5.2.1 Detector Signal vs. SNM Location in Cargo

XPASS was used to simulate the time dependent neutron count rate from a 5.3 kg bare sphere of HEU placed within 0.2 g/cm^3 high Z cargo (structural steel). The vehicle velocity through the interrogation system was set at a constant speed of 8.05 mph, and the AI source generated 10 MeV (maximum energy) photons at a frequency of 10 Hz. The HEU was simulated at 4 locations along the length of the cargo, at positions 750 cm, 350 cm, 0 cm, and -400 cm relative to the center of the cargo. Although an active background would be present during an interrogation, to isolate the change in the detector signal originating from the SNM, active background count rates were not calculated for these simulations.

Figure 5.12 shows the detector count rate for each of the simulated locations of the SNM. Relative to the 0 cm location, the curves for each location are shifted forward or back in time in accordance with the location of the SNM. The width of the peak regions, corresponding to the time the SNM is directly under the beam, are unchanged between the cases. The tail regions are also nearly unchanged relative to the 0 cm case. This behavior makes sense as the only change between each scenario is the time at which the SNM intersects the interrogation beam. The minor differences present in the spectra are due to the limitations of the time binning structures, and the assumption that the particles are uniformly distributed within each time bin.

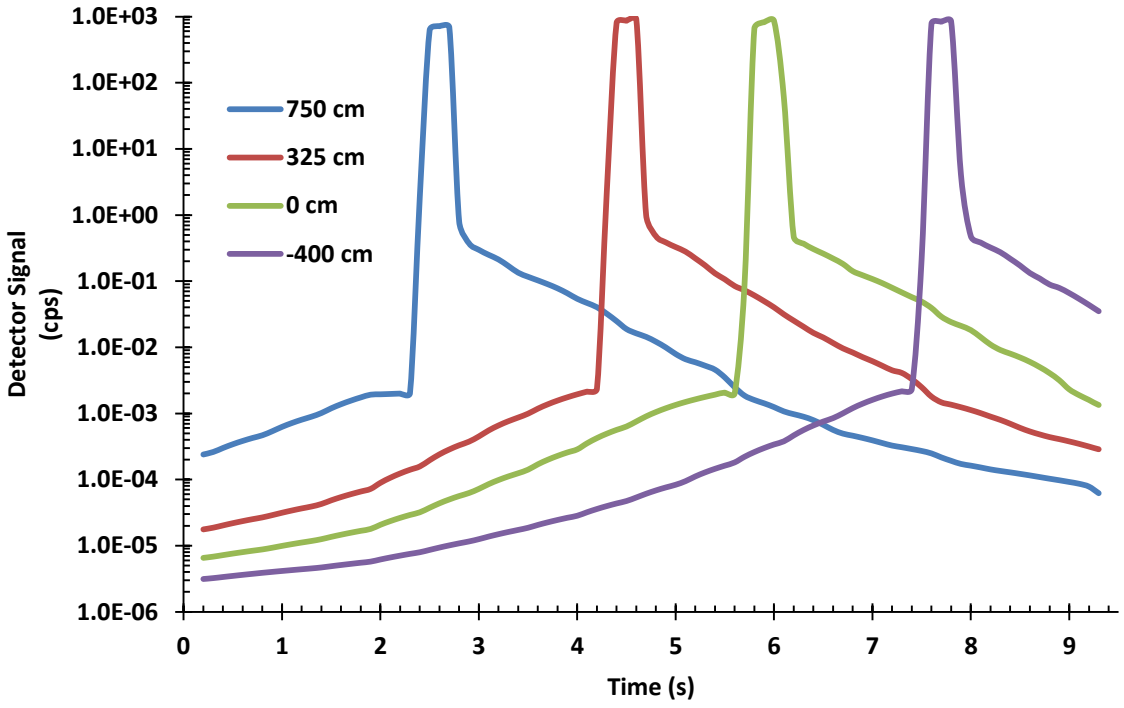

Figure 5.12: Neutron count rate as a function of SNM location within the cargo.

5.2.2 Detector Signal vs. Vehicle Velocity

To understand how the velocity of a vehicle traversing through an interrogation system affects the measured neutron count rate, XPASS was used to simulate several scenarios where the speed of the vehicle was varied. A detailed study such as this can help determine the maximum speed a vehicle can traverse through an interrogation system while not significantly reducing the ability to detect the presence of SNM. Determination of this maximum speed will help reduce the impact of AI on the flow of commerce, and reduce the cost associated with screening vehicles.

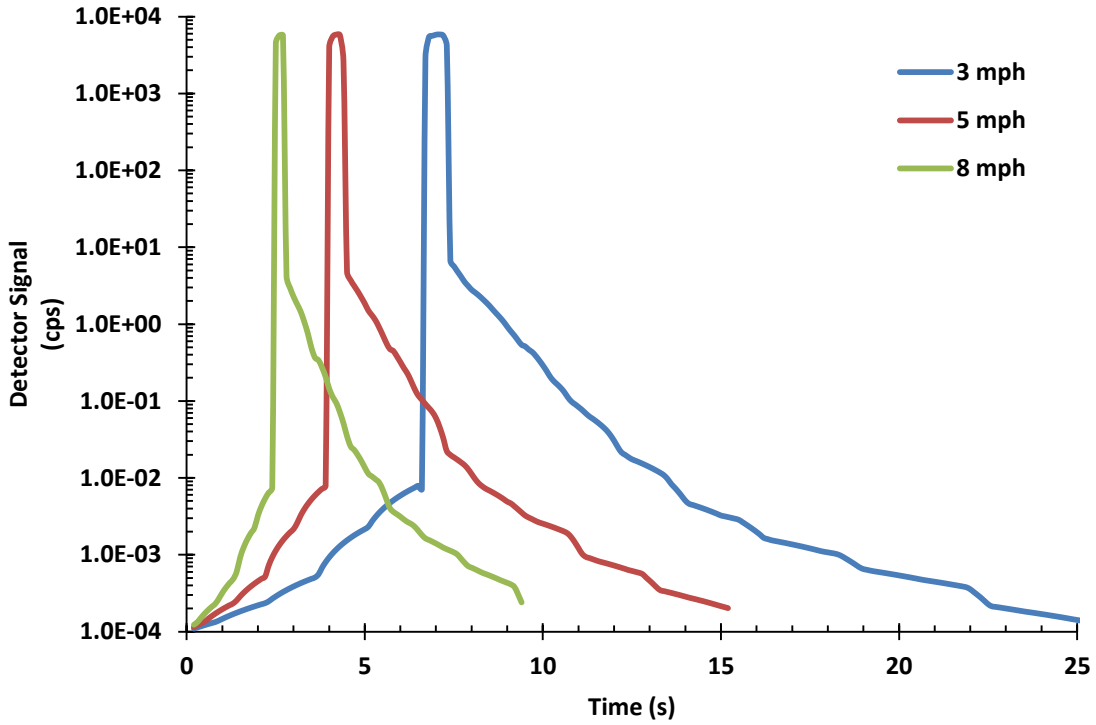

Figure 5.13: Neutron count rate as a function of vehicle velocity.

A 5.3 kg sphere of bare sphere of HEU was placed within 0.2 g/cm^3 high Z cargo (structural steel). The AI source generated 10 MeV (maximum energy) photons at a frequency of 10 Hz. The vehicle velocity was simulated at 3 mph, 5 mph, and 8 mph. Figure 5.13 shows neutron count in a detector for each of the simulated vehicle velocities.

It can be seen from figure 5.13 that as the vehicle velocity slows, it takes longer for the SNM to reach the location of the beam, and therefore the peak corresponding to when the SNM is irradiated gets shifted back in time. Also, the width of the peak increases with decreasing vehicle velocity, as the SNM spends more time under the beam for lower vehicle velocities. The tail region starts off at a slightly higher value for lower velocities, as there is more buildup of the neutron signal due the SNM being irradiated by more pulses the longer it spends under the beam. In addition, the tail region falls off

more slowly with a lower velocity. This is because the fall off in the tail region is due to two components, decay of the delayed neutron signal as well as increasing geometric attenuation. While the delayed neutron signal decay is identical for each vehicle velocity, the geometric attenuation increases faster for a vehicle traveling at a higher speed. Table 5.3 shows the differences in the time it takes for the detector count rate to reach $1/e$ times the value immediately after the final pulse hits the SNM.

	3 mph	5 mph	8 mph	
Count rate after final pulse	6.71	4.79	4.21	cps
Decay time	0.80	0.60	0.40	seconds

Table 5.3: Detector signal decay time for vehicles traveling at various speeds.

5.2.3 Deployed Systems Comparable to Benchmark Cases 1 and 2

In a true interrogation scenario, the linear accelerator is constantly pulsing and the neutron count rate is measured between pulses. Any SNM of reasonable size will likely be irradiated by multiple pulses of photons as the vehicle is being scanned. Therefore, the neutron count rate measured between pulses will not only include neutrons produced from the immediately preceding pulse. Rather, there will be a superposition of neutrons from all previous pulses that interacted with the SNM. This leads to a buildup of the neutron count rate, as each pulse contributes delayed neutrons to the detector at later times. Figure 5.14 shows the detector count rate as a function of time for the system given in benchmark case 1. The only difference in this scenario as opposed to what was done in benchmark case 1 is the frequency of interrogation pulses is set at the actual value of 125 Hz given in the literature, as opposed to being reduced to 5 Hz to obtain a single pulse on the SNM.

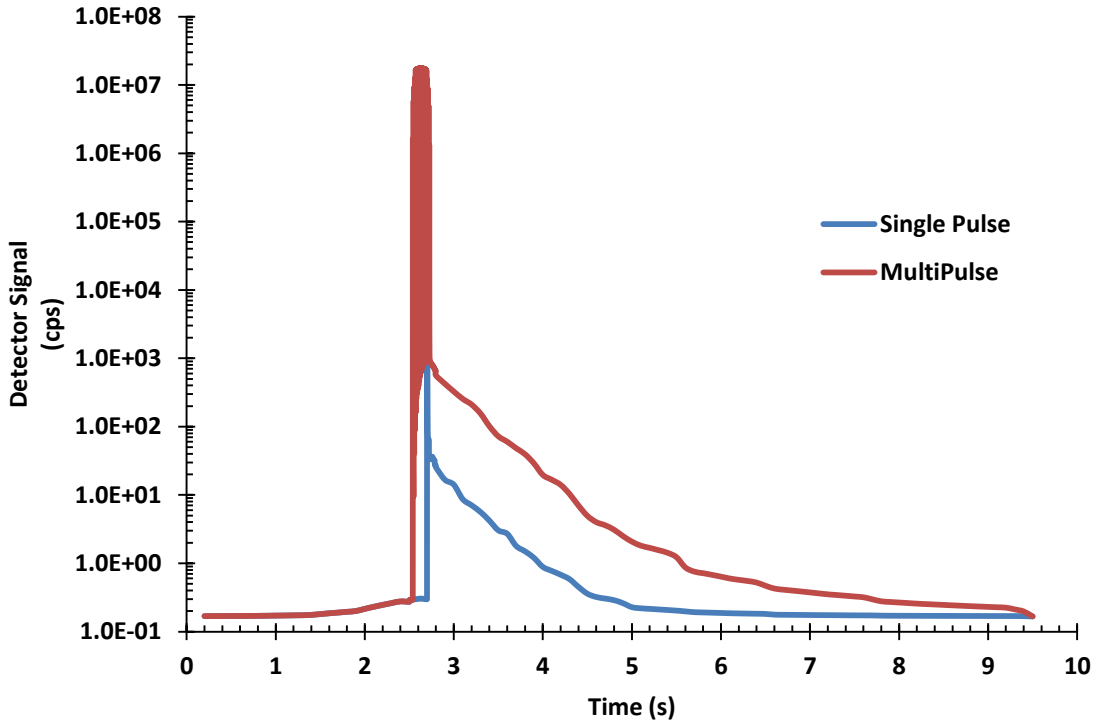

Figure 5.14: Time dependent detector count rate for an interrogation system modeled after benchmark case 1.

Comparing the curves in figure 5.14, it can be seen that immediately following the interrogation of the HEU, the detector count rate is much higher for the multipulse case as compared to a single pulse. Because multiple pulses have activated the HEU, it takes longer for the tail region to completely die off to background levels, as it starts its decay from a higher value. Figure 5.15 plots the detector count rates for the interval of time when the beam is irradiating the HEU. Figure 5.15 shows the behavior of the detector count rate between pulses building up to a constant value as the number of pulses hitting the HEU increases. This saturation value is most likely a function of k_{eff} as well as the delayed neutron fraction and precursor decay constant.

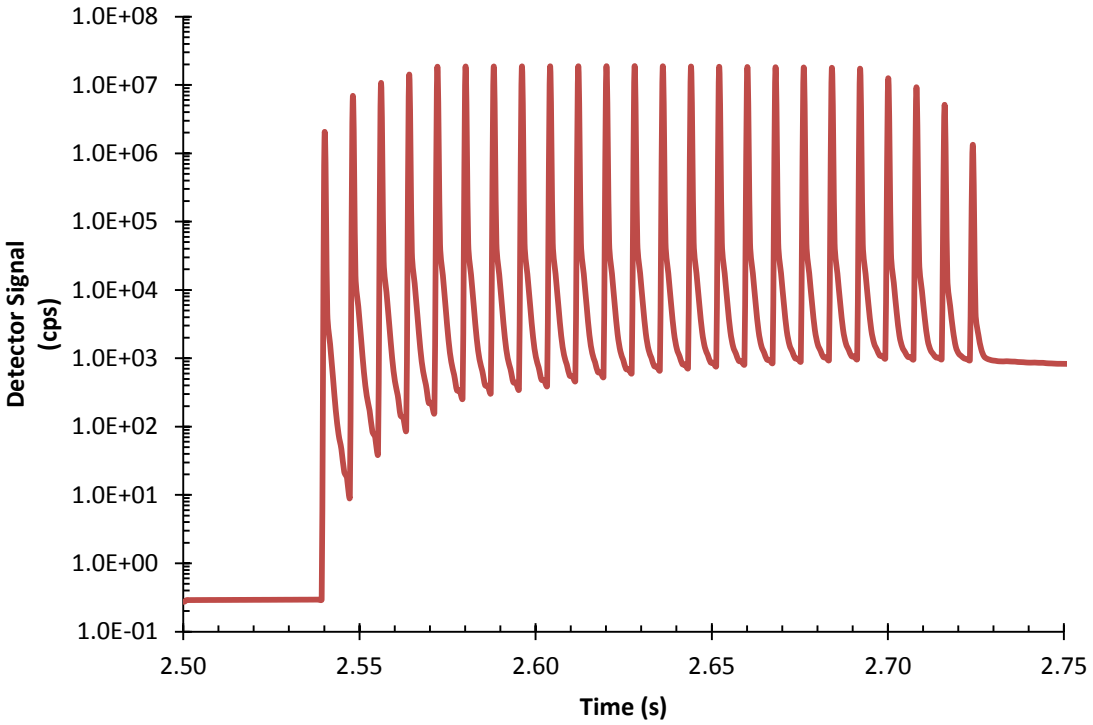

Figure 5.15: Build up of detector count rate with number of pulses hitting SNM.

Figures 5.16 and 5.17 show the detector count rate as a function of time for a system modeled after benchmark case 2. The only difference in this scenario as opposed to what was done in benchmark case 2 is the frequency of interrogation pulses is set at the actual value of 50 Hz given in the literature, as opposed to being reduced to 5 Hz.

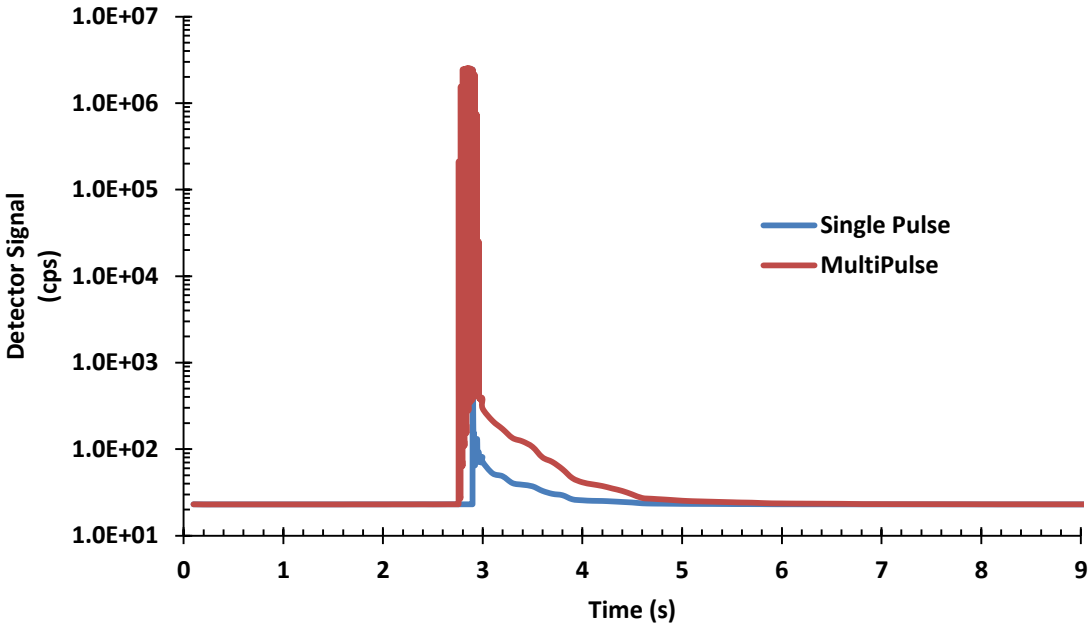

Figure 5.16: Time dependent detector count rate for an interrogation system modeled after benchmark case 2.

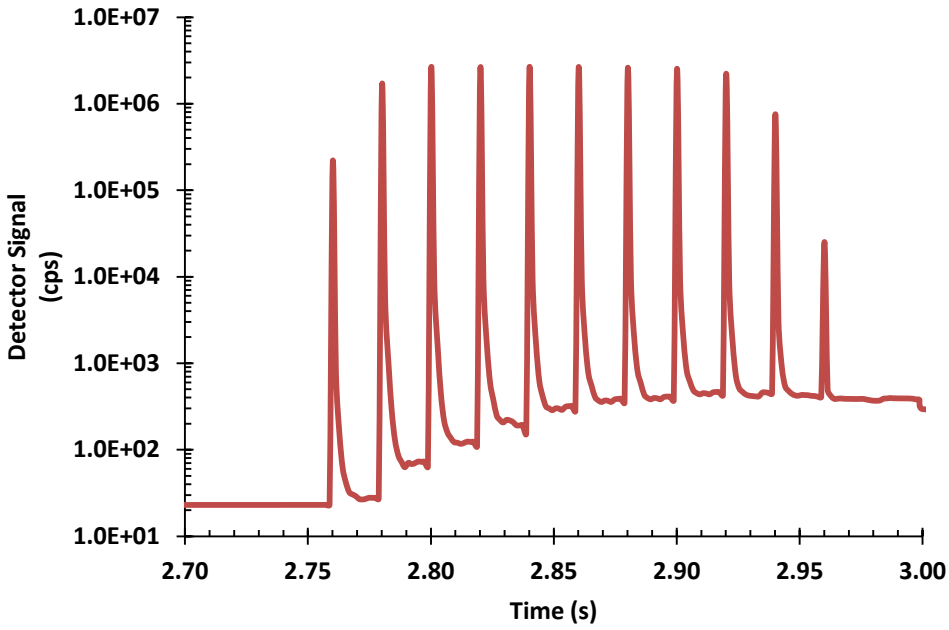

Figure 5.17: Build up of detector count rate with number of pulses hitting SNM.

5.2.4 Active Background vs. Beam Energy and Cargo Type

Induced background from the interrogation of bulk cargo with high energy photons results in a reduced DP for a given FAP. The reduction in the DP is caused by the large increase in the background count rate induced from the cargo. XPASS was used to simulate the induced active background from several bulk cargo materials of low Z (wood), mid Z (ceramic tile), and high Z (structural steel), as well as a 1:1 combination of low Z/void, mid Z/void, and high Z/void material. These scenarios were simulated to obtain a crude understand of the variation in the induced active background as a function interrogation energy for various bulk cargo materials. Table 5.4 gives the MCNPX isotopic composition used for each of the bulk material types.

Low Z	(Wood)	Mid Z	(Ceramic Tile)	High Z	(Structural Steel)
1001	-5.79E-02	8016	-5.25E-01	14000	-1.01E-02
6000	-4.80E-01	13027	-5.23E-03	24000	-1.69E-01
8016	-4.60E-01	14000	-4.49E-01	25055	-2.00E-02
		20000	-1.44E-02	26000	-6.55E-01
		26000	-7.21E-03	28000	-1.20E-01
				42000	-2.51E-02

Table 5.4: Isotopic compositions of XPASS bulk cargo materials.

XPASS was used to run a parameter sweep interrogating over the various bulk cargo materials and interrogation source energies. The induced active background is plotted in figure 5.18 for each bulk cargo material as a function of energy. Two trends can be taken from the figure. The first is the induced background becomes larger with increasing interrogation energy, and the second is that the induced background is larger for bulk cargo with higher Z. However, the second trend is not strictly true, as the photonuclear thresholds are isotope dependent. This is why the active background does not come into play until 11 MeV for the mid Z material, while both low Z and high Z

material have isotopes with a photonuclear threshold at around 9 MeV. Because of the isotopic dependence on the photonuclear threshold, treating the bulk cargo materials as being generally representative of low Z, mid Z, and high Z materials may not be valid for AI scenarios. This general representation was originally done in XPASS for passive interrogation systems as photoatomic interactions with the bulk cargo, which are well characterized by photon energy as well as cargo density and Z, were of greatest interest. For AI, photonuclear interactions are of greatest interest and the isotopic composition of the material can make a significant difference in the induced background. Therefore, when AI systems are of interest, the low Z, mid Z, and high Z bulk cargo material built into XPASS cannot be said to be generally representative of low Z, mid Z, and high Z cargo, but rather are only representative of wood, ceramic tile, and structural steel respectively.

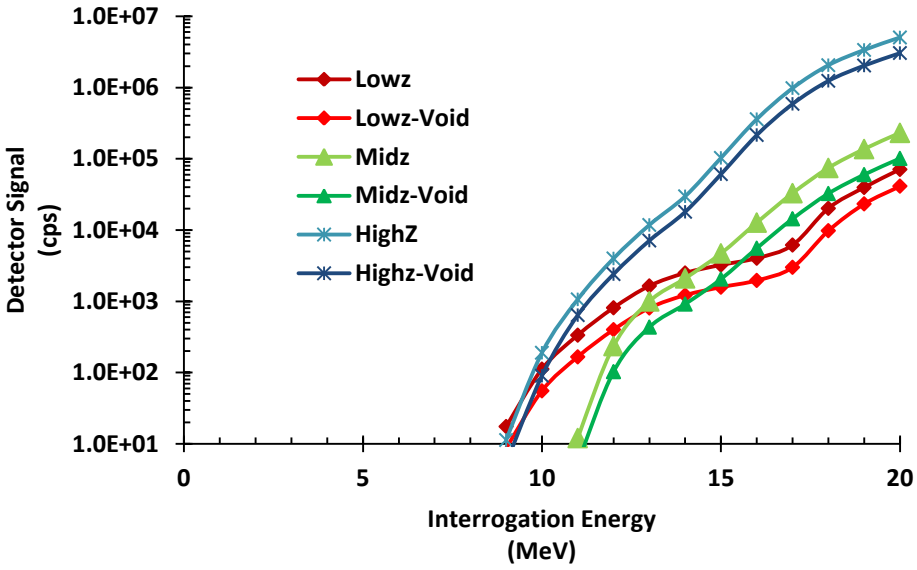

Figure 5.18: XPASS simulated induced active backgrounds for several bulk cargo types.

The variation in the induced active background with cargo material leads to a reduced ability to detect SNM. This is because without prior knowledge of what the induced signal will be, the alarm threshold must be set a value greater than what would be expected from common bulk cargo material (unless a high rate of false positives is acceptable). The difference in the induced background between structural steel and wood is two order of magnitude. If an alarm threshold was set at a value based upon structural steel so that it produces a low FAP for all cargos materials, shielded SNM embedded in wood may never trip a GC alarm as the detector count rate may always be below the threshold. Figure 5.19 plots induced active background for each interrogation averaged over each bulk cargo type. It also plots, on a separate axis, the ratio between the standard deviation σ and the mean μ of the induced background.

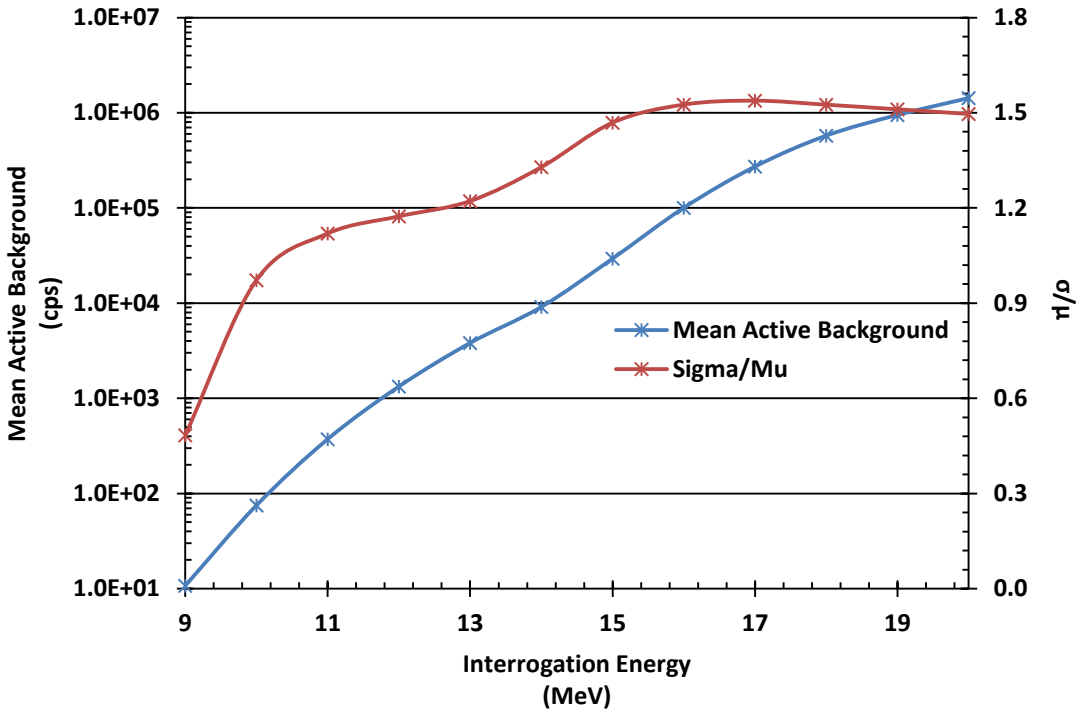

Figure 5.19: Average induced background as a function of interrogation energy.

If the induced active background was well characterized, the increase in background could be taken into account in setting the alarm threshold. This would be accomplished by matching the interrogation energy and alarm threshold based upon what is reported in the cargo manifest. If a larger than expected neutron signal is measured, it could be indicative of the presence of SNM or a manifest that does not accurately describe the contents of the cargo. Either case would warrant further inspection. XPASS can be used as a simulation tool for determining the expected neutron count rate for a large variety of bulk cargo material at each possible interrogation energy. A much more exhaustive parameter sweep would be require. The parameter sweep should encompass many more bulk cargo material types, as well as span many combinations of multiple cargo types. Without this matching of the threshold based upon the expected induced background, the uncertainty in the total background signal caused by the uncertainty in the induced background will swamp out any statistical variations due to the Poisson process associated with other sources of radiation background. This uncertainly will then become the limiting factor in the ability to reliably screen cargo for SNM.

5.2.5 Detector Signal vs. Shielding Configuration

The effect on the detector count rate from the addition shielding material around the SNM was investigated using XPASS. Three cases involving Pb shielding, 10% borated polyethylene (BPE) shielding, and a combination of Pb and BPE shielding were simulated and analyzed. For all cases, unless otherwise stated, the scenario involved a 5.5 kg sphere of HEU placed within a voided cargo container. The interrogation source produced photons at 10 MeV (maximum energy), at a frequency of 50 Hz. Background calculations were turned off so that the change in the neutron count rate originating from the SNM due to a change in shielding configuration could be studied. These scenarios

represent several potential shielding strategies and understanding the effect the type of shielding and the configuration of the shielding has on the detector count rate can lead to improved techniques for detection of shielded SNM.

Borated Polyethylene Shield

Simulations for several thicknesses, between 2 mm and 40 mm, of BPE shielding material placed around the HEU were run. The intent of this shielding configuration is to moderate and absorb neutrons produced within the SNM, reducing the number that reach the detector. The detector count rate for each shield configuration was compared to that from bare HEU. Figure 5.20 shows the detector count rate for the various shielding configurations.

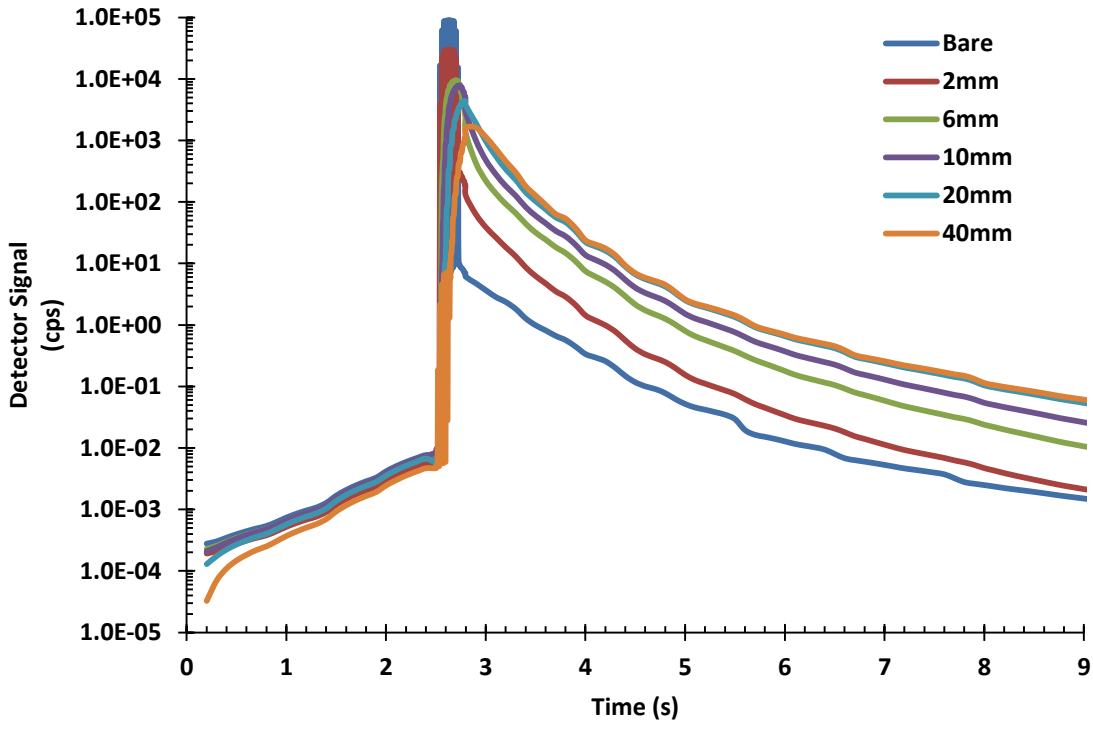

Figure 5.20: Neutron count rate as a function of BPE shield thickness.

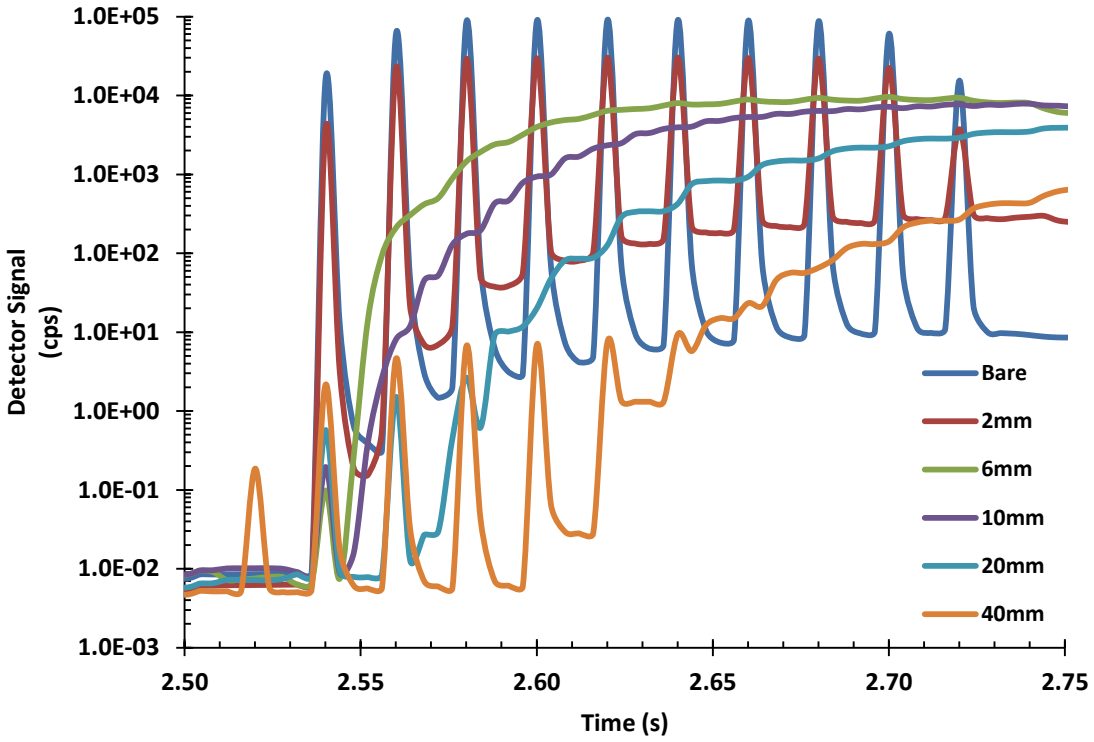

Figure 5.21: Neutron count rate during irradiation as a function of BPE shield thickness.

Figure 5.20 shows an interesting behavior where the peak neutron count rate during irradiation decreases when BPE shield is present, but the neutron count rate after irradiation increases with increasing BPE thickness. This behavior can be understood by looking at what happens during the irradiation of the SNM, shown in figure 5.21.

The signal during an interrogation pulse is dominated by prompt fast neutrons transporting directly to the detector. Delayed neutrons contribute to the count rate after and between each pulse. These delayed neutrons may scatter back to the SNM from the shielding to produce fast neutrons at a later time through subcritical multiplication. The buildup of the detector signal with shielding thickness, shown in figure 5.21, is driven by thermalization of the prompt neutrons by the shielding. The figure shows the buildup becoming shifted later in time as the thickness of the BPE shield increases. This makes

sense as neutrons scatter within in the polyethylene for a longer period of time as the thickness of the shield increases. The peak count rate is decreases when BPE shielding is present, but this decrease is accompanied by an increased count rate after the pulse. The decrease in the peak is partially caused by neutrons being absorbed within the BPE. However, as the BPE thickness increases, neutrons that would have reached the detector during or immediately after the interrogation pulse become more likely to be moderated and experience a much longer migration time to the detector. This also leads to a decrease in the neutron count rate during the pulse, and is what causes an increase in the neutron count rate at later times.

The moderation of the prompt neutrons may play a key factor in the detection of the SNM. While the BPE does generally lead to a decrease in the total number of neutrons entering the detector, it also leads to an increase in the number of detectable neutrons that can be used to signal an alarm. This is a because majority of the neutrons that reach the detector are within the large peaks for bare and lightly shielded SNM. Those peaks correspond to time periods when the source is actively interrogating the SNM. However, during those periods the detector systems are typically off as they would be saturated from background from the source. Therefore, the large increase in the neutron count rate from prompt neutrons streaming to the detector is typically not used in alarm algorithms. While the addition of BPE shielding will absorb and reduce the number of prompt neutrons making it to the detector, the larger effect is to thermalize and delay in time when those neutrons reach the detector. If the neutrons are delayed enough such that they reach they detector between pulses when the detector is on, a net increase in the DP will be observed as the neutrons are now useful in detection. Understanding the tradeoff between neutron absorption within the BPE, and moderation of the prompt neutron peak can lead to improved techniques for detecting SNM.

Lead Shield

A sensitivity study was carried out upon several thicknesses, between 2 mm and 40 mm, of lead (Pb) shielding material placed around the HEU. The intention of this configuration is to attenuate the interrogating photons, as opposed to attempting to absorb the photoneutrons produced within the SNM. The detector count rate for each shield configuration was compared to that from bare HEU. Figure 5.22 shows the detector count rate for each of the various shielding configurations.

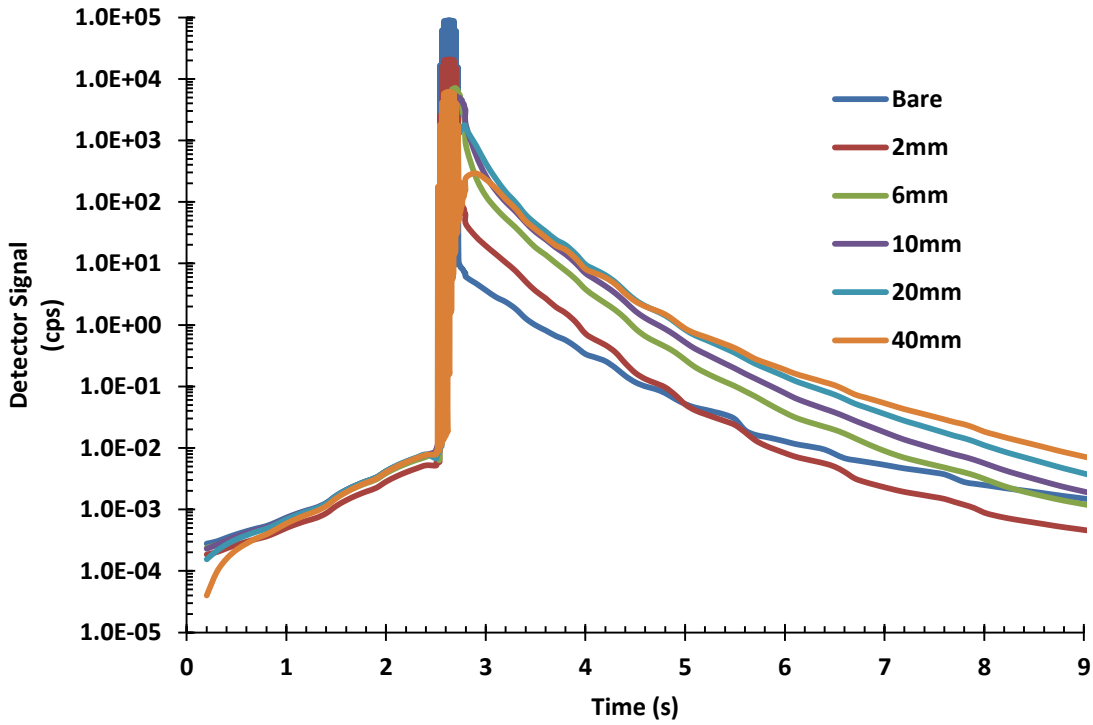

Figure 5.22: Neutron count rate as a function of Pb shield thickness.

The peak neutron count rate is seen to decrease in the presence of Pb shielding as one would expect. However, figure 5.22 shows that similarly to BPE shielding, the neutron count rate immediately after the SNM is interrogated is seen to increase in the

presence of shielding. This is due to neutron scattering in the Pb shield as there is no longer a direct unimpeded path from the SNM to the detector..

Figure 5.23 focuses in on the 0.25 second time interval during and immediately after delivery of the pulses that irradiate the HEU. The behavior is similar to that of the BPE case, with one major distinction. The decline in the prompt neutron count rate with shielding thickness is much less dramatic than was the case for an equal thickness of BPE. Indeed, as the Pb thickness is increased past 20 mm, the count rate during the pulse beings to increase with shield thickness. This is caused by increasing photo-neutron and (n,2n) production within the Pb shield. As the thickness of the Pb shield increases, the decrease in the photon intensity is offset by an increase in photo-neutron production within the shield. The neutrons produced within the shield interrogate the SNM and result in the emission of additional neutrons. The peaks at ~2.53 sec and ~2.74 sec (also present in the BPE case, but 2 orders of magnitude smaller) are caused by photo-neutrons produced within the shield which scatter into the SNM. At 40 mm thickness, the threat object is large enough so that an additional pulse at either end will intersect the shield and create neutrons that reach the SNM.

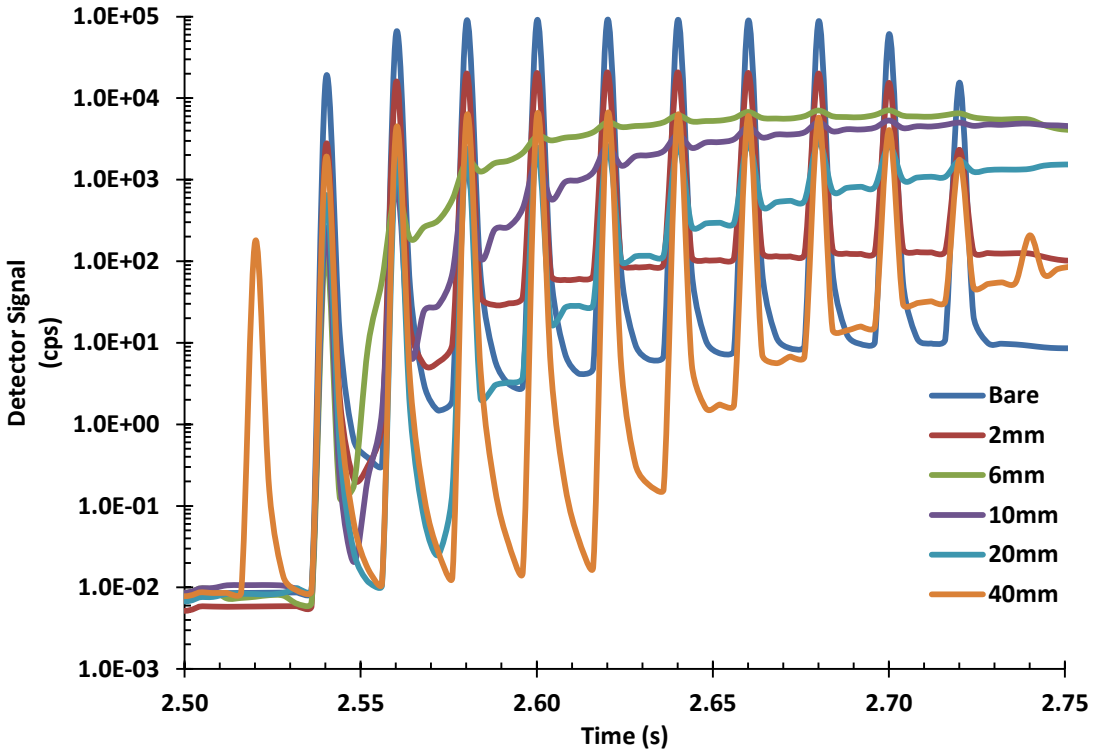

Figure 5.23: Neutron count rate during irradiation as a function of Pb shield thickness.

Nested Lead & Borated Polyethylene Shields

XPASS was used to simulate the neutron count rate for various combinations of nested layers Pb and BPE shielding. The goal of this shielding configuration is to both decrease the interrogating photon intensity as well as absorb the emitted neutrons. Two layers of shielding, 2 cm and 4 cm thick, were placed around the HEU. The order of the shielding layer thickness was varied (2 cm inner layer, 4 cm outer layer vs. 4 cm inner layer, 2 cm outer layer), as well as the order of the shielding material (Pb inner layer, BPE outer layer vs. BPE inner layer, Pb outer layer). Figure 5.24 shows the detector count rate for each of these cases as well as that for the bare HEU.

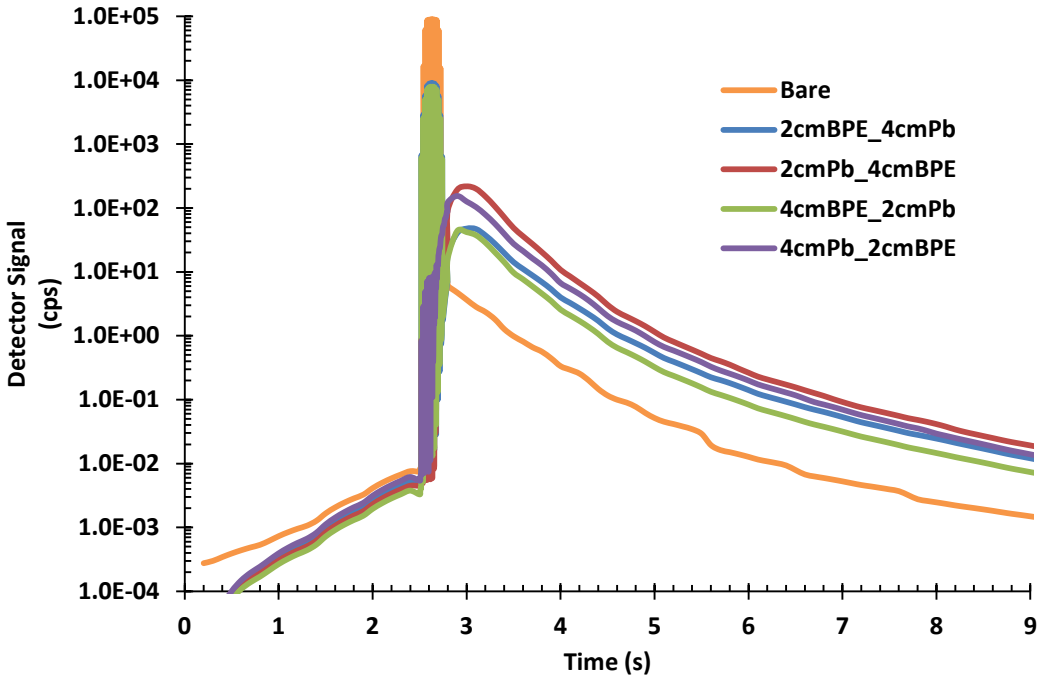

Figure 5.24: Neutron count rate as a function of nested shield configuration. First layer listed is the inner shield, second layer is the outer shield.

Figure 5.24 shows the same behavior that was seen previously, where the neutron count rate after irradiation of the HEU is increased in the presence of shielding, as compared to the bare case. Figure 5.25 shows that for configurations where Pb is the inner layer, the peak count rate when the beam is on is significantly reduced compared to configurations which have Pb as the outer layer. However, figure 5.24 shows that after shortly after irradiation the count rates switch, and the configuration with Pb as the inner layer produces a higher neutron count rate.

The behaviors shown in figure 5.24 and 5.25 can be understood by following the transport of neutrons produced within the Pb shield. When the Pb shield is the outer layer, neutrons produced within it have a direct path to the detector. This leads to the relatively large detector counts rate during the interrogation pulse. When Pb is the innermost layer of shield, the neutrons produced within must first travel through the BPE

before reaching the detector. The neutrons become thermalized and spread out in time as well as absorbed as they pass through the BPE, leading to a greatly reduced peak count rate during the interrogation pulse.

On the other hand, when the Pb is the innermost layer of shielding, the inward directed neutrons produced within the shield have a direct path to the SNM. Therefore the neutron interrogation source, born within the shield, which reaches the SNM is relatively large. Whereas when the Pb is the outer shielding layer, many neutrons thermalize and become absorbed as they must first pass through the BPE before reaching the SNM. Still, some of these neutrons will make it though the BPE and interrogate the SNM, leading to additional neutron production. However, the neutrons produced within the SNM must also pass through the BPE on their way out to the detector. Therefore, when Pb is the outermost layer of shield, there must be at least two crossings through the BPE shielding layer before neutrons born within the SNM, from neutrons produced in the Pb, shield can make it to the detector. This is what leads to the switching in the detector count rates shortly after the irradiation of the SNM.

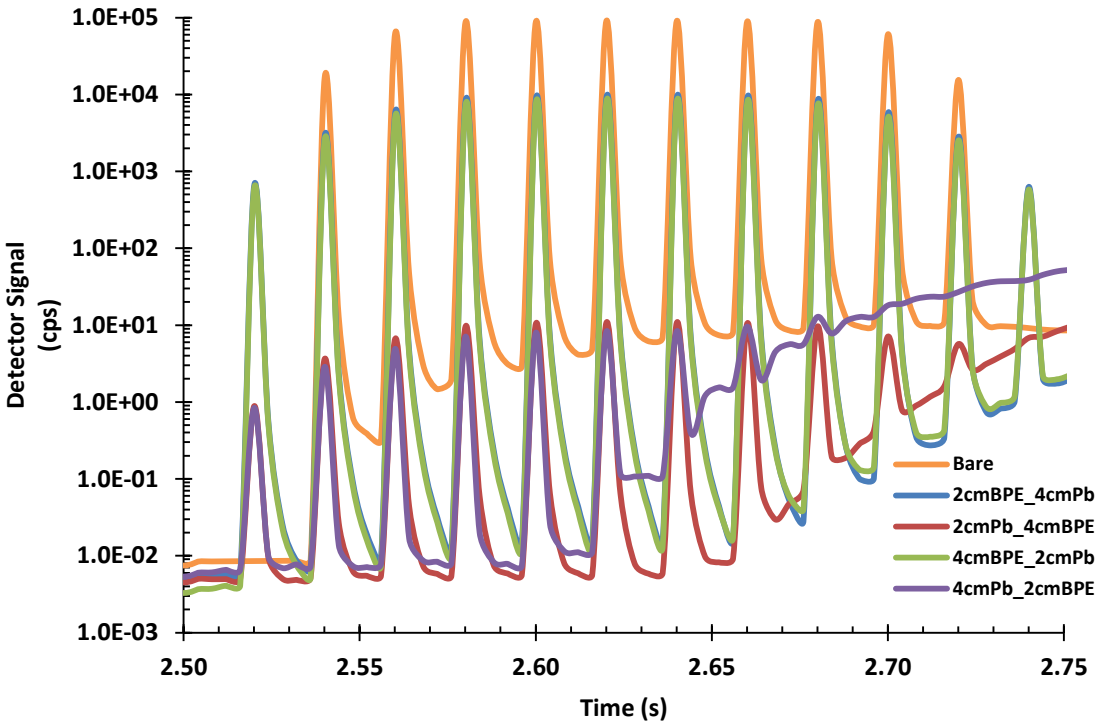

Figure 5.25: Neutron count rate during irradiation as a function of nested shield configuration.

XPASS calculates both the detector spectra as well as the DP as a function of time for a range of FAPs. The output file for the AI mode is formatted in a way which is convenient for plotting this data (see section 4.7.3). However, XPASS does not allow the user to explicitly set the alarm threshold for calculation of the DP. Rather, it computes the threshold that gives the desired FAP based upon the computed background count rate. XPASS assumes a normal distribution with $\sigma^2 = \mu$ based upon Poisson statistics. However, as discussed in section 5.2.4, this is not correct for AI scenarios unless the induced active background can be extremely well characterized. If not, the uncertainty from the large variation in possible induced background count rates will swamp any

statistical uncertainty and lead to a large reduction in at ability to reliably detect the presence of SNM. Adding the ability for the user to explicitly set the alarm threshold will allow XPASS to compute much more meaningful DPs, as the user can set the threshold based upon their understanding of the mean background count rate and the variance of it. Using XPASS in its current state, the analysis given below is not meant to be interpreted as the true DP for the modeled scenarios. Rather the trends in the DP and the behaviors of the ROC curves, as well as an illustration of the ability to compute these within XPASS, are what is attempting to be shown.

Two of the nested shielding cases were chosen for simulation in low Z (wood) bulk cargo with the active background calculation turned on to study how the detection probability is affected by the layering of differing shield materials. The cases chosen were HEU wrapped with a 2 cm thick inner layer, and 4 cm thick outer layer of shielding material where the order of the Pb and BPE was interchanged

Figure 5.26 shows the DP, for a 1% FAP, as a function of time for the configuration where BPE is the inner shield layer. The DP at each time step was calculated using a GC algorithm where the detector count rate was integrated over corresponding time bin. The time dependent neutron count rate is equivalent to the blue curve in figures 5.24 and 5.25, with the addition of an active background calculated to be 120.975 cps. In this scenario, the shielded HEU is physically within the beam for the time period between 2.5 and 2.75 seconds. The detection probability spikes to a value of 1 during each pulse within this period. However, as XPASS does not model detector saturation or dead time effects, and these spikes in DP are typically not "usable" as the detector is not counting during and immediately after the beam pulse. These spikes are shown in figure 5.26 only as a reference to where the maximum DP occurs in relation to when the SNM is irradiated. In between pulses during irradiation, the detection probably

falls to essentially the FAP (1%) as the active background dominates any small increase in signal from the SNM. However, as time progresses, the DP increases to a value of 14.2% as neutrons make their way out of the shield. The peak in the DP at 3.0 seconds corresponds to the peak in the tail region of figure 5.24.

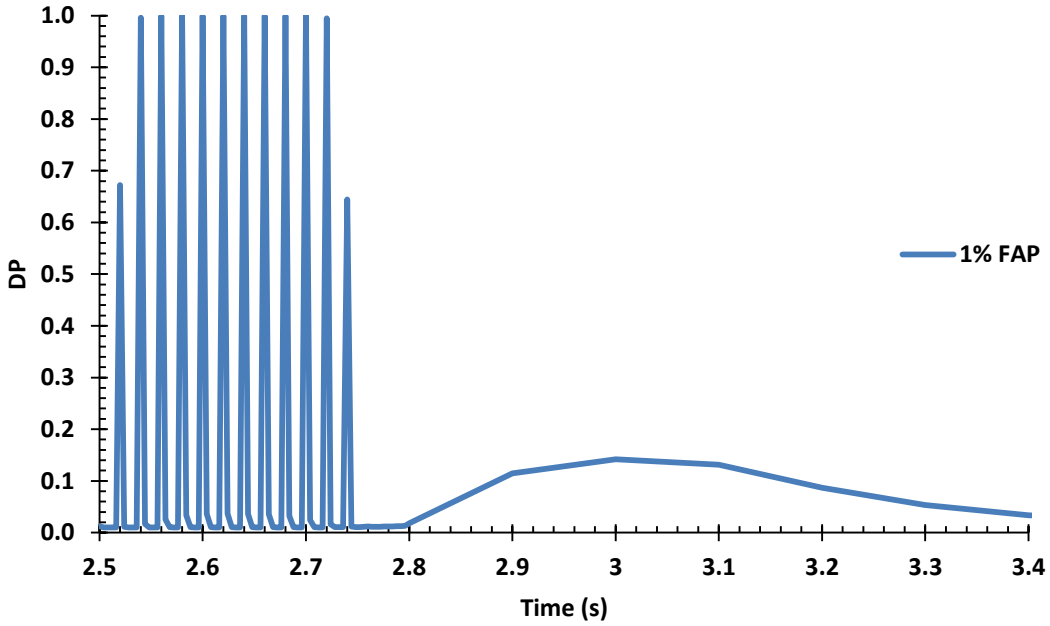

Figure 5.26: Detection probability at various times during and after irradiation of HEU shielded with a 2cm inner layer of BPE and 4cm outer layer of Pb.

Receiver operating characteristic (ROC) curves were generated for various times corresponding to the rise and fall of the DP between ~2.8 seconds and 3.6 seconds. Figure 5.27 shows how the ROC curves change with time during this interval with maximal detection probability.

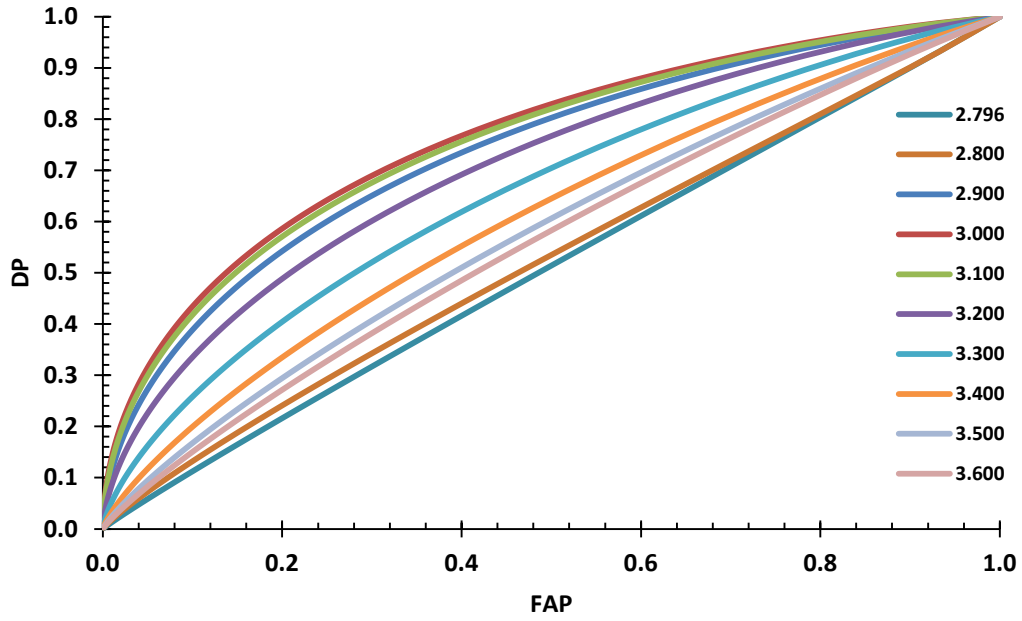

Figure 5.27: ROC curves for various time steps between 2.796 and 3.6 seconds.

The same analysis was done for the alternate shielding configuration, where the inner shield was a 2 cm thick layer of Pb and the outer shield was a 4 cm thick layer of BPE. Figure 5.28 plots the DP for a 1% FAP as a function of time. The behavior of the DP in this configuration is drastically different from that where BPE is on the inside. Because the peak count rate during irradiation is very small (see figure 5.25), the DP rises to less than 2% when the beam is on (shown on a log scale in figure 5.28 for clarity). Shortly after irradiation, the detector count rate beings to increase (see figure 5.24) and the DP jumps to a maximum value of 95.8% and stays at a high DP for a significant time period of about 0.4 seconds before rapidly decaying away as the detector count rate falls to background levels.

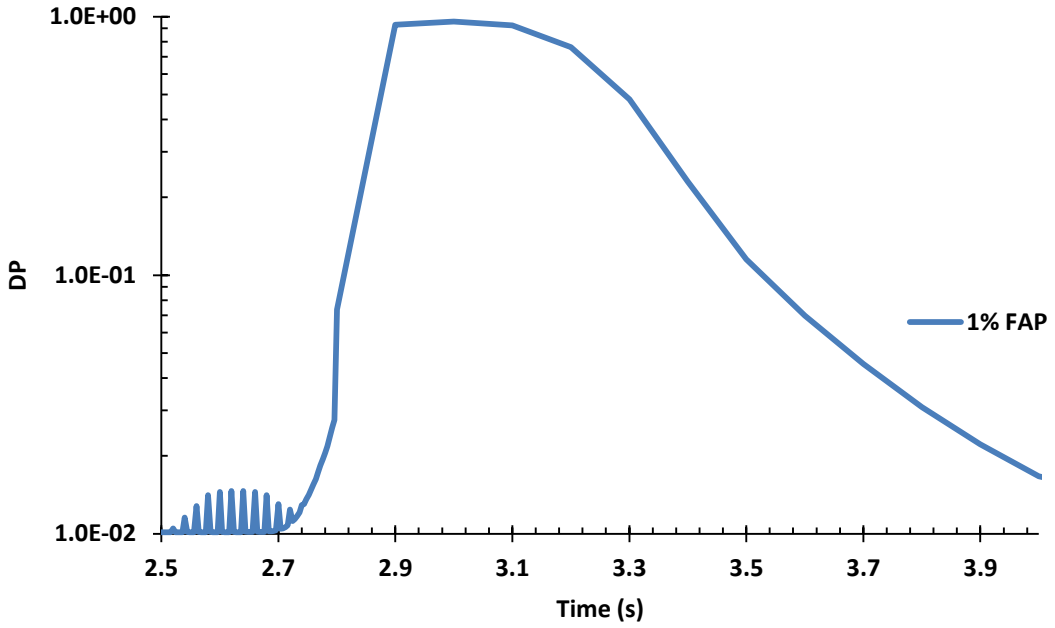

Figure 5.28: Detection probability at various times during and after irradiation of HEU shielded with a 2 cm inner layer of Pb and 4 cm outer layer of BPE.

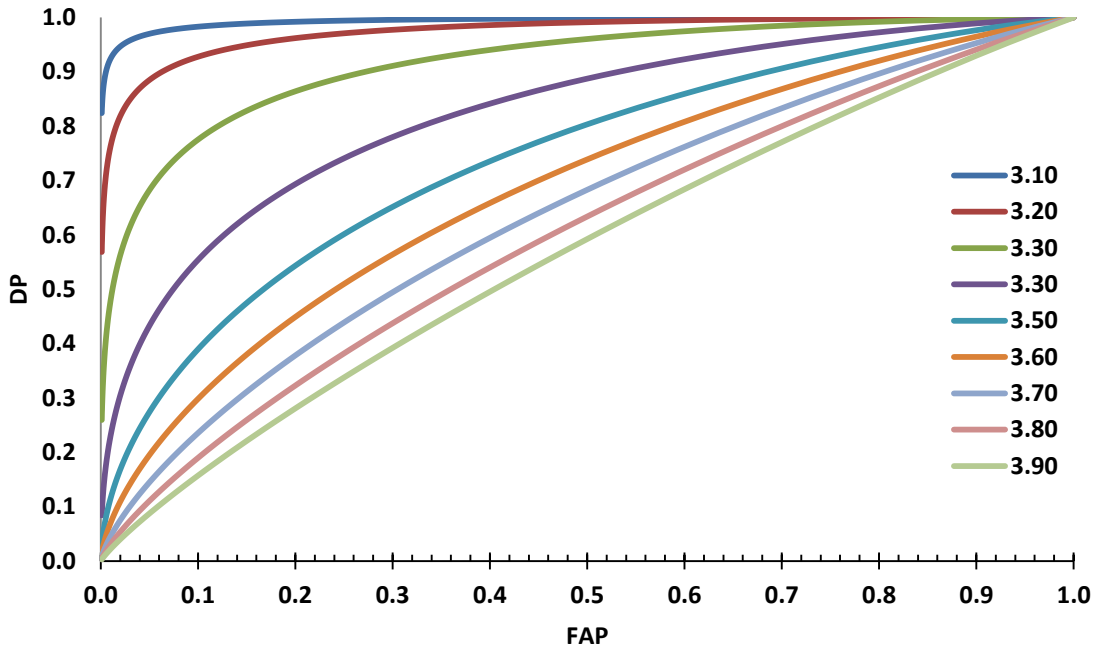

Figure 5.29: ROC curves for various time steps between 3.1 and 3.9 seconds.

Analysis of a large number of shielding configurations including these and other shielding materials can shed light on ways to optimize detection probability. The addition of shielding to SNM seems to increase the DP when compared to the bare case, at least for the shield thicknesses simulated in this work. This seems to be due to the affect of scattering winning out over the absorption and attenuation caused by the shield. As the thickness of the shield is increased, it would be expected that the attenuation will begin to dominate and a net decrease in the DP will be seen. XPASS simulations with larger shielding radii can be used to obtain an estimate of where this transition occurs for various shielding configurations.

Understanding how the shielding affects the neutron count rate can lead to improved detector designs and alarm algorithms. Based upon the behavior shown in this analysis, an algorithm integrates the neutron count rate between pulses and compares that to the value from the previous pulse may be more sensitive than a simple GC algorithm. An algorithm such as this would be able to see the rise and fall of the neutron count rate caused by the thermalization of neutrons within the shield and or bulk cargo, rather than simply looking for a net increase over background. If the period of the decay of the detector signal, taking into account the velocity of the vehicle, matches that of SNM, an alarm can be trigger and the vehicle sent to secondary screening.

Chapter 6

CONCLUSIONS

Simulations of active interrogation scenarios have typically been done by modeling them in massively parallel S_n codes or Monte Carlo codes such as MCNPX. These simulations have historically required long computation times using many cores, even when aggressive techniques to improve convergence are employed. This has limited the ability to do detailed simulations to only those with massive computational resources, with others relying on vastly simplified models which allowed them to model a scenario within a reasonable amount of time.

The XPASS methodology aims to enable practical simulation of active interrogation scenarios utilizing full 3D geometry and transport. Other attempts at reducing the computational burden for simulating AI scenarios have focused primarily on simplifying approximations, such as reducing the problem geometry to a single spatial dimension, to accomplish their goal. XPASS brings the ability to rapidly simulate AI scenarios with results comparable to a full Monte Carlo simulation, but in orders of magnitude less time. The results presented in chapter 5 were all calculated using a single core on a personal laptop in between 20 min to 45 min each. Obtaining a converged solution for of even the simplest of those scenarios was not possible, within practical limits, on a 126 core cluster running MCNPX.

While XPASS does utilize several simplifying approximations, such as a uniformly distributed cargo, these are not a requirement of the method. Since each sub-model is created independently of all others (and coupling between sub-models is handled iteratively and through boundary conditions), the detail within any sub-model can be as fine or course as desired. In addition, as long as the interface conditions remain

unchanged, any sub-model can be refined at a later time to increase the fidelity of its response functions. These refinements can include improved geometric detail or an increase in the number of variables within the space the sub-model spans. For example, if the AI source sub-model is initially a crude model of a linear accelerator that only spans electron energy and target material, refinement can add detail to linear accelerator model as well as allow for variation of the electron beam shape, beam profile (Gaussian, flat top), target thickness, addition of beam filters, and more.

While an increase in the fidelity or addition of other parameterized variables to the sub-model will increase the time needed to generate the response function data library, XPASS runtime is relatively independent of the sub-model complexity. This is because regardless of the complexity of the sub-model, XPASS combines sub-models through a series of matrix multiplications. As the complexity of the sub-model increases, the matrix values become a better representation of the physical reality; but the computational time required to read and multiply the matrices remains unchanged. However, if the number of variables within the threat space over which a sub-model spans is increased, an increase in computational time will be seen as this will result in additional data interpolations to obtain the correct response matrix. Additionally, if the energy group structures are made to be more refined, computational costs will be incurred from interpolating and multiply larger matrices.

The major accomplishment of this work was in developing the implementation of the Greens function methodology specifically to AI scenarios. The response functions for an interrogation scenario span multiple radiation types (electron, photon, and neutron) whose transport physics must be accurately described. A key challenge was the development and determination of appropriate boundary conditions and discretization schemes for each sub-model which captures enough detail to reconstruct an accurate

depiction of the particle transport. A lot of work went into identifying the phase space variables in each sub-model which must be captured explicitly by the response functions versus ones that could well be approximated through assumptions. One major distinction between the sub-models developed for AI as against the sub-models developed for passive system is the directionality of the interrogation beam. This leads to sub-models where symmetry cannot always be assumed.

Development of the ACL method for conserving the total primary photo-neutron production within the SNM was a major contributing factor to maintaining the practicality of the Greens function method for AI systems. Without it, the data generation and data storage requirements for energy and time dependent tallies as a function of beam location and angular distribution on the SNM would make this method intractable. In addition, the development of a database structure that can index the response data was a necessity for managing the file IO of such a large data library. The new system is fully extensible and will allow XPASS's data libraries to significantly expand in size without causing practical issues aside from hard drive space.

There are several applications where XPASS can make an immediate impact on research and development. The first and simplest of these is to use XPASS as a simulation tool to understand the sensitivities of a detector signal to various permutations. This would involve running many scenarios, varying one parameter at a time, and comparing the results against a baseline scenario. Changes in the detector count rate for each permutation can be analyzed to better understand the behavior of a system to changes in a single parameter.

This can be taken a step further by simulating test scenarios where multiple parameters are changed. This would provide additional information on how the detector signal change from a single variable is dependent upon the value of a second variable.

For example, if only the electron source energy was varied, one might determine that an energy of 20 MeV was optimal as it resulted in the largest number of neutrons produced within the SNM. However, if this energy variation is done with multiple cargo types, one might find that this is only true for cargo that have extremely high photo-nuclear thresholds, and that when all possible cargo types are considered, a lower source energy is optimal as it leads to less photo-neutron production within cargo if a material with a low photo-nuclear threshold is present.

Another potential use of XPASS would be to generate detector spectra for many cases, including both threat scenarios and benign, for development of improved alarm algorithms. The spectra can be analyzed to determine features that are indicative of a threat scenario, and an alarm algorithm that triggers on this feature developed. Additional spectra can be generated for training the alarm algorithm as well as for testing purposes.

XPASS can be used as a research and development tool for aiding in design and optimization of AI systems and detector designs. The generic system for which the current XPASS data libraries are generated for can be used to identify desirable features within a commercial design. For example, studied can be done varying the target material to see which material leads to the highest detector count rate when all possible scenarios are considered. One may find that under certain scenarios, one target material will outperform others, while in other scenarios a different material is optimal. Under this case, a linear accelerator design which can swap target material between vehicle interrogations. Pairing vehicle manifests with the target material could lead to an increased detection probability. Similarly, it may be determined that for certain cargo types a low energy beam is optimal, and for other cargo types a high energy beam is optimal. Systems that vary the electron energy for a specific vehicle, based upon the

cargo manifest, could be developed. Or alternatively, a system that modulates the source energy between pulses to cover all scenarios where the cargo manifest may be incorrect or misleading could be optimal.

The ultimate goal would be to use XPASS as alarm tool in AI systems deployed in the field. A vehicle would be interrogated and the time dependent neutron count rate measured with a detector. XPASS would then compute, in real time, compute spectra by sampling the treat space, and determine the region(s) within the threat space the measured spectrum may have originated. If it is determined that there is a high likelihood the measured spectrum originated from a non-benign region, XPASS could trigger an alarm to send the vehicle to secondary inspection. This capability would require additional development, as XPASS would need to be able to computer many spectra in a time frame of several seconds. With parallelization of XPASS, and potentially the implementation of GPU compatibility, this capability could probably be realized.

6.1 FUTURE WORK

As it stands currently, there exists much work to be done to improve the capabilities of XPASS as well as to put it into a form suitable for distribution. As it, XPASS is not suitable for distribution on a large scale, and the most important work would be to migrate the response function database library developed for passive detection into the form used for AI. With this single change, the complete XPASS data library could be compressed and distributed through optical media or download from an approved host site.

The change to the reflection iteration scheme outlined in section 4.7.1 should be applied to the passive mode of XPASS, as it was only implemented for the new AI capability. The method was not implemented for the passive mode as there was not time

to ensure the change would not lead to unintended side effects in other portions of the code. This could happen if certain parts were coded in a way that relies on the methods previously implemented. For example, the variable time stepping (see section 4.7.2) was added to the AI mode of XPASS as a way to reduce the computation time required to get a solution with fine time resolution in the regions of interest. This was implemented as an additional feature after the new AI capability in XPASS was completed. Implementation of the variable time stepping did not simply involve changing the time structure used within XPASS. Certain sub-models were coded in a way that depended on the time structure being fixed and the time bins being of equal width over all time. These assumptions had to each be identified and removed. Simply changing the time structure, without going through the remainder of the code, would have introduced errors based upon the assumptions used when the original code was written.

Finally, addition of several features to XPASS would greatly improve its capabilities. First, the ability for the user to explicitly specify the alarm threshold would give the calculated DP much more meaning and bring the XPASS simulations much closer to what would be done in a deployed system. Currently, XPASS sets the alarm threshold based upon the user specified FAP and the XPASS calculated background. This results in realistic DPs when the background can be relatively well characterized, such as in a passive detection system. For AI, the cosmic and terrestrial, as well as the active background from the source can more or less be characterized from field measurements. However, the active background induced from the vehicle cargo cannot be well characterized and has large variation depending on the cargo type, cargo density, and cargo packing. Setting the threshold based upon the calculated induced active background (as XPASS currently does) is only meaningful when exact knowledge of the cargo contents and distribution is known a priori. Allowing the user to manually specify

the alarm threshold would mimic a real system as it will need to be set at a value which takes into account the variability in the induced active background. XPASS can be used as a tool to determine the variability in the induced AI background by simulating vehicle with a range of cargo types, which can help inform what the threshold value should be set at.

The method XPASS uses to integrate the detector signal for the alarm algorithm should also be modified. As is, the total neutron count sent to the alarm algorithm is obtained by integrating the detector count rate over a single time bin. This is somewhat misleading and unrealistic, as the integration time XPASS uses is dependent upon the width of the time bin. Therefore, since XPASS uses non-uniform time bin widths, the time steps near when the SNM is being irradiated will experience a shorter integration time due to the finer time bins. This is unrealistic as the location of the SNM is unknown to the system operators, and therefore the integration time should be set to a fixed a duration of time, as opposed to a number of time bins. Changing the behavior of XPASS to integrate the detector signal over a fixed time interval will make the alarm algorithm signal integration more realistic.

An improved method for treating the distribution of cargo within the vehicle can be implemented as well. Currently, response functions for a uniformly distributed cargo at a fixed density are required. The density was chosen so that the total mass of the cargo is equal to the maximum amount legally allowed for transport. This leads to unrealistic scenarios where heavy materials, such as steel, take the same density as light materials, such as wood, so that the total mass within the cargo volume is the same. To overcome this, new response functions should be generated where the cargo is uniformly distributed throughout the cargo at the proper density. Reduction in the total cargo mass can be accomplished by automatically increasing the streaming fraction to simulate a loosely

packed cargo (still uniformly distributed), where the total mass is less than or equal to the maximum allowed weight.

APPENDICIES

Appendix A

Group Structures

A.1 Energy Structures

Electron

E1									
[MeV]									
4.20E+00	4.40E+00	4.60E+00	4.80E+00	5.00E+00	5.20E+00	5.40E+00	5.60E+00	5.80E+00	6.00E+00
6.20E+00	6.40E+00	6.60E+00	6.80E+00	7.00E+00	7.20E+00	7.40E+00	7.60E+00	7.80E+00	8.00E+00
8.20E+00	8.40E+00	8.60E+00	8.80E+00	9.00E+00	9.20E+00	9.40E+00	9.60E+00	9.80E+00	1.00E+01
1.02E+01	1.04E+01	1.06E+01	1.08E+01	1.10E+01	1.12E+01	1.14E+01	1.16E+01	1.18E+01	1.20E+01
1.22E+01	1.24E+01	1.26E+01	1.28E+01	1.30E+01	1.32E+01	1.34E+01	1.36E+01	1.38E+01	1.40E+01
1.42E+01	1.44E+01	1.46E+01	1.48E+01	1.50E+01	1.52E+01	1.54E+01	1.56E+01	1.58E+01	1.60E+01
1.62E+01	1.64E+01	1.66E+01	1.68E+01	1.70E+01	1.72E+01	1.74E+01	1.76E+01	1.78E+01	1.80E+01
1.82E+01	1.84E+01	1.86E+01	1.88E+01	1.90E+01	1.92E+01	1.94E+01	1.96E+01	1.98E+01	2.00E+01

Table A.1: Electron energy group structure E1

Photon

P1									
[MeV]									
4.50E+00	5.00E+00	5.50E+00	6.00E+00	6.50E+00	7.00E+00	7.50E+00	8.00E+00	8.50E+00	9.00E+00
9.50E+00	1.00E+01	1.05E+01	1.10E+01	1.15E+01	1.20E+01	1.25E+01	1.30E+01	1.35E+01	1.40E+01
1.45E+01	1.50E+01	1.55E+01	1.60E+01	1.65E+01	1.70E+01	1.75E+01	1.80E+01	1.85E+01	1.90E+01
1.95E+01	2.00E+01								

Table A.2: Photon energy group structure P1

Neutron

N1									
[MeV]									
1.000E-10	1.390E-10	1.932E-10	2.686E-10	3.734E-10	5.191E-10	7.216E-10	1.003E-09	1.395E-09	1.939E-09
2.695E-09	3.746E-09	5.207E-09	7.239E-09	1.006E-08	1.399E-08	1.945E-08	2.703E-08	3.758E-08	5.224E-08
7.261E-08	1.009E-07	1.403E-07	1.951E-07	2.712E-07	3.769E-07	5.240E-07	7.284E-07	1.013E-06	1.408E-06
1.957E-06	2.720E-06	3.781E-06	5.256E-06	7.307E-06	1.016E-05	1.412E-05	1.963E-05	2.729E-05	3.793E-05
5.273E-05	7.330E-05	1.019E-04	1.416E-04	1.969E-04	2.737E-04	3.805E-04	5.289E-04	7.353E-04	1.022E-03
1.421E-03	1.975E-03	2.746E-03	3.817E-03	5.306E-03	7.376E-03	1.025E-02	1.425E-02	1.981E-02	2.754E-02
3.829E-02	5.323E-02	7.399E-02	1.029E-01	1.430E-01	1.988E-01	2.763E-01	3.841E-01	5.339E-01	7.422E-01
1.032E+00	1.434E+00	1.994E+00	2.772E+00	3.853E+00	5.356E+00	7.445E+00	1.035E+01	1.439E+01	2.000E+01

Table A.3: Neutron energy group structure N1

A.2 TIME STRUCTURES

Vehicle

T1
[seconds]
*Variable width The course region is linearly spaced with a user defined bin width equal to the physics parameter *interval*. The fine region is linearly spaced with a bin width equal to the AI parameters $(freq \cdot nFineTime)^{-1}$

Table A.4: Vehicle movement time structure T1

Induced Neutron Emission from Interrogation (prompt + delayed)

T2									
[seconds]									
1.00E-07	1.64E-07	2.68E-07	4.39E-07	7.20E-07	1.18E-06	1.93E-06	3.16E-06	5.18E-06	8.48E-06
1.39E-05	2.28E-05	3.73E-05	6.11E-05	1.00E-04	1.67E-04	2.78E-04	4.64E-04	7.74E-04	1.29E-03
2.15E-03	3.59E-03	5.99E-03	1.00E-02	1.36E-02	1.85E-02	2.51E-02	3.41E-02	4.64E-02	6.31E-02
8.58E-02	1.17E-01	1.58E-01	2.15E-01	2.93E-01	3.98E-01	5.41E-01	7.36E-01	1.00E+00	1.31E+00
1.72E+00	2.26E+00	2.97E+00	3.90E+00	5.12E+00	6.73E+00	8.83E+00	1.16E+01	1.52E+01	2.00E+01

Table A.5: Neutron emission from SNM induced from interrogation time structure T2

Neutron Transport

T3									
[seconds]									
1.00E-12	1.32E-12	1.75E-12	2.31E-12	3.05E-12	4.04E-12	5.34E-12	7.05E-12	9.33E-12	1.23E-11
1.63E-11	2.15E-11	2.85E-11	3.76E-11	4.98E-11	6.58E-11	8.70E-11	1.15E-10	1.52E-10	2.01E-10
2.66E-10	3.51E-10	4.64E-10	6.14E-10	8.11E-10	1.07E-09	1.42E-09	1.87E-09	2.48E-09	3.27E-09
4.33E-09	5.72E-09	7.56E-09	1.00E-08	1.32E-08	1.75E-08	2.31E-08	3.05E-08	4.04E-08	5.34E-08
7.05E-08	9.33E-08	1.23E-07	1.63E-07	2.15E-07	2.85E-07	3.76E-07	4.98E-07	6.58E-07	8.70E-07
1.15E-06	1.52E-06	2.01E-06	2.66E-06	3.51E-06	4.64E-06	6.14E-06	8.11E-06	1.07E-05	1.42E-05
1.87E-05	2.48E-05	3.27E-05	4.33E-05	5.72E-05	7.56E-05	1.00E-04	1.32E-04	1.75E-04	2.31E-04
3.05E-04	4.04E-04	5.34E-04	7.05E-04	9.33E-04	1.23E-03	1.63E-03	2.15E-03	2.85E-03	3.76E-03
4.98E-03	6.58E-03	8.70E-03	1.15E-02	1.52E-02	2.01E-02	2.66E-02	3.51E-02	4.64E-02	6.14E-02
8.11E-02	1.07E-01	1.42E-01	1.87E-01	2.48E-01	3.27E-01	4.33E-01	5.72E-01	7.56E-01	1.00E+00

Table A.6: Neutron transport time structure T3

Appendix B

Active Interrogation Response Functions

Each response function developed in this work for the AI component of XPASS is presented below. The response function name is given on the top, followed by the source energy, destination energy, and time binning structures used for the sub-model.

B.1 AI Source Response Functions

$R_{\gamma\leftarrow e}^{src}$				
E1		P1	N/A	
Variable	**Range**	**Samples**	**s|n**	**Interpolation**
Target Material	W, Pb, Al, Fe	4	s	N/A
Target Thickness	[0.3,2.4] mm	8	n	Linear
Electron Beam Radius	[0.25,1.25] mm	5	n	Linear
Divergence Angle	[0.125,42.1] degrees	23	n	Linear

Table B.1: Response Function $R_{\gamma\leftarrow e}^{src}$

B.2 Cargo Response Functions

$R_{Uncollided}^{cargo}$				
P1		P1	N/A	
Variable	**Range**	**Samples**	**s|n**	**Interpolation**
Depth in Cargo	[1,256] cm	9	n	Logarithmic
Off-Axis Distance from Beamlet Center	[0,30] cm	11	n	Linear
Threat Object Radius	[0.3,20.0] cm	10	n	Linear
Cargo Material	Void, lowz, midz, highz	4	s	N/A

Table B.2: Response Function $R_{Uncollided}^{cargo}$

$R_{Collided}^{cargo}$				
P1		P1	N/A	
Variable	**Range**	**Samples**	**s|n**	**Interpolation**
Depth in Cargo	[1,256] cm	9	n	Logarithmic
Off-Axis Distance from Beamlet Center	[0,30] cm	11	n	Linear
Threat Object Radius	[0.3,20.0] cm	10	n	Linear
Cargo Material	Void, lowz, midz, highz	4	s	N/A

Table B.3: Response Function $R_{Collided}^{cargo}$

R_{p-n}^{cargo}				
P1		N1	N/A	
Variable	**Range**	**Samples**	**s|n**	**Interpolation**
Depth in Cargo	[1,256] cm	9	n	Logarithmic
Off-Axis Distance from Beamlet Center	[0,30] cm	11	n	Linear
Threat Object Radius	[0.3,20.0] cm	10	n	Linear
Cargo Material	Void, lowz, midz, highz	4	s	N/A

Table B.4: Response Function R_{p-n}^{cargo}

B.3 SHIELDING RESPONSE FUNCTIONS

$R_{Uncollided}^{shield}$				
P1		P1	N/A	
Variable	**Range**	**Samples**	**s|n**	**Interpolation**
Inner Radius	[0.5,5.0] cm	10	n	Linear
Outer Radius	[0.7,13.0] cm	10	n	Linear
ssi	[-0.9848, 0.9848] radians	13	n	Linear
Shield Material	lead, bopoly	2	s	N/A

Table B.5: Response Function $R^{shield}_{Uncollided}$

$R^{shield}_{Collided}$				
P1		P1	N/A	
Variable	**Range**	**Samples**	**s|n**	**Interpolation**
Inner Radius	[0.5,5.0] cm	10	n	Linear
Outer Radius	[0.7,13.0] cm	10	n	Linear
xsi	[-0.9848, 0.9848] radians	13	n	Linear
Shield Material	lead, bopoly	2	s	N/A

Table B.6: Response Function $R^{shield}_{Collided}$

$R^{shield}_{(\gamma,n)inner}$				
P1		N1	N/A	
Variable	**Range**	**Samples**	**s|n**	**Interpolation**
Inner Radius	[0.5,5.0] cm	10	n	Linear
Outer Radius	[0.7,13.0] cm	10	n	Linear
Xsi	[-0.9848, 0.9848] radians	13	n	Linear
Shield Material	lead, bopoly	2	s	N/A

Table B.7: Response Function $R^{shield}_{(\gamma,n)inner}$

$R^{shield}_{(\gamma,n)outer}$				
P1		N1	N/A	
Variable	**Range**	**Samples**	**s|n**	**Interpolation**
Inner Radius	[0.5,5.0] cm	10	n	Linear
Outer Radius	[0.7,13.0] cm	10	n	Linear
Xsi	[-0.9848, 0.9848] radians	13	n	Linear
Shield Material	lead, bopoly	2	s	N/A

Table B.8: Response Function $R^{shield}_{(\gamma,n)outer}$

B.4 SNM RESPONSE FUNCTIONS

$R^{SNM}_{nProduction}$				
P1		N1	N/A	
Variable	**Range**	**Samples**	**s|n**	**Interpolation**
SNM Type	du, heu, vheu, wgpu, rgpu	5	s	N/A
SNM Radius	[0.1,5.0] cm	23	n	Linear

Table B.9: Response Function $R^{SNM}_{nProduction}$

$R^{SNM}_{nLeakage}$				
N1		N1	T2	
Variable	**Range**	**Samples**	**s|n**	**Interpolation**
SNM Type	du, heu, vheu, wgpu, rgpu	5	s	N/A
SNM Radius	[0.1,5.0] cm	23	n	Linear
Xsi	[-0.9236, 0.9236] radians	21	n	Linear

Table B.10: Response Function $R^{SNM}_{nLeakage}$

B.5 AI BACKGROUND RESPONSE FUNCTIONS

$R^{Bg}_{Induced}$				
P1		N1	N/A	
Variable	**Range**	**Samples**	**s|n**	**Interpolation**
Cargo Material	void, lowz, midz, highz	4	s	N/A

Table B.11: Response Function $R^{Bg}_{Induced}$

Appendix C

Response Function MCNPX Templates

MCNPX (version 2.70) template decks used for generating the response function data are given below. The template decks have flags for each variable over which the response function spans. An input deck generator was developed which replaces each flag in the MCNPX template deck with a specified value for each variable. The input deck generator create an MCNPX deck for all combination of variable values given in the input generator deck.

Note: \ indicates the current line is continued on the next line (added here for viewing purposes)

C.1 AI Source Response Function Generation

MCNPX Template

```
Source Sub-Model
c Cell Cards
c ==========
997  0  (-999 998)  $ vacuum
998  1  -%(MAT.density) (-998)  $ target
999  0  (999)  $ outside world

c Surface Cards
c =============
1  CZ  0.34906 $ 0.25 degree
2  CZ  0.69814 $ 0.5 degree
3  CZ  1.04724 $ 0.75 degree
4  CZ  1.74551 $ 1 degree
5  CZ  3.49208 $ 2 degree
6  CZ  5.24078 $ 3 degree
7  CZ  6.99268 $ 4 degree
8  CZ  8.74887 $ 5 degree
9  CZ  10.5104 $ 6 degree
10 CZ  12.2785 $ 7 degree
11 CZ  14.0541 $ 8 degree
12 CZ  15.8384 $ 9 degree
13 CZ  17.6327 $ 10 degree
14 CZ  21.2557 $ 12 degree
15 CZ  24.9328 $ 14 degree
16 CZ  28.6745 $ 16 degree
17 CZ  32.4920 $ 18 degree
18 CZ  36.3970 $ 20 degree
19 CZ  46.6308 $ 25 degree
20 CZ  57.7350 $ 30 degree
```

```
21 CZ  70.0021 $ 35 degree
22 CZ  83.9100 $ 40 degree
23 CZ  100.000 $ 45 degree
998 RPP  -7.2 7.2  -7.2 7.2  -%(TRGT.thickness) 0  $ target
999 RCC  0 0 -1.0  0 0 101  325  $ problem bounds

c Data Cards
c ==========
%(MAT.isos)
MODE n p e
LCA 8j 1 1
PHYS:p 4j 0
PHYS:e 5j 25 25
CUT:e j 0.25 $ kill electrons below 250keV
ACT DG=mg
SDEF X=D1 Y=D2 Z=-0.5 AXS=0 0 1 VEC=0 0 1
     DIR=1 EXT=0 PAR=e ERG=D3
SP1 -41 %(EBEAM.rad)
SP2 -41 %(EBEAM.rad)
SI3 4 79i 20
SP3 0 1 79R
F11:p  999.2
c fs card to segment tally based upon off-axis angle
FS11 -1 -2 -3 -4
     -5 -6 -7 -8
     -9 -10 -11 -12
     -13 -14 -15 -16 -17
     -18 -19 -20 -21 -22 -23
c sd card to divide each segment by the area of the tally region (ring)
SD11
     1.963E-01 5.890E-01 9.817E-01 1.374E+00
     9.425E+00 1.571E+01 2.199E+01 2.827E+01
     3.456E+01 4.084E+01 4.712E+01 5.341E+01
     5.969E+01 1.382E+02 1.634E+02 1.885E+02 2.136E+02
     2.388E+02 7.069E+02 8.639E+02 1.021E+03 1.178E+03 1.335E+03
     1
FM11 80
FT11 scx 3
E11 4 31i 20  $ photon energy structure
PRINT
NPS 1E7
PRDMP 1E7 1E7 1 1 1E7
BBREM 1.  1. 46i 10. 1
IMP:n,p,e  1 1 0
```

Input Generator Deck

```
3
%(MAT) 4s|W,Pb,Al,Fe
.density:1
19.25
11.34
```

```
2.700
7.874
.isos:1
M1  74000 1  $ W - tungsten (19.25 g/cm^3)
M1  82000 1  $ Pb - lead (11.34 g/cm^3)
M1  13000 1  $ Al - aluminum (2.70 g/cm^3)
M1  26000 1  $ Fe - iron (7.874 g/cm^3)

%(TRGT) 8n|0.03,0.06,0.09,0.12,0.15,0.18,0.21,0.24
.thickness:1
0.03
0.06
0.09
0.12
0.15
0.18
0.21
0.24

%(EBEAM) 5n|0.025,0.050,0.075,0.100,0.125
.rad:1
0.025
0.050
0.075
0.100
0.125
```

C.2 CARGO RESPONSE FUNCTION GENERATION

MCNPX Template

```
Cargo Sub-Model
c Cell Cards
c ==========
1   0        -1   $ Threat Object
101 %(MAT.dens)    101 -102 1  $ Infinite Caro
999 0        -101:102  $ outside world

c Surface Cards
c =============
1   SPH  %(DEPTH.x) 0 %(OFFAXIS.z)  %(RADIUS.r)  $ Threat Object
101 PX   0    $ infinite cargo
102 PX   260  $ infinite cargo

c Data Cards
c ==========
%(MAT.isos)
MODE n p
PHYS:p 3j 1 0
LCA 8j 1 1
SDEF PAR=p  ERG=D1  X=0 Y=D2 Z=D3  SUR=101  VEC=1 0 0  DIR=1
SI1 %(ERG.e)
```

```
SP1 0 1
SI2  -1.25 1.25
SP2  0 1
SI3  -1.25 1.25
SP3  0 1
F11:p 1
FT11 tag 1
FU11 -1 1e10 NT
E11 4.0 31i 20 $ photon energy structure
F21:n 1
E21 1E-10 78iLog 20 $ neutron energy structure
PRINT
NPS 1E5
SPABI:n np 20 4
IMP:n,p  0 1 0
```

Input Generator Deck

```
5
%(DEPTH) 9n|1,2,4,8,16,32,64,128,256
.x:1
1
2
4
8
16
32
64
128
256

%(OFFAXIS) 11n|0,1,2,3,5,8,12,16,20,25,30
.z:1
0
1
2
3
5
8
12
16
20
25
30

%(RADIUS) 10n|0.3,0.8,1.5,2.2,3.0,3.9,4.8,8.0,13.0,20.0
.r:1
0.3
0.8
1.5
2.2
3.0
```

```
3.9
4.8
8.0
13.0
20.0

%(MAT) 4s|void,lowz,midz,highz
.dens:1
0
1 -0.2
1 -0.2
1 -0.2
.isos:7
c   $ void
c
c
c
c
c
c
m1  $ low-z Wood
          1001 -5.789e-02 $ hydrogen-1
          6000 -4.800e-01 $ carbon-natural
          8016 -4.600e-01 $ oxygen-natural
c
c
c
m1  $ mid-z Clay
      8016 -0.524858
      13027 -0.005227
      14000 -0.449011
      20000 -0.014419
      26000 -0.007213
c
m1  $ high-z Structural Steel
         14000 -1.012e-02 $ silicon-natural
         24000 -1.693e-01 $ chromium-natural
         25055 -1.996e-02 $ manganese-natural
         26000 -6.550e-01 $ iron-natural
         28000 -1.204e-01 $ nickel-natural
         42000 -2.514e-02 $ molybdenum-natural

%(ERG) 33n|4.0,4.5,5.0,5.5,6.0,6.5,7.0,7.5,8.0,8.5,9.0,9.5,10.0,10.5,\
11.0,11.5,12.0,12.5,13.0,13.5,14.0,14.5,15.0,15.5,16.0,16.5,17.0,17.5,\
18.0,18.5,19.0,19.5,20.0
.e:1
0.0 4.0
4.0 4.5
4.5 5.0
5.0 5.5
5.5 6.0
6.0 6.5
6.5 7.0
```

```
7.0 7.5
7.5 8.0
8.0 8.5
8.5 9.0
9.0 9.5
9.5 10.0
10.0 10.5
10.5 11.0
11.0 11.5
11.5 12.0
12.0 12.5
12.5 13.0
13.0 13.5
13.5 14.0
14.0 14.5
14.5 15.0
15.0 15.5
15.5 16.0
16.0 16.5
16.5 17.0
17.0 17.5
17.5 18.0
18.0 18.5
18.5 19.0
19.0 19.5
19.5 20.0
```

C.3 SHIELDING RESPONSE FUNCTION GENERATION

MCNPX WWG Template

```
Shielding Sub-Model WW-Generator
c Cell Cards
c ==========
1   0         -101      $ void
2   1 %(MAT.dens)  -102 101  $ shield
3   0         -999 102  $ vacuum
999 0          999      $ outside world

c Surface Cards
c =============
101 SPH  0 0 0  %(IRAD.r)   $ inner radius
102 SPH  0 0 0  %(ORAD.r)   $ outter radius
999 SPH  0 0 0  90   $ bounds

c Data Cards
c ==========
%(MAT.isos)
MODE n p
CUT:n 2j 0 0
PHYS:p 3j 1 0
LCA 8j 1 1
```

```
sdef PAR=p  ERG=D1  X=D2 Y=D3 Z=-51
     DIR=1  VEC=0 0 1 ARA=1
SI1 %(ERG.e)
SP1 0 1
SI2 -%(ORAD.r) %(SIN_XSI.angle)
SP2 0 1
SI3 -%(ORAD.r) %(ORAD.r)
SP3 0 1
F15:p  0 0 0  0
WWG 15 0 0
MESH  GEOM=sph  REF=0 0 -51  ORIGIN=0 0 0
     IMESH %(ORAD.r) 100   IINTS 25 1
     JMESH 0.5      JINTS 1
     KMESH 1.0      KINTS 1
PRINT
NPS 1E5
PRDMP 1E5 1E5 1 1 1E5
IMP:n,p  1 1 1 0
```

MCNPX Template

```
Shielding Sub-Model
c Cell Cards
c ==========
1   0         -101      $ void
2   1 %(MAT.dens)  -102 101  $ shield
3   0         -999 102  $ vacuum
999 0          999      $ outside world

c Surface Cards
c =============
101 SPH  0 0 0  %(IRAD.r)   $ inner radius
102 SPH  0 0 0  %(ORAD.r)   $ outter radius
999 SPH  0 0 0  90   $ bounds

c Data Cards
c ==========
%(MAT.isos)
MODE n p
CUT:n 2j 0 0
PHYS:p 3j 1 0
LCA 8j 1 1
sdef PAR=p  ERG=D1  X=D2 Y=D3 Z=-51
     DIR=1  VEC=0 0 1
SI1 %(ERG.e)
SP1 0 1
SI2 -%(ORAD.r) %(SIN_XSI.angle)
SP2 0 1
SI3 -%(ORAD.r) %(ORAD.r)
SP3 0 1
F11:p 101
FT11 tag 1
```

```
FU11 -1 1e10 NT
E11 4.0 31i 20
F21:n 101
E21 1E-10 78iLog 20
F31:n 102
E31 1E-10 78iLog 20
WWP:p 4j -1
PRINT
NPS 1E6
PRDMP 1E6 1E6 1 1 1E6
SPABI:n np 20 4
IMP:n,p  0 1 1 0
```

Input Generator Deck

```
5
%(IRAD) 10n|0.5,0.8,1.2,1.8,2.2,2.5,3.0,3.5,4.0,5.0
.r:1
0.5
0.8
1.2
1.8
2.2
2.5
3.0
3.5
4.0
5.0

%(ORAD) 10n|0.7,1.4,2.3,3.2,4.5,5.7,7.0,8.5,10.5,13
.r:1
0.7
1.4
2.3
3.2
4.5
5.7
7.0
8.5
10.5
13

%(SIN_XSI) 13n|-0.9848,-0.7660,-0.5000,-0.3420,-0.1736,-0.0872,0.0000,\
0.0872,0.1736,0.3420,0.5000,0.7660,0.9848
.angle:1
SIN_XSI
SIN_XSI
SIN_XSI
SIN_XSI
SIN_XSI
SIN_XSI
SIN_XSI
SIN_XSI
```

```
SIN_XSI
SIN_XSI
SIN_XSI
SIN_XSI
SIN_XSI

%(MAT) 2s|lead,bopoly
.dens:1
-11.34
-1.030
.isos:4
M1   $ natural lead
     82000 1
c
c
M1   $ borated polyethylene
     1001 0.627759
     5000 0.046690
     6000 0.325552

%(ERG) 33n|4.0,4.5,5.0,5.5,6.0,6.5,7.0,7.5,8.0,8.5,9.0,9.5,10.0,10.5,\
11.0,11.5,12.0,12.5,13.0,13.5,14.0,14.5,15.0,15.5,16.0,16.5,17.0,17.5,\
18.0,18.5,19.0,19.5,20.0
.e:1
0.0 4.0
4.0 4.5
4.5 5.0
5.0 5.5
5.5 6.0
6.0 6.5
6.5 7.0
7.0 7.5
7.5 8.0
8.0 8.5
8.5 9.0
9.0 9.5
9.5 10.0
10.0 10.5
10.5 11.0
11.0 11.5
11.5 12.0
12.0 12.5
12.5 13.0
13.0 13.5
13.5 14.0
14.0 14.5
14.5 15.0
15.0 15.5
15.5 16.0
16.0 16.5
16.5 17.0
17.0 17.5
17.5 18.0
```

```
18.0 18.5
18.5 19.0
19.0 19.5
19.5 20.0
```

C.4 SNM RESPONSE FUNCTION GENERATION

MCNPX Template: nProduction

```
SNM Sub-Model: Neutron Production
c Cell Cards
c ==========
1   1 -%(MAT.density)  -101      $ SNM
3   0         -999 101  $ vacuum
999 0          999      $ outside world

c Surface Cards
c =============
101 SPH  0 0 0  %(RAD.radius)    $ SNM
999 SPH  0 0 0  50      $ bounds

c Data Cards
c ==========
%(MAT.isos)
MODE n p
CUT:n 2j 0 0
PHYS:p 3j 1 0
LCA 8j 1 1
SDEF PAR=p  ERG=D1  SUR=101  DIR=D2
SI1 0 4 31i 20
SP1 0 1 32R
SI2 H -1 0
SP2 -21 1
F11:n 101
FT11 SCX 1
FM11 33
E11 1E-10 78iLOG 20
PRINT
NPS 1E7
PRDMP 1E7 1E7 1 1 1E7
IMP:n,p 1 1 0
```

Input Generator Deck

```
2
%(MAT) 5s|du,heu,vheu,wgpu,rgpu
.density:1
18.95
18.95
18.95
15.75
```

```
15.75
.isos:6
M1  $ DU (18.95 g/cm^3)
     92234 -0.001
     92235 -0.2
     92238 -99.799
MX1:n  $ Al-27 is transparent to neutrons
     13027  13027  13027
M1  $ HEU (18.95 g/cm^3)
     92232 -3E-8  92234 -0.70
     92235 -90.3  92236 -0.30
     92238 -8.70
MX1:n  $ Al-27 is transparent to neutrons
     13027  13027  13027  13027  13027
M1  $ VHEU (18.95 g/cm^3)
     92234 -0.70  92235 -90.3
     92236 -0.30  92238 -8.70
MX1:n  $ Al-27 is transparent to neutrons
     13027  13027
     13027  13027
M1  $ WGPu (15.75 g/cm^3)
     94236 -5E-9   94238 -1.5E-2
     94239 -93.63  94240 -6.00
     94241 -0.355
MX1:n $ Al-27 is transparent to neutrons
     13027  13027  13027  13027  13027
M1  $ RGPu (15.75 g/cm^3)
     94236 -3E-8  94238 -1.2
     94239 -59.0  94240 -24.0
     94241 -11.8  94242 -4.00
MX1:n $ Al-27 is transparent to neutrons
     13027  13027  13027  13027  13027  13027

%(RAD) 23n|0.10,0.20,0.30,0.40,0.50,0.60,0.70,0.80,0.90,1.00,1.20,\
1.40,1.60,1.80,2.00,2.25,2.50,2.75,3.00,3.50,4.00,4.50,5.00
.radius:1
0.10
0.20
0.30
0.40
0.50
0.60
0.70
0.80
0.90
1.00
1.20
1.40
1.60
1.80
2.00
2.25
2.50
```

```
2.75
3.00
3.50
4.00
4.50
5.00
```

MCNPX Template: nLeakage

```
SNM Submodel: Neutron Leakage
c Cell Cards
c ==========
1   1 -%(MAT.density)  -101      $ SNM
2   0         -999 101  $ vacuum
999 0          999      $ outside world

c Surface Cards
c =============
101 SPH  0 0 0  %(RAD.rad)      $ SNM
999 SPH  0 0 0  50      $ bounds

c Data Cards
c ==========
%(MAT.isos)
MODE n p
CUT:n 2j 0 0
PHYS:p 3j 1 0
LCA 8j 1 1
SDEF PAR=n ERG=D1 X=D2 Y=D3 Z=D4 CEL=1
SI1 H 0 1E-10 78iLOG 20
SP1 D 0 1 79R
SI2 -%(RAD.rad) %(RAD.rad)
SP2 0 1
SI3 -%(RAD.rad) %(RAD.rad)
SP3 0 1
SI4 -%(RAD.rad) %(SIN_XSI.angle)
SP4 0 1
F11:n 101
FM11 80
FT11 SCX 1
E11 1E-10 78iLOG 20
T11 1E1 13iLOG 1E4 8iLOG 1E6 14iLOG 1E8 10iLOG 2E9 NT
PRINT
NPS 1E7
IMP:n,p 1 1 0
```

Input Generator Deck

```
3
%(MAT) 5s|du,heu,vheu,wgpu,rgpu
.density:1
18.95
```

```
18.95
18.95
15.75
15.75
.isos:4
M1  $ DU (18.95 g/cm^3)
     92234 -0.001
     92235 -0.2
     92238 -99.799
M1  $ HEU (18.95 g/cm^3)
     92232 -3E-8  92234 -0.70
     92235 -90.3  92236 -0.30
     92238 -8.70
M1  $ VHEU (18.95 g/cm^3)
     92234 -0.70  92235 -90.3
     92236 -0.30  92238 -8.70
c
M1  $ WGPu (15.75 g/cm^3)
     94236 -5E-9   94238 -1.5E-2
     94239 -93.63  94240 -6.00
     94241 -0.355
M1  $ RGPu (15.75 g/cm^3)
     94236 -3E-8  94238 -1.2
     94239 -59.0  94240 -24.0
     94241 -11.8  94242 -4.00

%(RAD) 27n|0.10,0.20,0.30,0.40,0.50,0.60,0.70,0.80,0.90,1.00,1.20,\
1.40,1.60,1.80,2.00,2.25,2.50,2.75,3.00,3.25,3.50,3.75,4.00,4.25,4.50,\
4.75,5.00
.rad:1
0.10
0.20
0.30
0.40
0.50
0.60
0.70
0.80
0.90
1.00
1.20
1.40
1.60
1.80
2.00
2.25
2.50
2.75
3.00
3.25
3.50
3.75
4.00
```

```
4.25
4.50
4.75
5.00

%(SIN_XSI) 21n|-0.9236,-0.8660,-0.7660,-0.6428,-0.5000,-0.3420,\
-0.1736,-0.1219,-0.0872,-0.0349,0.0000,0.0349,0.0872,0.1219,0.1736,\
0.3420,0.5000,0.6428,0.7660,0.8660,0.9236
.angle:1
SIN_XSI
SIN_XSI
SIN_XSI
SIN_XSI
SIN_XSI
SIN_XSI
SIN_XSI
SIN_XSI
SIN_XSI
SIN_XSI
SIN_XSI
SIN_XSI
SIN_XSI
SIN_XSI
SIN_XSI
SIN_XSI
SIN_XSI
SIN_XSI
SIN_XSI
SIN_XSI
SIN_XSI
```

C.5 AI BACKGROUND RESPONSE FUNCTION GENERATION

MCNPX Template

```
MESSAGE: FATAL

Cargo Sub-Model
c Cell Cards
c ==========
1   %(MAT.dens)    -1
2   %(MAT.dens)    -2
3   %(MAT.dens)    -3
4   %(MAT.dens)    -4
5   %(MAT.dens)    -5
6   %(MAT.dens)    -6
7   %(MAT.dens)    -7
8   %(MAT.dens)    -8
101 %(MAT.dens)    101 -102  1 2 3 4 5 6 7 8  $ Infinite Caro
999 0        -101:102  $ outside world
```

```
c Surface Cards
c =============
1   SX    2  1
2   SX    4  1
3   SX    8  1
4   SX   16  1
5   SX   32  1
6   SX   64  1
7   SX  128  1
8   SX  256  1
101 PX    0      $ infinite cargo
102 PX  260      $ infinite cargo

c Data Cards
c ==========
%(MAT.isos)
MODE n p
PHYS:n 3j 10
CUT:n 2j -0.75 -0.005
PHYS:p 3j 1 0
LCA 8j 1 1
SDEF PAR=p  ERG=D1  X=0 Y=D2 Z=D3  SUR=101  VEC=1 0 0  DIR=1
SI1 0 4.0 31i 20
SP1 0 1 32r
SI2  -1.25 1.25
SP2  0 1
SI3  -1.25 1.25
SP3  0 1
F11:n  1
FT11 scx 1
FM11 206.25  $ multiply by number of source energy groups and source\
area
c FM11 33
SD11 4.18879 $ volume of sphere = 4pi/3
F21:n  2
FT21 scx 1
FM21 206.25  $ multiply by number of source energy groups and source\
area
c FM21 33
SD21 4.18879 $ volume of sphere = 4pi/3
F31:n  3
FT31 scx 1
FM31 206.25  $ multiply by number of source energy groups and source\
area
c FM31 33
SD31 4.18879 $ volume of sphere = 4pi/3
F41:n  4
FT41 scx 1
FM41 206.25  $ multiply by number of source energy groups and source\
area
c FM41 33
SD41 4.18879 $ volume of sphere = 4pi/3
F51:n  5
```

```
FT51 scx 1
FM51 206.25  $ multiply by number of source energy groups and source\
area
c FM51 33
SD51 4.18879 $ volume of sphere = 4pi/3
F61:n  6
FT61 scx 1
FM61 206.25  $ multiply by number of source energy groups and source\
area
c FM61 33
SD61 4.18879 $ volume of sphere = 4pi/3
F71:n  7
FT71 scx 1
FM71 206.25  $ multiply by number of source energy groups and source\
area
c FM71 33
SD71 4.18879 $ volume of sphere = 4pi/3
F81:n  8
FT81 scx 1
FM81 206.25  $ multiply by number of source energy groups and source\
area
c FM81 33
SD81 4.18879 $ volume of sphere = 4pi/3
E0 1E-10 78iLog 20 $ neutron energy structure
PRINT
NPS 1E8
PRDMP 1E8 1E8 2j 1E8
IMP:p  1 8r 0
IMP:n  1 7r 0 0
```

Input Generator Deck

```
1
%(MAT) 4s|void,lowz,midz,highz
.dens:1
0
1 -0.2
1 -0.2
1 -0.2
.isos:8
c   $ void
c
c
c
c
c
c
c
m1  $ low-z Wood
     1001 -5.789e-02 $ hydrogen-1
     6000 -4.800e-01 $ carbon-natural
     8016 -4.600e-01 $ oxygen-natural
```

```
     pnlib=70u
c
c
c
m1  $ mid-z Clay
     8016 -0.524858
     13027 -0.005227
     14000 -0.449011
     20000 -0.014419
     26000 -0.007213
     pnlib=70u
c
m1  $ high-z Structural Steel
     14000 -1.012e-02 $ silicon-natural
     24000 -1.693e-01 $ chromium-natural
     25055 -1.996e-02 $ manganese-natural
     26000 -6.550e-01 $ iron-natural
     28000 -1.204e-01 $ nickel-natural
     42000 -2.514e-02 $ molybdenum-natural
     pnlib=70u
```

Appendix D

Benchmarks and Applications XPASS Input Files

D.1 BENCHMARKS

Case 1: Single pulse of 10 MeV photons on 5.3 kg of HEU, 2.8 kg of WGPu (WGPu)

```
#
#    XPASS Threat Scenario Modeling Software
#

#
# PHYSICS
#
physics
      photon on
      neutron on
      fissgamma off
      mactime on
      ergfac 1
      refeps 1e-4
      sigmaeff 0.0
      interval 0.1
      background off

#
# SOURCE
#
source
      snm 0
            type wgpu
            mass 2800
            iso
                  pu236 5e-9
                  pu238 0.015
                  pu239 93.63
                  pu240 6.0
                  pu241 0.355
            posx 120
            posy 750
            posz 100

#
# VEHICLE
#
vehicle
      truck
            cargo
                  void 1
            stream 0.0
```

```
            velocity 8.05

#
# ACTIVE INTERROGATION
#
AI
      electrons
            10.0 1
      current 6
      sx 20.0
      sy 0
      sz 100
      target W
      thickness 1.5
      erad 1
      pulsew 4
      freq 5
      nFineTime 200
      BW 35
      FBH 1.0
      bg
            0 1.67

#
# BACKGROUND RADIATION
#
background
      photon
            usoil 36
            uconc 46
            thsoil 44
            thconc 21
            ksoil 85
            kconc 23.7
      neutron
            lat 0
            long 0
            smod 0.5
            elev 0

#
# DETECTORS
#
detection
      he3
            posx 198.1
            posy 0
            posz 100
            height 117
            modrad 3.8
            refrad 0.0
            actwidth 52
            eff 1.0
```

```
            fanofac 1.0
            alarm
                  gc
                        nint 1
```

Case 2: Single pulse of 10 MeV photons on 22 kg of HEU

```
#
#    XPASS Threat Scenario Modeling Software
#

#
# PHYSICS
#
physics
      photon on
      neutron on
      fissgamma off
      mactime on
      ergfac 1
      refeps 1e-4
      sigmaeff 0.0
      interval 0.1
      background off

#
# SOURCE
#
source
      snm 0
            type heu
            mass 22000
            iso
                  u234 0.70
                  u235 90.3
                  u236 0.3
                  u238 8.7
            posx 48.1
            posy 700
            posz 100

#
# VEHICLE
#
vehicle
      truck
            cargo
                  void 1
            stream 0.0
            velocity 8.05

#
```

```
# ACTIVE INTERROGATION
#
AI
      electrons
            10.0 1
      current 38
      sx 748.1
      sy 0
      sz 100
      target W
      thickness 1.5
      erad 1
      pulsew 6
      freq 5
      nFineTime 150
      BW 35
      FBH 1.0
      bg
            0 23

#
# BACKGROUND RADIATION
#
background
      photon
            usoil 36
            uconc 46
            thsoil 44
            thconc 21
            ksoil 85
            kconc 23.7
      neutron
            lat 0
            long 0
            smod 0.5
            elev 0

#
# DETECTORS
#
detection
      he3
            posx 198.1
            posy 0
            posz 100
            height 182.88
            modrad 3.8
            refrad 0.0
            actwidth 52
            eff 1.0
            fanofac 1.0
            alarm
                  gc
```

```
                        nint 1
```

Case 3: Count Rate Attenuation with Lead Shielding (5.08 cm Pb)

```
#
#    XPASS Threat Scenario Modeling Software
#

#
# PHYSICS
#
physics
      photon on
      neutron on
      fissgamma off
      mactime on
      ergfac 1
      refeps 1e-4
      sigmaeff 0.0
      interval 0.2
      background off

#
# SOURCE
#
source
      snm 0
            type heu
            mass 22500
            iso
                  u234 0.70
                  u235 90.3
                  u236 0.3
                  u238 8.7
            posx 18.1
            posy 750
            posz 100
            shield
                  layer
                        type lead
                        thick 5.08
                        stream 0

#
# VEHICLE
#
vehicle
      truck
            cargo
                  void 1
            stream 0.0
            velocity 8.05
```

```
#
# ACTIVE INTERROGATION
#
AI
      electrons
            10.0 1
      current 38
      sx -215.9
      sy 0
      sz 100
      target W
      thickness 1.5
      erad 1
      pulsew 6
      freq 5
      nFineTime 50
      BW 35
      FBH 1.0
      bg
            0 50

#
# BACKGROUND RADIATION
#
background
      photon
            usoil 36
            uconc 46
            thsoil 44
            thconc 21
            ksoil 85
            kconc 23.7
      neutron
            lat 0
            long 0
            smod 0.5
            elev 0

#
# DETECTORS
#
detection
      he3
            posx 198.1
            posy 0
            posz 100
            height 182.88
            modrad 3.8
            refrad 0.0
            actwidth 52
            eff 1.0
            fanofac 1.0
```

D.2 APPLICATIONS

Detector Signal vs. SNM Location in Cargo (325 cm)

```
#
#    XPASS Threat Scenario Modeling Software
#

#
# PHYSICS
#
physics
      photon on
      neutron on
      fissgamma off
      mactime on
      ergfac 1
      refeps 1e-4
      sigmaeff 0.0
      interval 0.1
      background off

#
# SOURCE
#
source
      snm 0
            type heu
            mass 5300
            iso
                  u232 3e-8
                  u234 2.0
                  u235 85
                  u236 1.0
                  u238 12
            posx 0
            posy 325
            posz 100

#
# VEHICLE
#
vehicle
      truck
            cargo
                  highz 1
            stream 0.0
            velocity 8.05

#
# ACTIVE INTERROGATION
#
AI
```

```
      electrons
            10.0 1
      current 6
      sx 20.0
      sy 0
      sz 100
      target W
      thickness 1.5
      erad 1
      pulsew 4
      freq 10
      nFineTime 1
      BW 45
      FBH 1.0

#
# BACKGROUND RADIATION
#
background
      photon
            usoil 36
            uconc 46
            thsoil 44
            thconc 21
            ksoil 85
            kconc 23.7
      neutron
            lat 0
            long 0
            smod 0.5
            elev 0

#
# DETECTORS
#
detection
      he3
            posx 198.1
            posy 0
            posz 100
            height 70
            modrad 3.8
            refrad 0.0
            actwidth 52
            eff 1.0
            fanofac 1.0
```

Detector Signal vs. Vehicle Velocity (5.0 mph)

```
#
#    XPASS Threat Scenario Modeling Software
#
```

```
#
# PHYSICS
#
physics
      photon on
      neutron on
      fissgamma off
      mactime on
      ergfac 1
      refeps 1e-4
      sigmaeff 0.0
      interval 0.1
      background off

#
# SOURCE
#
source
      snm 0
            type heu
            mass 5300
            iso
                  u232 3e-8
                  u234 2.0
                  u235 85
                  u236 1.0
                  u238 12
            posx 120
            posy 750
            posz 100

#
# VEHICLE
#
vehicle
      truck
            cargo
                  void 1
            stream 0.0
            velocity 5.0

#
# ACTIVE INTERROGATION
#
AI
      electrons
            10.0 1
      current 6
      sx 20.0
      sy 0
      sz 100
      target W
```

```
      thickness 1.5
      erad 1
      pulsew 4
      freq 10
      nFineTime 1
      BW 45
      FBH 1.0

#
# BACKGROUND RADIATION
#
background
      photon
            usoil 36
            uconc 46
            thsoil 44
            thconc 21
            ksoil 85
            kconc 23.7
      neutron
            lat 0
            long 0
            smod 0.5
            elev 0

#
# DETECTORS
#
detection
      he3
            posx 198.1
            posy 0
            posz 100
            height 70
            modrad 3.8
            refrad 0.0
            actwidth 52
            eff 1.0
            fanofac 1.0
```

Deployed Systems Comparable to Benchmark Cases 1 and 2 (Case 2)

```
#
#    XPASS Threat Scenario Modeling Software
#

#
# PHYSICS
#
physics
      photon on
      neutron on
```

```
      fissgamma off
      mactime on
      ergfac 1
      refeps 1e-4
      sigmaeff 0.0
      interval 0.1
      background off

#
# SOURCE
#
source
      snm 0
            type heu
            mass 22500
            iso
                  u234 0.70
                  u235 90.3
                  u236 0.3
                  u238 8.7
            posx 48.1
            posy 700
            posz 100

#
# VEHICLE
#
vehicle
      truck
            cargo
                  void 1
            stream 0.0
            velocity 8.05

#
# ACTIVE INTERROGATION
#
AI
      electrons
            10.0 1
      current 38
      sx 748.1
      sy 0
      sz 100
      target W
      thickness 1.5
      erad 1
      pulsew 6
      freq 50
      nFineTime 15
      BW 35
      FBH 1.0
      bg
```

```
            0 23

#
# BACKGROUND RADIATION
#
background
      photon
            usoil 36
            uconc 46
            thsoil 44
            thconc 21
            ksoil 85
            kconc 23.7
      neutron
            lat 0
            long 0
            smod 0.5
            elev 0

#
# DETECTORS
#
detection
      he3
            posx 198.1
            posy 0
            posz 100
            height 182.88
            modrad 3.8
            refrad 0.0
            actwidth 52
            eff 1.0
            fanofac 1.0
            alarm
                  gc
                        nint 1
```

Active Background vs. Beam Energy and Cargo Type (VoidMid - 8 MeV)

```
#
#    XPASS Threat Scenario Modeling Software
#

#
# PHYSICS
#
physics
      photon on
      neutron on
      fissgamma off
      mactime on
      ergfac 1
```

```
      refeps 1e-4
      sigmaeff 0.0
      interval 0.1
      background off

#
# SOURCE
#
source
      snm 0
            type heu
            mass 5000
            iso
                  u234 0.70
                  u235 90.3
                  u236 0.3
                  u238 8.7
            posx 48.1
            posy 750
            posz 100

#
# VEHICLE
#
vehicle
      truck
            cargo
                  midz 1
                  void 1
            stream 0.0
            velocity 8.05

#
# ACTIVE INTERROGATION
#
AI
      electrons
            12.0 1
      current 38
      sx -700
      sy 0
      sz 100
      target W
      thickness 1.5
      erad 1
      pulsew 6
      freq 50
      nFineTime 1
      BW 45
      FBH 1.0
      bgXw 65
      bgYw 15
      bgZw 65
```

```
#
# BACKGROUND RADIATION
#
background
      photon
            usoil 36
            uconc 46
            thsoil 44
            thconc 21
            ksoil 85
            kconc 23.7
      neutron
            lat 0
            long 0
            smod 0.5
            elev 0

#
# DETECTORS
#
detection
      he3
            posx 198.1
            posy 0
            posz 100
            height 173
            modrad 3.8
            refrad 0.0
            actwidth 52
            eff 1.0
            fanofac 1.0
            alarm
                  gc
                        nint 1
```

Detector Signal vs. Shielding Configuration (2.0 cm Pb)

```
#
#    XPASS Threat Scenario Modeling Software
#

#
# PHYSICS
#
physics
      photon on
      neutron on
      fissgamma off
      mactime on
      ergfac 1
      refeps 1e-4
```

```
      sigmaeff 0.0
      interval 0.1
      background off

#
# SOURCE
#
source
      snm 0
            type heu
            mass 5500
            iso
                  u234 0.70
                  u235 90.3
                  u236 0.3
                  u238 8.7
            posx 48.1
            posy 750
            posz 100
            shield
                  layer
                        type lead
                        thick 2.0
                        stream 0

#
# VEHICLE
#
vehicle
      truck
            cargo
                  void 1
            stream 0.0
            velocity 8.05

#
# ACTIVE INTERROGATION
#
AI
      electrons
            10.0 1
      current 38
      sx 748.1
      sy 0
      sz 100
      target W
      thickness 1.5
      erad 1
      pulsew 6
      freq 50
      nFineTime 5
      BW 35
      FBH 1.0
```

```
#
# BACKGROUND RADIATION
#
background
      photon
            usoil 36
            uconc 46
            thsoil 44
            thconc 21
            ksoil 85
            kconc 23.7
      neutron
            lat 0
            long 0
            smod 0.5
            elev 0

#
# DETECTORS
#
detection
      he3
            posx 198.1
            posy 0
            posz 100
            height 173
            modrad 3.8
            refrad 0.0
            actwidth 52
            eff 1.0
            fanofac 1.0
```

Detector Signal vs. Shielding Configuration
(4.0 cm BPE + 2.0 cm Pb & Induced Background)

```
#
#    XPASS Threat Scenario Modeling Software
#

#
# PHYSICS
#
physics
      photon on
      neutron on
      fissgamma off
      mactime on
      ergfac 1
      refeps 1e-4
      sigmaeff 0.0
      interval 0.1
```

```
      background off

#
# SOURCE
#
source
      snm 0
            type heu
            mass 5500
            iso
                  u234 0.70
                  u235 90.3
                  u236 0.3
                  u238 8.7
            posx 48.1
            posy 750
            posz 100
            shield
                  layer
                        type bopoly
                        thick 4.0
                        stream 0
                  layer
                        type lead
                        thick 2.0
                        stream 0

#
# VEHICLE
#
vehicle
      truck
            cargo
                  lowz 1
            stream 0.0
            velocity 8.05

#
# ACTIVE INTERROGATION
#
AI
      electrons
            10.0 1
      current 38
      sx 748.1
      sy 0
      sz 100
      target W
      thickness 1.5
      erad 1
      pulsew 6
      freq 50
      nFineTime 5
```

```
      BW 35
      FBH 1.0
      bgXw 40
      bgYw 15
      bgZw 40

#
# BACKGROUND RADIATION
#
background
      photon
            usoil 36
            uconc 46
            thsoil 44
            thconc 21
            ksoil 85
            kconc 23.7
      neutron
            lat 0
            long 0
            smod 0.5
            elev 0

#
# DETECTORS
#
detection
      he3
            posx 198.1
            posy 0
            posz 100
            height 173
            modrad 3.8
            refrad 0.0
            actwidth 52
            eff 1.0
            fanofac 1.0
            alarm
                  gc
                        nint 1
```

Glossary

ACL - Average chord length

AI - Active interrogation

BPE - Borated Polyethylene

DP - Detection probability

EW - Energy windowing

FAP - False alarm probability

GC - Gross count

HEU - Highly enriched uranium

INL - Idaho National Laboratory

NORM - Naturally occurring radioactive material

LAD - Large area detector

LANL - Los Alamos National Laboratory

LLNL - Lawrence Livermore National Laboratory

MCNPX - Monte Carlo N-Particle eXtended

MC&A - Material controls and accounting

NNSA - National Nuclear Security Administration

PPS - Physical protection system

ROC - Receiver operating characteristic

SLD - Second Line of Defense

SNM - Special nuclear material

WGPu - Weapons grade plutonium

XPASS - eXpedited Analysis of Smuggling Scenarios

References

1. Embassy of the United States. “Remarks of President Barack Obama”, August 2012. http://prague.usembassy.gov/obama.html

2. 2012 Seoul Nuclear Security Summit. “2010 Washington Nuclear Security Summit”, August 2012. http://www.thenuclearsecuritysummit.org/eng_about/archive.jsp

3. National Nuclear Security Administration. “Material Control & Accountability”, August 2012. http://www.nnsa.energy.gov/aboutus/ourprograms/nuclearsecurity/materialcontrolandaccountability

4. National Nuclear Security Administration. “Fact Sheet: NNSA's Second Line of Defense Program”. August 2012. http://nnsa.energy.gov/mediaroom/factsheets/nnsassecondlineofdefenseprogram

5. G.G. Thoreson. “A General Nuclear Smuggling Threat Scenario Analysis Platform”. *The University of Texas at Austin,* August 2011

6. G.G Thoreson et al. “Efficient calculation of detection probabilities”. *Nuclear Instruments and Methods in Physics Research A*, Vol. 615, April 2010, pp. 313-325

7. K. Nelson et al. “A Statistical Model for Generating a Population of Unclassified Objects and Radiation Signatures Spanning Nuclear Threats”. *Los Alamos National Laboratory,* LLNL-TR-408407, Sept. 2008

8. G. Takoudis et al. “Spatial and spectral gamma-ray response of plastic scintillators used in portal radiation detectors; comparison of measurements and simulations”. *Nuclear Instruments and Methods in Physics Research A*, Vol. 599, Feb. 2009, pp. 74-81

9. R.T. Kouzes et al. “The role of spectroscopy versus detection for border security”. *Journal of Radioanalytical and Nuclear Chemistry*, Vol. 276, 2008, pp. 719–723

10. D.C. Stromswold. “Field Tests of a NaI(Tl)-Based Vehicle Portal Monitor at Border Crossings”. *IEEE Nuclear Science Symposium Conference Record*, Oct. 2004, pp. 196 - 200

11. R.M. Keyser et al. “Comparison of MCNP and experimental measurements for an HPGe-based spectroscopy portal monitor”. *Journal of Radioanalytical and Nuclear Chemistry*, Vol. 276, 2008, pp. 399-405

12. T. Burr et al. “Alarm criteria in radiation portal monitoring”. *Applied Radiation and Isotopes*, Vol. 65, May 2007, pp. 569-580

13. J. Ely et al. “The use of energy windowing to discriminate SNM from NORM in radiation portal monitors”. *Nuclear Instruments and Methods in Physics Research A*, Vol. 560, 2006, pp. 373–387

14. B.D. Geelhood et al. “Overview of Portal Monitoring at Border Crossings”. *IEEE Nuclear Science Symposium Conference Record*, Oct. 2003, pp. 513-517

15. R.C. Runkle et al. “Analysis of Spectroscopic Radiation Portal Monitor Data Using Principal Components Analysis”. *IEEE Transactions on Nuclear Science*, Vol. 53, June 2006, pp. 1418-1423

16. R. Dynes et al. “Evaluating Testing, Costs, and Benefits of Advanced Spectroscopic Portals for Screening Cargo at Ports of Entry: Interim Report”. *National Academies Press*, 2010

17. C.E. Moss et al. “Comparison of Active Interrogation Techniques”. *IEEE Transactions on Nuclear Science*, Vol. 53, Aug. 2006, pp. 2242-2246

18. R.C. Little et al. “Detection of Highly Enriched Uranium Through Active Interrogation”. *Los Alamos National Laboratory*

19. M. Hohlmann et al. “Design and Construction of a First Prototype Muon Tomography System with GEM Detectors for the Detection of Nuclear Contraband”. *IEEE Nuclear Science Symposium Conference Record*, 2009, pp.971-975

20. D.B. Pelowitz. “MCNPX User’s Manual Ver. 2.7.0”. *Los Alamos National Laboratory,* LA-CP-11-00438, April 2011

21. GEANT4 Collaboration. “Geant4 User's Guide for Application Developers Ver. 9.5.0”. Dec. 2011

22. E. Lewis et al. “Computational Methods of Neutron Transport”. *American Nuclear Society Press*, 1993

23. D.J. Mitchell et al. “GADRAS User Manual”. *Sandia National Laboratory*, November 2009

24. R. Alcouffe. “PARTISN Calculations of 3D Radiation Transport Bench-marks for Simple Geometries with Void Regions”. *Progress in Nuclear Energy*, vol. 39, 2001

25. T.M. Evans et al. “DENOVO: A NEW THREE-DIMENSIONALPARALLEL DISCRETE ORDINATES CODE IN SCALE”. *Nuclear Technology*, Vol. 171, Aug. 2010, pp. 171-200

26. E.I. Novikova et. al. “Designing SWORD - SoftWare for Optimization of Radiation Detectors”. *IEEE Nuclear Science Symposium Conference Record*, Vol.1, 2006, pp. 607-612

27. A.J. Fallgren et al. “An Introduction to TR-X: A Simplified Tool for Standardized Analysis”. *Los Alamos National Laboratory,* LA-UR-10-06128, 2010

28. B. A. Faddegon. "Forward-directed bremsstrahlung of 10- to 30- MeV electron incident on thick target of Al and Pb". *Med. Phys.* 15 (5) 1990

29. N. Starfelt and H. W. Koch. "Differential Cross-Section Measurements of Thin-Target Bremsstrahlung Produced by 2.7- to 9.7-MeV Electrons. *Phys. Rev.* 102 (6) 1956

30. D. P. Gierga. "Electron Photon Calculations using MCNP". *MIT Master's Thesis* 1998

31. C. E. Moss et. al. "Comparison of Active Interrogation Techniques". *IEEE TRANSACTIONS ON NUCLEAR SCIENCE.* Vol. 53 (4). 2006

32. C. E. Moss et. al. "Linear Accelerator-Based Active Interrogation For Detection of Highly Enriched Uranium". *Application of Accelerators in Research and Industry: 17th Int'l. Conference*

33. W.J.M. de Kruijf et al. “On the average chord length in reactor physics”. *Annals of Nuclear Energy*, Vol. 30, 2003, pp. 549–553

34. K.M. Case et al. “Introduction to the Theory of Neutron Diffusion”. *Los Alamos Scientific Laboratory*, LAMD-1273, 1953

35. D. Normal et al. "Pulsed Photonuclear-Induced, Neutron Measurements of Nuclear Materials with Composite Shielding". *52nd INMM Annual Meeting, Conference Proceedings*. 2011

36. J.L. Jones et al. "Enhanced Photofission-Based, Coincident/Multiplicity Inspection Measurements". *51st INMM Annual Meeting, Conference Proceedings*. 2010

37. W.M. Myers et al. "Photon and Neutron Active Interrogation of Highly Enriched Uranium". *INTERNATIONAL CONFERENCE ON NUCLEAR DATA FOR SCIENCE AND TECHNOLOGY*, 2004

38. C.E. Moss et al. " Neutron Detectors for Active Interrogation of Highly Enriched Uranium". *IEEE TRANSACTIONS ON NUCLEAR SCIENCE*. Vol. 51 (4). 2004